Department of Physics and Astronomy
University of Heidelberg

Test of CPT theorem invariance via mass difference of Ω-hyperons

Master Thesis in Physics
submitted by

Georgijs Skorodumovs

born in Ventspils, Latvia

2020

This Master Thesis has been carried out by Georgijs Skorodumovs
at the
Physikalisches Institut Heidelberg
under the supervision of
Priv.-Doz. Dr. Kai Schweda

Abstract

In this thesis we have reconstructed and studied the weak decays $\Omega^- \rightarrow \Lambda(p\pi^-)K^-$ and $\overline{\Omega}^+ \rightarrow \bar{\Lambda}(\bar{p}\pi^+)K^+$ of the Ω hyperons produced in Run 2 pp collisions at the centre-of-mass energy $\sqrt{s} = 13$ TeV. We have analysed the whole Run 2 pp data sample with selected $1.7 \cdot 10^9$ minimum bias events. We have observed that the hyperons gain an artificial positive offset to their mean invariant mass values when the corresponding daughter particles are handled as primary tracks by the standard Kalman tracking algorithm. The artificial mass offsets were estimated for the $\Lambda - \bar{\Lambda}$ and $\Omega^{\pm}$ baryons. Their measured values are $+292 \pm 7$ keV/c^2 and $+195 \pm 5$ keV/c^2, respectively. We have managed to lower the invariant mass shifts by a factor of two, i.e. 147 ± 10 keV/c^2 and 98 ± 7 keV/c^2 for the Λ and Ω hyperons, respectively. This was done by re-tracking the secondary tracks with a right hypothesis of their origin being the position of the secondary vertex. The invariant mass of 101452 Ω^- and 104469 $\overline{\Omega}^+$ baryons was determined in the momentum range $2 < p_T < 6$ GeV/c with an unprecedented precision $\mathrm{M}(\Omega^-) = 1672.5364^{+0}_{-0.0500} \pm (0.0061)_{\mathrm{stat}} \pm (0.0049)_{\mathrm{syst}}$ MeV/c^2 ($\chi^2_{\mathrm{red}} = 1.03$) and $\mathrm{M}(\overline{\Omega}^+) = 1672.5439^{+0}_{-0.0500} \pm (0.0060)_{\mathrm{stat}} \pm (0.0100)_{\mathrm{syst}}$ MeV/c^2 ($\chi^2_{\mathrm{red}} = 1.24$). This allowed us to perform the most precise test of CPT symmetry invariance in the Ω system of $\Delta\,\mathrm{M/M} = (-4.48^{+1.13}_{-0} \pm 8.41) \cdot 10^{-6}$ which is about a factor ten more precise than the current world average value. Our result is consistent with CPT symmetry conservation.

Zusammenfassung

In dieser Arbeit haben wir die schwachen Zerfälle $\Omega^- \rightarrow \Lambda(p\pi^-)K^-$ und $\overline{\Omega}^+ \rightarrow \bar{\Lambda}(\bar{p}\pi^+)K^+$ rekonstruiert und untersucht. Dafür haben wir den kompletten Datensatz, welcher während des LHC Run2 für Proton-Proton Kollision bei einer Schwerpunktsenergie von $\sqrt{s} = 13$ TeV gesammelt wurde, analysiert. Der Datensatz besteht aus $1.7 \cdot 10^9$ MB Events. Für den rekonstruierten Datensatz aus 101452 Ω^- und 104469 $\overline{\Omega}^+$ im Impulsbereich $2 < p_T < 6$ GeV/c haben wir beobachtet, dass der Kalman Algorithmus die Energien von Ω Töchterteilchen drastisch überschätzte, wenn diese als primäre Teilchen angenommen wurden. Dies resultierte in eine positive Massenverschiebung von $+292 \pm 7$ keV/c^2 bzw. $+195 \pm 5$ keV/c^2 für die rekonstruierten Massen von Λ bzw. Ω Teilchen. Wir haben geschafft, die Massenverschiebung zu minimieren, indem die Töchterteilchen mit einer richtigen Annahme der sekundären Teilchen "re-trackt" wurden. Die neuen Werte betragen 147 ± 10 keV/c^2 bzw. 98 ± 7 keV/c^2 für die Λ bzw. Ω Baryonen. Die invariante Masse von $\Omega^\pm$ Teilchen wurde mit der höchsten Präzision bestimmt. Unser Ergebnis lautet $\mathrm{M}(\Omega^-) = 1672.5364^{+0}_{-0.0500} \pm (0.0061)_{\mathrm{stat}} \pm (0.0049)_{\mathrm{syst}}$ MeV/c^2 ($\chi^2_{\mathrm{red}} = 1.03$) und $\mathrm{M}(\overline{\Omega}^+) = 1672.5439^{+0}_{-0.0500} \pm (0.0060)_{\mathrm{stat}} \pm (0.0100)_{\mathrm{syst}}$ MeV/c^2 ($\chi^2_{\mathrm{red}} = 1.24$). Dies ermöglichte, einen präzisen Test der CPT-Invarianz mit Ω Teilchen durchzuführen, $\Delta\,\mathrm{M/M} = (-4.48^{+1.13}_{-0} \pm 8.41) \cdot 10^{-6}$. Das Ergebnis ist in Übereinstimmung mit der CPT-Invarianz.

Contents

Abstract 3

1 Introduction 9

2 Discrete transformations & symmetry violation 12

2.1 Discrete symmetries 13

2.2 CPT - exact symmetry of nature? 16

3 ALICE Detector System 20

3.1 Inner Tracking System 21

3.2 Time Projection Chamber 23

4 Event and track selection 28

4.1 Data sets and event selection 28

4.2 Track selection 29

5 Cascade reconstruction 33

5.1 General cascade finding with ALICE 35

5.2 Reconstruction in Run II 36

5.3 Topological selection 36

6 Analysis 45

7 Systematics studies 58

7.1 Systematics in different periods 61

7.2 Variation of track and topology selection 63

7.3 Λ mass dependence 65
7.4 Magnetic field 68
7.5 TPC related systematic studies 70

8 Results and outlook **80**

Appendix A Discrete Symmetries **83**

Appendix B Event properties **85**

Appendix C On covariance and correlation factors **87**

Appendix D Λ mass dependence of the Ω mass spectrum **90**

References **92**

Acknowledgments **98**

Listing of figures

1.1 $\Omega^{\pm}$ signal measured by Chan et al. (1998) 10

2.1 Overview of CPT test results performed for known systems using the comparison of measured masses for particles and their counterparts. For visibility some of the displayed error-bars have been enlarged by factors given in brackets under the corresponding particle's name. The central values were not scaled. Data taken from (Tanabashi et al., 2018; Adam et al., 2015). . . 19

3.1 Overview of the ALICE detector system, Botta (2017) 21
3.2 Layout of the Inner Tracking System, figure from Aamodt et al. (2010) . . 22
3.3 Properties of ITS (Contin, 2012). 22
3.4 Sketch of the TPC field cage and principle of particle tracking 24
3.5 Average momentum resolution for the selected daughter tracks coming from cascade decay. The species types stand for corresponding particle hypothesis: p - positive daughter of V0, π - negative daughter of V0, K - bachelor track of the cascade. A similar definition is implemented for the anti-particles. 25
3.6 The measured specific energy loss dE/dx is depicted as a function of particle momentum for various particle types. The solid lines show the theoretically expected energy loss curves. The figure is taken from ALICE (2015). . . . 26

4.1 Distribution of spatial positions of the primary interaction vertex for selected events. 29

5.1 Schematic overview of PID capabilities of ALICE. 34
5.2 Schematic visualisation of the topology in the V0 and cascade decays. . . . 35

5.3 Visualisation of topological properties which were corrected manually in the Run 2 hyperon reconstruction. 37
5.4 Schematic sketch of the estimation of the distance of closest approach between a charged particle's track in a magnetic field and the primary vertex. . 38
5.5 Schematic decay of a particle into two daughter tracks (blue dotted lines) is sketched. The momentum of the mother particle is $\vec{p}$ and the distance $\vec{D}$ from the coordinate origin. The reconstructed position of the primary vertex on an event-by-event basis is given by the vector $\vec{D}_{PV}$. Note: the track does not have to originate from the primary vertex. 41
5.6 Cascade rejection. Invariant mass spectra of the Ξ/Ω particles 43

6.1 Invariant mass spectrum of the Ω hyperons depicted for a selected p_T-bin. . 47
6.2 Mean mass distribution of the Ω hyperons as a function of the transverse momentum p_T. The results are obtained for the initial Ω sample. 49
6.3 Mean mass distribution of the daughter Λ hyperons as a function of the transverse momentum p_T. The daughter particles are handled as primaries by the Kalman tracker. 50
6.4 Mean mass of the combined Λ and $\bar{\Lambda}$ spectrum as function of transverse momentum shown for different radial distances of the secondary Λ position. 51
6.5 Sketch of the energy correction procedure performed for the daughter tracks. 52
6.6 Studies of the energy loss correction dE in dependence on the particle momentum and pseudo-rapidity 53
6.7 The average energy loss $\langle dE \rangle$ as a two-dimensional function of the particle momentum and the position of the secondary vertex. 54
6.8 Energy corrected mean mass distribution of the daughter Λ hyperons. . . . 55
6.9 Width of the mass peak σ, described by the Gaussian distribution, as a function of the particle momentum. The case when no energy loss correction is done on the secondaries is compared to the case when the energy correction is applied on the secondary particles. The analysed Λ hyperons are daughters of the Ω baryons. Hence, they (Λ) decay at larger radii than the mother particle. This leads to a larger correction of the width of the mass distribution. 56
6.10 Energy loss corrected mean mass distribution of the $\Omega^{\pm}$ baryons as a function of the transverse momentum. 57

7.1 Plateau analysis for each data sample collected for each data taking period. . 62

7.2 Distribution of systematic uncertainty $\sigma_{\langle\Delta\mu\rangle}$ obtained in the mass analysis of the Ω hyperons obtained on different data sub-samples using the variation of topological cuts. 64
7.3 Invariant mean mass spectra of the Ω baryons as a function of p_T. Two different methods were used for the mass computation. The dark blue squares represent the Ω mass values which were calculated using the world average mass value of the Λ baryon. The light blue squares denote the reconstructed Ω mass. 65
7.4 Systematic studies of the Ω mass spectrum. 66
7.5 Mean mass spectrum of the $\overline{\Omega}^{+}$ particle as a function of the momentum p_T, plotted for two different magnetic field polarities. 69
7.6 Systematic studies of the Ω invariant mass dependence on the quality of the PID with the TPC. The red arrow indicate the central cut value used for the analysis. Every measurement is compared to the proper superset with $n_{\sigma(dE/dx} < 4$. 72
7.7 Systematic studies of the Ω invariant mass dependence on the threshold number of reconstructed track clusters inside the TPC N_{cls}. The red arrow indicate the cut value put on the allowed number of TPC clusters used in the analysis. Each measurement is compared to that with $N_{\text{cls}} > 70$. 73
7.8 Systematic studies of the Ω invariant mass dependence on the threshold ratio of the number of reconstructed track clusters to the number of findable clusters $N_{\text{cls}}/N_{\text{findable}}$. Red arrow indicate the minimum allowed value of $N_{\text{cls}}/N_{\text{findable}}$ which was used in the analysis. Each measurement is compared to that with $N_{\text{cls}}/N_{\text{findable}} > 70$. The green vertical line at $N_{\text{cls}}/N_{\text{findable}} = 90$ shows where the discrepance between real data and MC becomes significant. See text for more detail. 74
7.9 Invariant mass spectrum of the $\Omega^{\pm}$ hyperons for different cuts of the Ξ mass. 75
7.10 Distribution of the mean mass deviations (upper panels) and the computed systematic uncertainty as a function of the width of the Ξ-mass rejection window. 76
7.11 Distribution of the systematic uncertainty due to cascade rejection. 77

C.1 **(a)** General subsets with a non vanishing intersection U. **(b)** Independent subsets. This can the case when studying sets dependent on different B field polarities, different TPC counting gas etc.**(c)** Case of inclusion. This case is studied by Barlow (2002). 87

List of Tables

1.1 Properties of HyperCP and ALICE Ω measurements 11

2.1 Summary of CPT tests performed in the strange particle sector. The value marked with an asterisk stands for an estimate, Tanabashi et al. (2018). . . . 19

4.1 Track selection and analysis cuts 32

5.1 Some properties for cascades and V0 particles. The shown decay channel depicts daughter particles which are reconstructed in this analysis. 42

5.2 Topological selection used during the pre-selection routine and in the analysis. The flag *any* means that no cut was done on a topological variable. . . 44

7.1 Values of topological cuts used for the analysis (central) and for the topological variations. The latter are shown in the right two columns. Variables are varied within a given value range in equidistant steps. Each value is chosen randomly (flat distribution). The units of variables in each row are shown in the left column. 63

7.2 Data sub-samples split to account for the magnetic field. 68

7.3 Results obtained in the analysis of the energy rescaled Ω sample invariant mass dependence on the polarity of the magnetic field. 68

7.4 Data sub-samples split to account for the TPC counting gas composition. . 70

7.5 Results obtained in the analysis of the energy corrected Ω sample invariant mass dependence on the TPC gas composition. 70

7.6 Signal yields of the $\Omega^{\pm}$ baryons for different mass window with of the Ξ mass used for the cascade rejection. 75

7.7 Mean mass of the $\Omega^{\pm}$ candidates in dependence on the radial decay position of the daughter Λ baryon. 78
7.8 Mean mass of the $\Omega^{\pm}$ candidates in dependence of the radial decay position of the mother Ω baryon. 79

8.1 Summary of the statistical and systematic uncertainties of the $\Omega^{\pm}$ mass values. 81

A.1 Summary of action of discrete (inversion) symmetry operators: parity (P), charge conjugation (C), time-reversal (T) and its combination, CPT, on different observables. 84

B.1 Periods' and event information 86

1

Introduction

The central objective of this work is the study of the decay $\Omega \to \Lambda K \to (p\pi)K$. The Ω hyperon is a special particle in the particle zoo of the Standard Model. Its discovery by Barnes et al. (1964) from a single event at the Brookhaven National Laboratory completed the SU(3) classification scheme of hadrons introduced independently by Gell-Mann (1961), Ne'eman (1961) and Zweig (1964). According to the theoretical predictions, the Ω baryon is a ground state ($J^p = \frac{3}{2}^+$) of the baryon decuplet with strangeness $S = -3$, hypercharge $Y = -2$ and a mass of ~ 1.672 GeV/c^2. The discovery in turn justified the theory that not only are the strongly interacting particles composite of elementary quarks but also that the strange quark exists!

Since then the properties of the Ω baryon were extensively studied by various experiments. The biggest contribution to the estimation of parity (Lu et al., 2005) and CP violation (Lu et al., 2006) in Ω decays was done by the HyperCP (E871) Collaboration at Fermilab, whose initial goal was to study CP violation in hyperon decays. The HyperCP experiment collected the largest hyperon samples during the runs in the years 1997 and 1999: 2.5 billions of Ξ^- and $\bar{\Xi}^+$ events and $\sim$ 10 million of Ω^- and $\bar{\Omega}^+$ decays (White, 2001; Burnstein et al., 2005). For

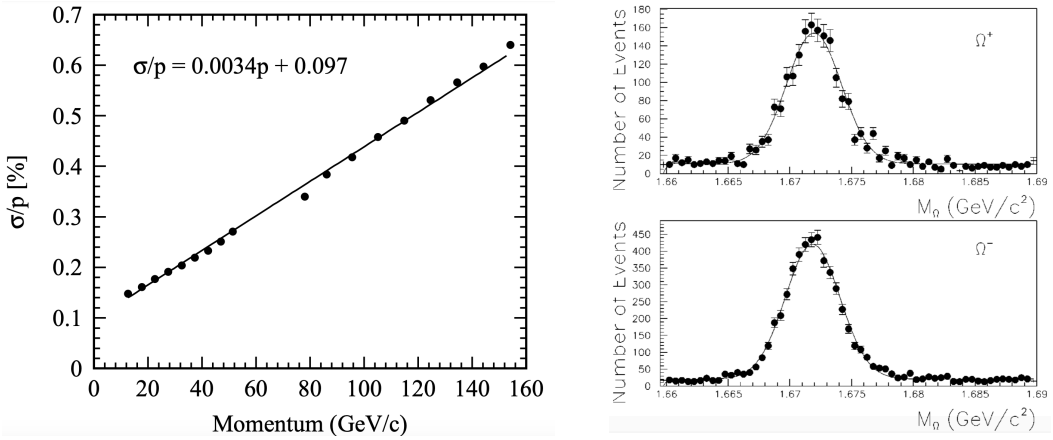

(a) Relative momentum resolution

(b) Ω invariant mass signal

Figure 1.1: $\Omega^{\pm}$ signal measured by Chan et al. (1998)

nearly 40 years the value of the Ω spin could not be determined experimentally because the production mechanisms of the hyperon have not been clearly understood. Only the recent study of exclusive decays $\Omega_c^0 \rightarrow \Omega^-\pi^+$ and $\Xi_c^0 \rightarrow \Omega^- K^+$ by Aubert et al. (2006) shows consistency with $S_\Omega = \frac{3}{2}$.

The ALICE and CMS Experiments at LHC, CERN, have analysed the yields of hyperons (among them Ω) with a goal to study the strangeness production mechanisms and collective motion (such as elliptic flow) in heavy ion collisions (Sirunyan et al., 2020; Acharya et al., 2020). The Ω baryon has been studied neither with LHCb nor with the ATLAS Experiments. Hence, no precision measurements of intrinsic $\Omega^{\pm}$ properties have ever been done with LHC.

In this work we want to perform a CPT test by precisely measuring the hyperon mass. So far the only CPT test via the measurement of $\Omega^- - \Omega^+$ mass difference was performed by Chan et al. (1998) with the result $\Delta M_\Omega / M_\Omega = (1.44 \pm 7.98) \times 10^{-5}$. This result was obtained in a fixed target experiment ($p + Be \rightarrow \Omega + X, E_p = 800$ GeV) at Fermilab (E756 Collaboration), whose initial aim was to measure the $\Omega^{\pm}$ magnetic moment and production polarization of hyperons. The $\Omega^-(\Omega^+)$ analysis sample consisted of 6323(2607) candidate events in a momentum range $250 - 450$ GeV. The production of $\bar{\Omega}^+$ was suppressed by a non-vanishing strange baryon-chemical potential $\mu_S \approx \frac{420}{\sqrt{s_{NN}}\ (GeV)}$ MeV. Indeed, with $\sqrt{s_{NN}} \approx 40\ GeV$ one can roughly estimate the suppression factor $\frac{\bar{\Omega}^+}{\Omega^-} = exp(-\frac{6\mu_S}{T}) \approx 0.6$ with $T \approx 160\ MeV$ (Aggarwal et al., 2011; Gao et al., 2018). Moreover, particle and anti-particle events were selected when applying opposite polarisations of magnetic field.

Although, ALICE and HyperCP have nearly the same resolutions in invariant mass reconstruction ($\sigma_\Omega = 2.3\, MeV/c^2$), ALICE enables a CPT test in a high energy regime with a vanishing baryo-chemical potential $\mu = 0$. This implies that spectra of produced particle and anti-particles have the same properties. Moreover, Ω^- and Ω^+ events are produced in the same collision. This provides an important systematic check, as the analysis is performed under same conditions. The momenta of the production yields are lower than at HyperCP which allows one to test CPT symmetry in a different part of the parameter space.

In this analysis we study central proton-proton collisions at $\sqrt{s} = 13$ TeV. Although, the strangeness yields are reduced in comparison to heavy-ion collisions (Hamieh et al., 2000), the lower final state multiplicity allows for a cleaner tracking environment and an enhanced signal-to-background ratio when compared to the p-Pb or Pb-Pb collisions.

Some properties of the HyperCP and ALICE experiments are summarised in table 1.1.

Variable	HyperCP E756	ALICE
Collision system	$p + Be$	$p + p$
Type of collisions	fixed target, $E_p = 800 GeV$	central $\sqrt{s} = 13 TeV$
Ω momentum range	$250 - 450$ GeV	$0.6 - 6.0$ GeV
Number of $\Omega^\pm$ events	$\sim 9 \cdot 10^3$	$\sim 5 \cdot 10^5$
Yield ratio $\bar{\Omega}^+/\Omega^-$	~ 0.4	~ 1.0
Magnetic field	2.1 T	0.5T (and 0.2T)
Resolution, σ_Ω	~ 2.3 MeV/c^2	~ 2.3 MeV/c^2

Table 1.1: Properties of HyperCP and ALICE Ω measurements

This thesis is structured as follows. Chapter 2 gives a brief theoretical overview of discrete symmetries: parity (P), charge conjugation (C) and time reversal (T). Consequently, the CPT symmetry, its possible observables and fundamental tests are discussed with pecial emphasis on the system $\Omega \rightarrow \Lambda(p\pi)K$ analysed with ALICE. Chapter 3 outlines the ALICE detector system with a highlight on the Inner Tracking System and Time Projection Chamber, which perform the tracking reconstruction and particle identification. Event and tracking reconstruction are described in chapter 4. Chapter 5 deals with the topological selection of Λ and Ω particles in detail. The central cut values on topological variables are summarised therein. The strategy and performance of the analysis is the central topic of chapter 6. Chapter 7 is dedicated to the description of related systematic uncertainties. A summary is given in chapter 8.

2

Discrete transformations & symmetry violation

It is hard to underestimate the role which symmetries play in physics and, especially, in particle physics. The study of symmetries has been the driving force in building up the Standard Model (SM). Besides the Lorentz covariance (energy-momentum conservation) and global gauge invariance of the electromagnetic field (charge conservation), a few examples are:

- The unification of electromagnetic and weak interactions incorporated in the Yang-Mills field with the underlying electroweak symmetry group $U_Y(1) \times SU_L(2)$ (Glashow, 1961; Salam & Ward, 1964). This predicted the existence of the Z boson and the strength of weak couplings. The spontaneous breaking of electroweak symmetry by the Higgs mechanism gives rise to the mass of bosons $W^{\pm}$, Z and photons.
- Spontaneous breaking of the QCD chiral symmetry justifies the existence of three low mass pions (Gell-Mann et al., 1968)

- global SU(3) symmetry of QCD introduces structure into the zoo of strongly interacting particles, grouping them into octets and decuplets, as well as predicting the existence of gluons (Gell-Mann, 1961; Berger et al., 1979).
- Spontaneous breaking of the vacuum gives rise to the Higgs mechanism (Higgs, 1964).

This chapter is dedicated to the three kinds of discrete symmetries: parity (P), charge conjugation (C), time reversal (T), as well as their combinations CP and CPT symmetries. Since a vast amount of literature is dedicated to C, P and T symmetries, the focus of this chapter is mainly on experimental aspects of discrete symmetries with emphasis on the weak decay $\Omega \to \Lambda(p\pi)K$. The Appendix A provides a brief theoretical overview.

The chapter is built up as following: section 2.1 concentrates on the P, C and T symmetries and highlights the current results obtained in P, C and CP symmetry violation tests in the Ω system. Section 2.2 is dedicated to the CPT symmetry, possible consequences of CPT breaking are discussed. Consequently, a few possible CPT observables and test possibilities are described. Particular emphasis is given to the strange particle sector. The current CPT tests for stange particles are briefly discussed.

2.1 Discrete symmetries

Discrete symmetries are very special among other kinds of symmetries and are represented by unitary transformations U, i.e. $U^\dagger U = UU^\dagger = 1$, which in turn can be linear or anti-linear due to Wigner's theorem (Wigner, 1959). Mathematically, the anti-linearity simply means that all scalar factors are complex-conjugated under the corresponding transformation. Parity and charge conjugation are described by linear operators, whereas the time-reversal - by the anti-linear operator. The property of (anti-)linearity is deeply connected to a transformation itself and cannot be chosen by hand (Sozzi, 2018).

The outlined transformations are also called *inversions*, as they return a given system back to itself when applied twice, i.e. $U^2 = 1$. For a quantum field φ_i this implies:

$$U^\dagger \varphi_i(x) U = \eta_U S_{ij} \varphi_j(x'), \tag{2.1}$$

where S_{ij} is a matrix which acts on the fields φ_i and depends solely on the structure of the fields. The factor η_U represents a bridge between theory and experiment: if a transformation U is a valid symmetry of a system described by a Hamiltonian H, then $[U, H] = 0$ and $|\eta_U|^2 = 1$; for eigenstates of U the latter property implies that only values $\eta_U = \pm 1$ are

allowed. This gives rise to selection rules of transitions between states, which subsequently can be tested in experiments. If a state is not an eigenstate then there is no general procedure. Importantly, there is no analogue of the Noether theorem for discrete symmetries. This implies that there can be no conserved quantities, even if a discrete symmetry holds in a given system. (Sozzi, 2018).

Since the pioneering work by Wu et al. (1957) various experiments have showed that C, P, T as well as CP symmetries are broken in weak interactions only. It is appealing to search for a possible violation of CPT symmetry in a weakly interacting system.

2.1.1 Parity symmetry

The action of the parity P operator is an inversion of spatial coordinates $\vec{x} \to -\vec{x}$. Any state is transformed as $P|\vec{p}, s, q\rangle = \eta_P |-\vec{p}, s, q\rangle$. For around 60 years it has been known that parity is maximally violated by the weak interactions (Wu et al., 1957; Garwin et al., 1957). The origin of violation is the V-A nature of the weak coupling. The weak decays $\Omega \to \Lambda K$ with consequent $\Lambda \to p\pi$ are no exceptions. The P violation in these systems is measured in terms of the asymmetry decay parameter α, which manifests itself as an anisotropy of the angular distribution of the daughter proton in rest frame of daughter the Λ hyperon (Chen et al., 2005; Lu et al., 2006; Ablikim et al., 2019)

$$\frac{d\Gamma}{d\Omega} \sim 1 + \alpha_\Omega \alpha_\Lambda \cos\Theta, \tag{2.2}$$

where $\alpha_\Omega \sim Re(P^* D)$ is a measure of the interference between P- and D-wave state amplitudes, i.e. $J^P = 1^-$ and $J^P = 2^+$, respectively. Analogously, one defines $\alpha_\Lambda \sim Re(S^* P)$ with the S-wave state $J^P = 0^+$. The combined result $\alpha_\Omega = (1.80 \pm 0.24) \cdot 10^{-2}$ by Chen et al. (2005) and Lu et al. (2006) confirms that parity is indeed violated in the Ω golden decay channel.

2.1.2 Charge conjugation and CP symmetry

In quantum theory the charge conjugation operator C is defined by its action on the charge operator Q, $Q \to Q_C = C^\dagger Q C = -Q$. The operator Q describes not only electric charge, but also any internal charge (i.e. baryon number). The action of C on a state with momentum $\vec{p}$, spin s and charge q is given by $C|\vec{p}, s, q\rangle = \eta_C |\vec{p}, s, -q\rangle$.

The charge conjugation symmetry has been tested to be conserved in electromagnetic (Mills

& Berko, 1967) and strong interactions (Pais, 1959; Dobrzynski et al., 1966) where it manifests itself in various selection rules (Furry, 1937; Pais & Jost, 1952). On the contrary, this symmetry is maximally violated in the weak interactions in a similar way to P symmetry. As a consequence, one would not expect particles and anti-particles to have the same properties solely on the grounds of C symmetry.

Practically, an experimental study of C violation implies a measurement of the phase η_C, which can take values ± 1 only in case of C eigenstates, e.g. photons. None of the involved particles in this analysis is a C eigenstate. For these particles the number η_C is unphysical, its value is free of choice and consequently it cannot be measured. In principle, the C symmetry can be tested indirectly. However, we would need to prepare particle and anti-particle systems in a way that all their initial quantum numbers are known in detail. This would be very challenging for ALICE.

Instead of measuring C symmetry separately, one usually studies the combined CP symmetry. For hyperon decays, a standard procedure is to compare the decay parameters of a particle α and its counterpart $\bar{\alpha}$. If CP is a valid symmetry, the partial decay widths of $\Omega^- \to \Lambda(p\pi^-)K^-$ and $\Omega^+ \to \bar{\Lambda}(\bar{p}\pi^+)K^+$ must be equal and the relation must hold $\alpha = -\bar{\alpha}$ (Pais, 1959). With unprecedented precision, CP symmetry is measured in the $\Omega^\pm$ system by Chen et al. (2005) and Lu et al. (2006)

$$\frac{\alpha_{\Omega^-} + \bar{\alpha}_{\Omega^+}}{\alpha_{\Omega^-} - \bar{\alpha}_{\Omega^+}} = -0.016 \pm 0.092(\text{stat}) \pm 0.089(\text{syst}) \tag{2.3}$$

which indirectly proves that C symmetry is violated in Ω decays.

The action of the CPT operator may be decomposed as an action of CP with a subsequent action of the time-reversal operator T. Since CP symmetry is experimentally shown to hold for Ω decay, one could try to prove T-violation (or conservation), which in turn would mean violation (or conservation) of the combined CPT symmetry.

2.1.3 Time reversal

Operation of time reversal on a given system formally means the inversion of time $t \to -t$. For microscopic systems described by laws of quantum mechanics, one introduces the Wigner time reversal operator T. In comparison to P and C operators the time reversal T is anti-unitary, i.e. unitary and anti-linear. Mathematically, anti-unitarity means a combination of time inversion and charge conjugation $i \to -i$, i.e. $it \to it$, which preserves non-negativity of energy eigenvalues. Experimentally, the anti-unitarity of the T operator is a complication.

It can be shown that the scattering matrix S transforms as $S \rightarrow S_T = T^{\dagger}ST = S^{-1}$ (Sozzi, 2018). Generally, $S^{-1} \neq S$ and hence $[S, T] \neq 0$. The latter implies that even if time reversal symmetry is valid, there are no conserved quantum numbers related to it. Moreover, it has been theoretically proven that there are no vanishing observables if T symmetry holds, i.e. no null experiment can be done (Arash et al., 1985).

If one tries to test T symmetry separately, one usually has two options at hand.

The first possibility would be to study the **electric dipole moment** (EDM) of the Ω baryon which violates both P and T (Khriplovich & Lamoreaux, 1997). This would not be an option for ALICE, since EDM searches demand the detailed and controlled knowledge of the polarisation state of the studied system (Crivellin et al., 2018; Abel et al., 2020).

Another option would be a measurement of **T-odd variables**. If T symmetry is valid, then the Hamiltonian which describes the system cannot depend upon any of the terms: $S_1 \cdot (S_2 \times S_3)$, $p \cdot (S_1 \times S_2)$, $p_1 \cdot (p_2 \cdot p_3)$ etc. Here S_i and p_i denote spins and momenta of mother and daughter particles. Although it is possible to infer the longitudinal polarisation of daughter Λ hyperons, we have no knowledge about the spin orientation of Ω baryons. One could try to construct the T-odd variable exclusively out of momenta of involved particles. However, it would also result in an experimental complication since the presence of the final state interactions between daughter hadrons (Λ and $K^{\pm}$ or p and $\pi^{\pm}$) would affect the observable T quantity (Sozzi, 2018). One usually studies three-body or rare four-body decays of weakly interacting particles such as $K^+ \rightarrow \pi^0\mu^+\nu_\mu$ (Hasinoff et al., 2006), $\mu \rightarrow e\nu\bar{\nu}$ (Burkard et al., 1985) or $K^- \rightarrow \pi^0 e^- \bar{\nu}_e \gamma$ (Bolotov et al., 2005).

To conclude, any measurement of T symmetry in Ω system is extremely challenging at the current state. Therefore, one is left with the only option - to focus on a CPT symmetry as a whole and study the observables related to it.

2.2 CPT - EXACT SYMMETRY OF NATURE?

A subsequent action of the three symmetry operators C, P and T (in any order) results in a CPT transformation. This transformation links charge conjugation, spin statistics and Lorentz covariance (Lueders, 1954). The corresponding CPT theorem states that CPT is the exact symmetry of nature and puts the following constraints on any quantum field theory (QFT) Sozzi (2018):

- the Langrangian $\mathcal{L}$ of the QFT is Hermitian, local and normal-ordered;
- $\mathcal{L}$ preserves Lorentz symmetry;

- $\mathcal{L}$ respects the commutation (bosonic fields) and anti-commutation (fermionic fields) relations.

Generally, it is hard to construct a theory in which CPT symmetry is not conserved automatically (Sozzi, 2018). However, if CPT is found to be violated in any physical system, completely new horizons will be opened in physics beyond the Standard model. One of the main consequences of CPT symmetry violation is shown by Greenberg (2002): if CPT violation is present in an interacting field theory, then this theory is necessarily not Lorentz invariant.

There are various ways how one could attempt to include CPT violation in SM. For example, one could try to relax any of the assumptions listed above (Lehnert, 2016). Hawking (1976) points out that a possible breakdown of CPT symmetry may happen if gravitational effects modify laws of quantum mechanics. Current theoretical work concentrates on mechanisms addressing spontaneous CPT symmetry breaking, e.g. is possible for open bosonic strings in string theory (Kostelecky, 1998).

2.2.1 Tests of CPT symmetry

CPT symmetry may be tested experimentally. There are various consequences of the CPT theorem. For instance,

1. even if C symmetry is broken, particles and and their anti-particles must exist;

2. particles and anti-particles have electromagnetic properties equal in magnitude but opposite in sign (Sozzi, 2018). For practical purposes this motivates the precision tests of fine- and hyperfine structures, Lamb shifts (both in composite systems), as well as internal charges and magnetic moments;

3. the masses of stable particles and anti-particles are equal (Lueders & Zumino, 1957). Stable particles $|\psi\rangle$ and anti-particles $|\bar{\psi}\rangle$ are eigenstates of Hamiltonian H. For states at rest one can write $H|\psi\rangle = m(\psi)|\psi\rangle$ and $H|\bar{\psi}\rangle = m(\bar{\psi})|\bar{\psi}\rangle$. The action of CPT operator on a state is $CPT|\psi\rangle = \eta_{CPT}|\bar{\psi}\rangle$ with $|\eta_{CPT}|^2 = 1$. If CPT is a symmetry, then its operator commutes with the Hamiltonian and one obtains:

$$0 = [CPT, H]|\psi\rangle = \eta_{CPT}(m(\psi) - m(\bar{\psi}))|\bar{\psi}\rangle\,, \tag{2.4}$$

which justifies the above statement.

4. Expectation values of masses and life-times are equal for particles and their charge counterparts in case those are not stable. The non-relativistic Hamiltonian of decaying particles (at rest) is generally given by $H = M - \frac{i}{2}\Gamma$, where the real matrices M and Γ incorporate information about the mass and life-time, respectively. The expectation value of the Hamiltonian for a particle at rest would be $\langle\psi| H |\psi\rangle = \lambda$ with $\lambda \in \mathbb{C}$. One therefore investigates expectation values of pole positions $\langle\psi| (H-\lambda)^{-1} |\psi\rangle$. Lueders & Zumino (1957) show that $\langle\psi| (H-\lambda)^{-1} |\psi\rangle = \langle\bar{\psi}| (H-\lambda)^{-1} |\bar{\psi}\rangle$, where $|\bar{\psi}\rangle = CPT|\psi\rangle$. The core of derivation is the anti-linearity of CPT transformation (due to the T operator), $\lambda \xrightarrow{CPT} \lambda^*$.

This thesis is dedicated to test the CPT theorem on a hadronic system that decays via weak interaction. For hadrons the number of physical CPT observables is generally limited. This is mainly due to a lack of control over QCD effects. CPT observables can be introduced at the quark level as contributions to transition matrix elements (Sozzi, 2018). This can be viewed as a modification of values of Standard Model parameters. The problem arises when these modifications need to be transferred to the energy scale of the observed particles. On this scale QCD effects should be coped with in a non-perturbative regime. This can be done via lattice calculations. The systematic uncertainties are still too high to detect tiny CPT violation effects. This is the reason why this work deals only with the mass measurement of the $\Omega^{\pm}$ particle.

2.2.2 CPT IN STRANGE SECTOR

The idea of measuring and comparing masses and/or life-times of a particle and its counterpart is very simple. Harder is its realisation. How good has it been achieved in the strange sector so far, i.e. for hadrons with at least one strange valence quark and/or lighter quarks? Among 87 documented strange hadrons (including strange resonances), existence of only 49 is rather likely or certain (Tanabashi et al., 2018). The CPT test could be performed to $\sim 8\%$ of the latter - in exact numbers - only to 4 particles. The results are summarised in table 2.1. The CPT test based on the mass measurement has been done only for 13 particles, see fig.2.1.

Generally, CPT symmetry is tested very precisely for systems composite of stable particles and employs spectroscopic measurements of electromagnetic transitions. For instance, the CPT test on electrons was done via positronium spectroscopy. Differences between energy levels of ortho-positronium (2^3S_1) and para-positronium (1^3S_1) were compared with QED predictions (Fee et al., 1993). The most stringent matter-antimatter symmetry test on pro-

System	$\Delta m/m$	$\Delta\tau/\tau$
K^0	$< 6 \times 10^{-19}$	–
Λ	$(-0.1 \pm 1.1) \times 10^{-5}$	(-0.001 ± 0.009)
Ξ	$(-2.5 \pm 8.7) \times 10^{-5}$	(-0.01 ± 0.07)
Ω	$(-1.44 \pm 7.98) \times 10^{-5}$	$(0.00 \pm 0.05)^*$

Table 2.1: Summary of CPT tests performed in the strange particle sector. The value marked with an asterisk stands for an estimate, Tanabashi et al. (2018).

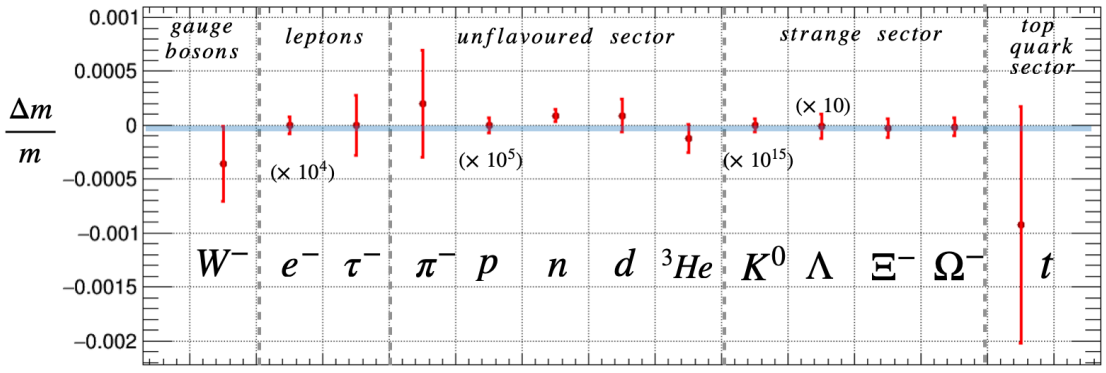

Figure 2.1: Overview of CPT test results performed for known systems using the comparison of measured masses for particles and their counterparts. For visibility some of the displayed error-bars have been enlarged by factors given in brackets under the corresponding particle's name. The central values were not scaled. Data taken from (Tanabashi et al., 2018; Adam et al., 2015).

tons was achieved by measuring the anti-proton to electron mass ration $M_{\bar{p}}/m_e$ in low energy single photon transitions of antiprotonic helium $\bar{p}He^+ \equiv \bar{p} + He^{+2} + e^-$ (Hori, 2018). Although strange particles are not stable, the K^0 system is exceptional. The study of the strangeness oscillations $K^0 - \bar{K^0}$ yield the most accurate result ever measured in any physical system (D'Ambrosio & Isidori, 2006), see table 2.1. For the Ω system the measured $\Delta M/M$ is 14 orders of magnitude less precise than in kaon system. In this work we will try to push this limit.

3

ALICE Detector System

ALICE, **A** **L**arge **I**on **C**ollider **E**xperiment, is a unique detector at CERN LHC whose aim is to study ultra-relativistic heavy ion collisions (Kuijer, 2003). ALICE is the only experiment at CERN which is utterly dedicated to deepen our understanding of strongly interacting matter in extreme conditions of high temperature and/or pressure. Meanwhile, the other 3 LHC experiments also have an active heavy ion (HI) program. The experiment covers a large physics program (Dainese, 2008). One of the avenues of research is a study of strange particles, e.g. investigation of intrinsic and collective properties, as well as strangeness production mechanisms (Kraus, 2009; Vasileiou, 2020). Exploration of strangeness is attractive in itself because there is no net strangeness in colliding particles, and is directly connected to the topic of this thesis.

Besides the analysis of nucleus-nucleus (Pb-Pb) collisions the physics program at ALICE also includes the study of head-on proton-nucleus (p-Pb) and proton-proton (p-p) collisions. The latter is mostly treated as a reference system in heavy ion physics (Monteno, 2005). The design centre-of-mass energy of the pp system is $\sqrt{s} = 14$ TeV with the instantaneous luminosity $\mathcal{L} = 10^{30}\ \mathrm{cm}^{-2}\mathrm{s}^{-1}$. In this work we focus on the study of pp collisions at highest

achieved energy of $\sqrt{s} = 13$ TeV.

The experimental apparatus has been built as a general-purpose detector that is able to cope with the high multiplicity environment of the produced particles, i.e. up to 8000 particles per pseudo-rapidity unit. Detectors are surrounded by the L3-Magnet (B=0.2 T or B=0.5 T). The choice of sub-detectors is motivated to address various physics questions. The detector overview is depicted in Fig. 3.1

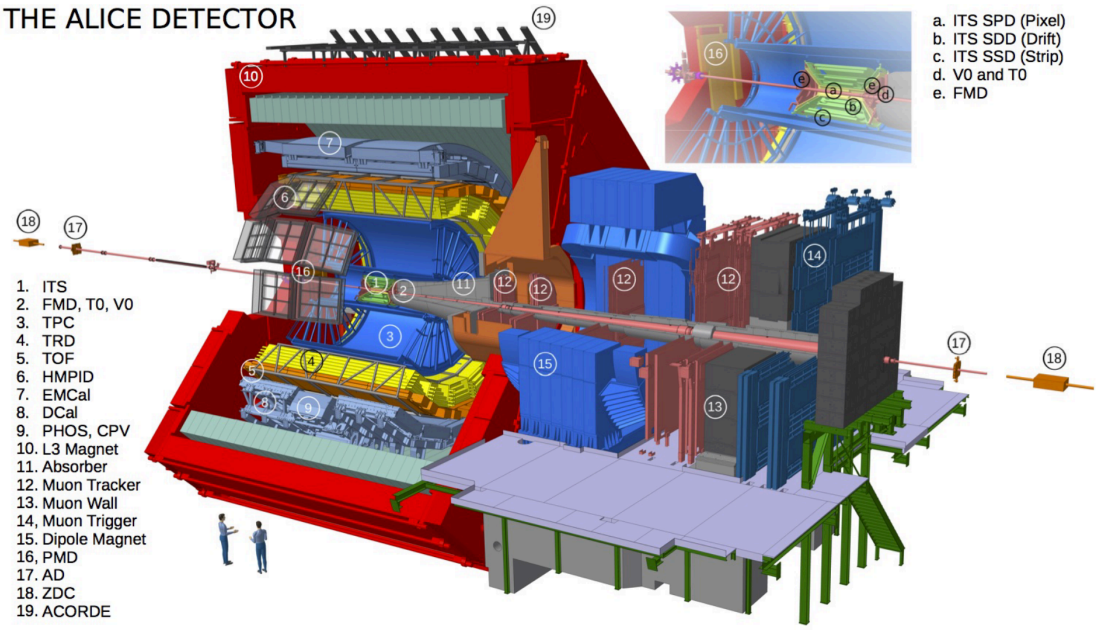

Figure 3.1: Overview of the ALICE detector system, Botta (2017)

The following sections outline the main ALICE detectors which play a crucial role in this analysis: the Inner Tracking System and the Time Projection Chamber.

3.1 Inner Tracking System

The innermost detector of the central barrel which is the reached by particles produced in beam collisions is the **I**nner **T**racking **S**ystem (ITS). The detailed design description is given in Dellacasa et al. (1999). For thorough information about the ITS performance refer to Contin (2012). In this section the main tasks of ITS are briefly outlined.

The detector consists of cylindrical coaxial semiconductor detectors which form six thin layers of a total material budget of $X/X_0 \approx 6\%$, see Fig. 3.2. ITS employs unique technology

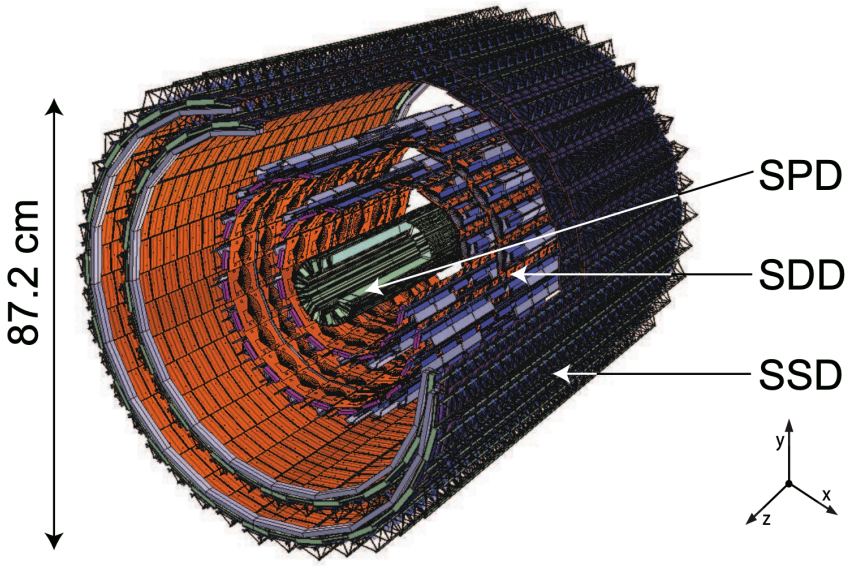

Figure 3.2: Layout of the Inner Tracking System, figure from Aamodt et al. (2010)

Layer / Type	r [cm]	$\pm z$ [cm]	Number of modules	Active area per module $r\phi \times z$ [mm^2]	Intrinsic resolution [μm] $r\phi$	z	Material budget X/X_0 [%]
1 / SPD	3.9	14.1	80	12.8×70.7	12	100	1.14
2 / SPD	7.6	14.1	160	12.8×70.7	12	100	1.14
3 / SDD	15.0	22.2	84	70.2×75.3	35	25	1.13
4 / SDD	23.9	29.7	176	70.2×75.3	35	25	1.26
5 / SSD	38.0	43.1	748	73×40	20	830	0.83
6 / SSD	43.0	48.9	950	73×40	20	830	0.83

Figure 3.3: Properties of ITS (Contin, 2012).

of silicon chip detectors and is built up out of two **S**ilicon **P**ixel **D**etectors (SPD), two **S**ilicon **D**rift **D**etectors (SDD) and **S**ilicon **S**trip **D**etectors (SSD).

The two innermost SPD layers have the highest granularity (i.e. active area per module $r\varphi \times z$) and the highest $r\varphi$ resolution among other ITS layers. The properties are motivated by the high particle density environment close to the primary vertex, table 3.3 . High tracking capability of SPDs is used to estimate both the position of primary interaction vertex and reconstruct vertices of pile-up events.

The drift detectors (SDD) and strip detectors (SSD) enable tracking with a resolution of order $r\varphi \sim 70\ \mu$m. Furthermore, the four layers (SDD and SSD) are equiped with analogue readout that enables identification of low energy particles ($p \leq 100$ MeV/c^2) via specific energy loss.

The utmost important task of ITS for the current work is the ability to reconstruct spatial positions of secondary vertices of hyperon decays. Moreover, ITS improves the momentum resolution of high energy tracks initially reconstructed by the Time Projection Chamber.

3.2 Time Projection Chamber

The core of the ALICE system is the **T**ime **P**rojection **C**hamber (TPC) which is the main tracking detector (Massimo, 2007). The TPC plays a crucial role in our analysis. In this section main properties of the TPC are presented. More information about the detector can be found in Alme (2010) and references therein.

The TPC is a 5 m long hollow cylindrical barrel detector with an inner radius of about 0.8 m and an outer radius - of $\sim$ 2.5 m. It provides momentum measurement of charged particles in the range $0.2 - 50$ GeV/c and particle identification via the specific energy loss dE/dx in a full azimuth and a pseudo-rapidity range $|\eta| < 0.9$ (Garabatos, 2004).

The TPC is filled with 88 m^3 counting gas. In order to provide stable operation, to minimize diffusion effect of drifting electrons and to maximize ion mobility, the quenching gas composition was chosen to be Ne-CO_2-N_2 in relative proportions 90 : 10 : 5 (in the year 2017) and Ar(88%) - CO_2(12%) (in the years 2016 and 2018).

The TPC forms a field cage, its body is divided into two parts of equal volume by the central electrode at the position z = 0, where a drift voltage of -100 kV is generated. This results in a drift field with a value of 400 V/cm along the beam direction, see fig. 3.4a.

When a charged particle enters the active volume of the detector, it loses energy via electromagnetic interactions with bounded electrons of gas atoms. During this process the electrons are freed, and atoms are ionised. These primary electrons drift along the z-direction with a constant velocity towards the TPC readout chambers. The latter are multi-wire proportional chambers (MWPC) and incorporate cathode pad readout technology, fig. 3.4b.

The moving electrons and positive ions in the gas induce mirror charges on the electrodes of the pad planes, resulting in positive voltage signals. Amplitudes of such signals would be of order 50 e^-, and it would be impossible to distinguish the signal from the noise (700 e^- – 1000 e^-). That is why the anode wires are used, in whose vicinity the primary electrons build up avalanches leading to the amplification (of factor $\sim 5000 - 6000$) of the readout signal.

Usual drifting velocities for primary electrons are of order 3 cm/μs. This results in a fast rising time of the induced signal. The ions drift 1000 times slower than the electrons. This

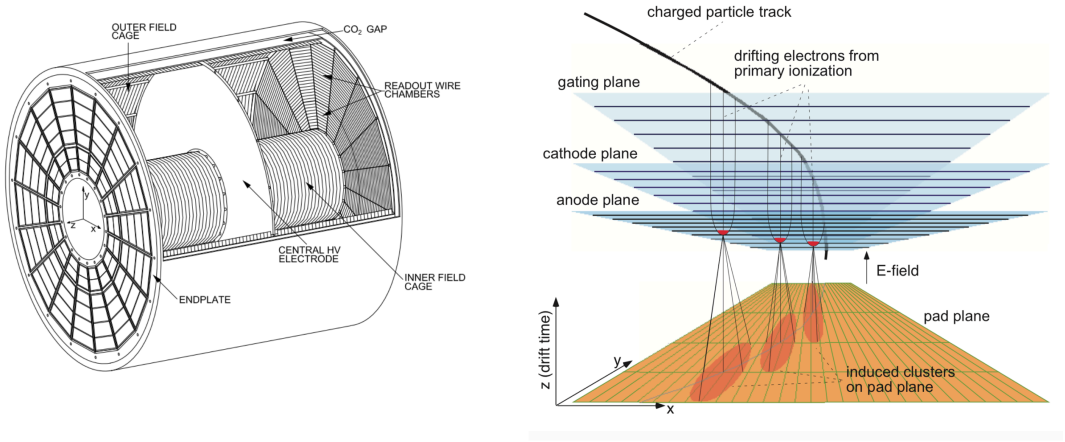

(a) Schematic view of the TPC field cage. The central electrode at -100 kV subdivides the cage into two rooms of equal volume with maximum drift length of 2.5 m. Endplates are MWPC and enable tracking of charged particles

(b) Schematic representation of the tracking inside TPC. The primary ionisation electrons are avalanched at the anode wires and are accumulated at the pad plane.

Figure 3.4: Sketch of the TPC field cage and principle of particle tracking

is the reason for the additional long tail of the order 100 μs in the readout signal. For the readout signal, the method of truncated mean is used which cuts the ion long tail.

3.2.1 Position and momentum measurements

A track of a charged particle traversing the TPC volume in a vicinity of magnetic field is described by a helix. Spatial points of this helix are found in the following way. The z-coordinate is obtained by a measurement of the drifting time of ionisation electrons reaching the readout chamber with a constant drift velocity v_{drift}. The coordinate in the x-y-plane is obtained as a centre-of-gravity of the corresponding charge cluster on the readout pads. The spatial point resolution depends on various parameters (including gas composition, temperature, geometry of readout and other parameters). An average position resolution achieved by TPC is of order of $1 - 2$ mm. The position resolution deteriorates with increasing drift length inside the TPC L_{drift} (due to diffusion of electron cloud) and increasing inclination angle λ (Lippmann, 2012).

The momentum resolution is usually given through the ratio of uncertainty and absolute value of transverse momentum σ_{p_T}/p_T and is not a constant parameter. The resolution σ_{p_T}/p_T is defined by the Gluckstern formula and is linearly proportional to p_T, pad resolution σ_{pad}

and inversely proportional to magnetic field B and number of found TPC clusters, $\sim N^{-0.5}$ (Gluckstern, 1963).

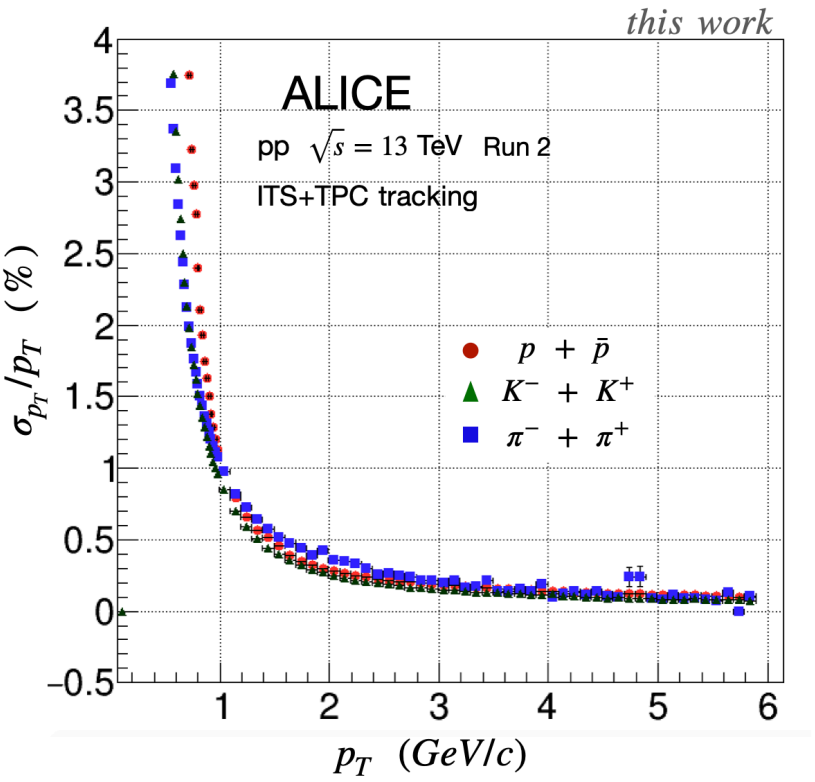

Figure 3.5: Average momentum resolution for the selected daughter tracks coming from cascade decay. The species types stand for corresponding particle hypothesis: p - positive daughter of V0, π - negative daughter of V0, K - bachelor track of the cascade. A similar definition is implemented for the anti-particles.

Fig. 3.5 shows the average momentum resolution for combined (ITS+TPC) tracking in Run2 measured for pre-selected daughter candidates of Ω/Ξ decays in pp collisions. The uncertainties are statistical only. Although tracking inside ITS improves the overall resolution, the main p_T-dependence is still dictated by capabilities of by TPC. It is important to point out that the resolution deteriorates for low-energy tracks due to multiple scattering, e.g. $\frac{\sigma_{p_T}}{p_T}(p_T = 0.2 GeV/c) \approx 4 - 6\%$. In a high energy regime, $p_T > 2\ GeV/c$, the resolution is the best with values in a range $\sim 0.1 - 0.2\%$

3.2.2 Particle identification with TPC

Electrically charged particles are identified inside the TPC by the characteristic ionisation energy loss per unit length dE/dx which is described by the Bethe-Boch formula (Bethe &

Ashkin, 1953):

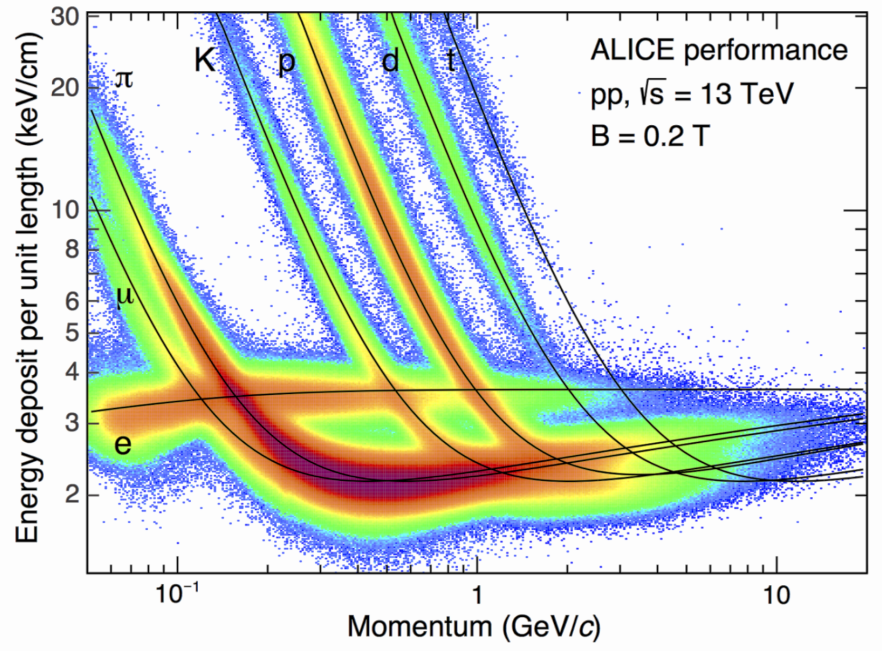

Figure 3.6: The measured specific energy loss dE/dx is depicted as a function of particle momentum for various particle types. The solid lines show the theoretically expected energy loss curves. The figure is taken from ALICE (2015).

The energy loss depends only on the charge, the velocity of the particle and on physical properties of the traversed medium. At ALICE one employs an empirical parameterization of Bethe-Bloch formula given by the ALEPH equation:

$$F(\beta\gamma) = \frac{P_1}{\beta^{P_4}} \left(P_2 - \beta^{P_4} - ln(P_3 + (\beta\gamma)^{-P_5}) \right), \tag{3.1}$$

where the parameters P_i depend on temperature, pressure and gas composition in the TPC (Blum et al., 2008).

Particle identification (PID) becomes possible when one expresses the measured energy loss signal (i.e. charge accumulated in pad clusters) as a function of particle momentum $p = \beta\gamma \cdot m$. The ALICE TPC performance of energy loss measurement is shown in fig.3.6. One can select species of a certain kind i by evaluating the number of standard deviations n_σ^i defined as

$$n_\sigma^i \equiv n_{\sigma_{TPC}}^i = \frac{\frac{dE}{dx}\Big|^i_{\text{meas}} - \frac{dE}{dx}\Big|^i_{\text{theo}}}{\sigma^i_{TPC}} \tag{3.2}$$

where $\frac{dE}{dx}\Big|^i_{\text{meas}}$ and $\frac{dE}{dx}\Big|^i_{\text{theo}}$ are measured and expected energy loss values for a certain particle

species, σ^{i}_{TPC} is the corresponding measured resolution. For this analysis we perform PID by constraining $|n_{\sigma}| < 4$.

The dE/dx resolution for hadronic observables such as protons, kaons, pions and their anti-particles reaches theoretical limit of $\sim 5\%$ and decreases with increasing number of reconstructed TPC clusters (Lippmann, 2012). The track matching for hadrons is performed at $85 - 95\%$ efficiency level, dependent on the particle transverse momentum.

4

Event and track selection

4.1 Data sets and event selection

For this work we analyse pp collisions at the centre-of-mass energy $\sqrt{s} = 13$ TeV. The data was acquired in the second running period (Run 2) during the years 2015–2018. The analysis is performed completely with the **E**vent **S**ummary **D**ata (ESD), which stores event properties and full information about tracks.

Our analysis begins with a selection of events. There are around 6.4×10^9 recorded events of pp collisions at a 13 TeV centre-of-mass energy. However, we pre-select only those events for further analysis which surpass the standard selection put by AliPhysics class *AliEventCuts*. The constraints are the following:

1. **Trigger**: only minimum bias (MB) events are processed. The chosen MB trigger flag is kINT7, i.e. event information is based on a measurement with the VZERO counter (Bhasin et al., 2010). This general purpose trigger has high efficiency for low and high multiplicity events and stores information about diffractive events, too. Moreover, events that originate due to beam-gas interactions in the beam pipe are vetoed, i.e. only real pp-collisions are selected Conrad et al. (2005).

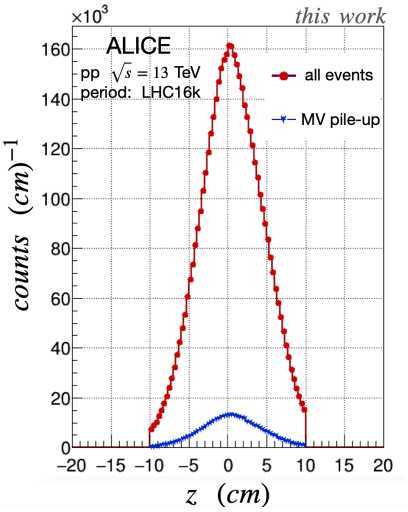

(a) Position of z-coordinate of the primary vertex measured for the period LHC16k. The multi-vertex (MV) pile-up events constitute $\sim 5 - 10\%$ fraction of the whole event sample and are discarded in this analysis.

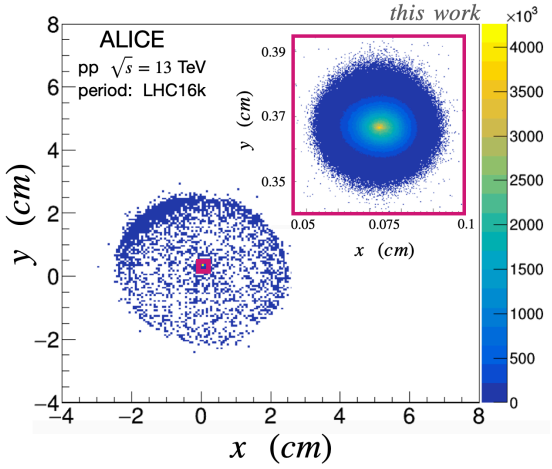

(b) Position of the primary vertex in the x-y plane as measured for the period LHC16k with subtracted MV-pile up events. The lower left panel shows the whole measured sample. The upper right plot depicts the zoomed region (rectangle in lower panel) with 99.9% of the events

Figure 4.1: Distribution of spatial positions of the primary interaction vertex for selected events.

2. **Vertex position**: it is checked whether a vertex spatial position can be reconstructed for a given event, i.e. if any tracklets were reconstructed by SPDs. In a positive scenario, the z-coordinate is constrained to the central $|z| < 10$ cm, see Fig. 5.2a. No cuts are applied on the vertex position in the x-y plane, see Fig. 5.2b.

3. **Vertex properties**: the z-coordinate needs to have a low dispersion $\sigma_Z < 0.25$ cm, where σ_Z is the fit value of the standard deviation of the z_v distribution. The coordinate z_v is the intersection of the SPD tracklets with the beam axis (Report, 2005).

This procedure abandons nearly 70% of MB events and nearly 1.7×10^9 events may be used for cascade finding. Among these events, around 10% are multi-vertex (MV) pile-up events. In this work the MV pile-up events are disregarded.

4.2 Track selection

For each event stored in the ESD, there is an associated saved list of tracks (ESD tracks), as well as lists of V0 particles (e.g. Λ and K^0_S) that are accessed via the class *AliESDV0*; and of cascade candidates (e.g. $\Xi^{\pm}$ and $\Omega^{\pm}$) that are stored as objects of the class *AliESDcascade*. The selected events (as described in previous section 4.1) are processed further by the class *AliAnal-*

ysisTaskWeakDecayVertexer which refits the V0 and cascade events, see section 5.2. The refit candidates are pre-selected by the task *AliAnalysisTaskStrangeCascadesDiscrete*, which was written for this analysis and being a part of the AliPhysics library. The output file represents a collection of event and cascade properties and has a structure of ROOT object TTree. Our task is based on the task *AliAnalysisTaskStrangenessVsMultiplicityRun2* but has a nested output TTree object, where *nested* means that the basic object of the tree is a pp collision event with all relevant information. For each event we save the information about the correspoding cascade candidates. Our task demands that at least one cascade candidate (AliESDcascade object) is stored in the event. Moreover, it imposes additional track and topology based selections in order to suppress misidentified hyperons. During the cascade pre-selection we used slightly looser cuts than those for the analysis. A motivation for this was to enable systematic studies for a broader parameter space. While the topological cuts are subject of chapter 5, the track-based selection is presented in this section.

The daughter particles are reconstructed in the central pseudo-rapidity range $|\eta| < 0.8$. This ensures that track lengths of all charged daughter candidates lie inside the TPC active volume. The Ω candidates are reconstructed in the mid-rapidity region $|y| < 0.5$. The minimum transverse momentum of the daughter tracks was selected to be at least $p_T \geq 150$ MeV/c.

No ITS-related cuts were applied in the daughter track pre-selection. However, we store the ITS information for each track: hits on ITS layers, information about shared clusters and layer status. For the analysis, the following ITS criteria were applied. If the radial decay position R in the global coordinate frame of either Λ or Ω candidate lies within the ITS SPD2 layer, $R < 7.6$ cm, the corresponding charged daughters need to be refitted inside the ITS. The ITS-refit is crucial since it improves track momentum and position resolution and suppresses background. If the radial position of secondary vertices is further away from the primary vertex than the radius of the SSD2 layer, $R > 43.1$ cm, then no ITS-refit is required. Alternatively, a false ITS-refit flag is required to be assigned to that track whose total number of hits inside the ITS N_{hits} is zero. Charged daughters originating at secondary vertices inside the first SPD layer, R < 3.9 cm, need to have at least one hit in either of the SPD layers. For secondaries with R > 3.9 we demand that the total number of hits N_{hits} is at least one.

It can occur that two tracks have one or more ITS clusters in common. These clusters are called *shared*. We select only those secondaries with R < 3.9 that have at least two unshared clusters. If the secondary decay vertex outside of the SPD2 layer and before the first SSD layer, the charged track needs to have at least one unshared cluster. When the V0 or cascade candidate decays radially further away than the SSD1 layer, the corresponding tracks must

not have any shared clusters.

Furthermore, consistency cuts are implemented in order to decrease the number of misidentified tracks. If a candidate (Λ or Ω) decays beyond the SPD1 layer $R > 3.9$ cm, there should be no hits on this layer fired by corresponding charged daughters. Similarly, hits are found in neither SPD1 or SPD2 layers if the decay vertex is further away than the SPD2 layer $R > 7.6$ cm.

All tracks are refitted in the TPC. Secondary tracks with a kink topology, e.g. semi-leptonic decays of charged kaons or pions, are discarded. The number of reconstructed TPC clusters is kept at least 70 out of possible 159. In the analysis, we used only those tracks with at least 80 TPC clusters. This cut helps to reject fake tracks and to improve both the momentum resolution of high energy particles and the dE/dx resolution (Lippmann, 2012; ALICE, 2020). The ratio of reconstructed TPC clusters to findable TPC clusters is kept at least $N_{cls}/N_{find} > 0.6$, where the number of the findable clusters is evaluated as a geometrically possible number of TPC hits for a given track. For the analysis, we tightened this cut up to $N_{cls}/N_{find} > 0.8$. Moreover, the track quality was assured by imposing a selection cut on the TPC tracking $\chi^2/N_{clusters} < 4$. The PID was performed by the TPC only. During the candidate pre-selection, we constrained the number of dE/dx standard deviations to $n_\sigma < 4$ for each daughter track. For the analysis, the cut was tightened to $n_\sigma < 3$. The cuts used for selection and analysis are summarized in table B.1.

Kinematics	**Selection**	**Analysis**
Pseudorapidity of daughter tracks $\|\eta\|$	< 0.8	< 0.8
Rapidity of Ω candidate $\|y\|$	< 0.5	< 0.5
Daughter momentum	$p_T \geq 150$ MeV/c	$p_T \geq 150$ MeV/c
ITS	**Selection**	**Analysis**
ITS refit flag	any	TRUE, if R < 7.6 cm FALSE, if R > 43.0 cm FALSE, if $N_{\text{hits}} = 0$
Hits in SPD layers	any	SPD1=1 or SPD2=1, if R < 3.9 cm SPD1=0, if 3.9 cm $<$ R < 7.6 cm SPD1=0 and SPD2=0, if R > 7.6 cm
Shared clusters	any	$N_{\text{hits}} - N_{\text{shared}} \geq 2$, if R < 3.9 cm $N_{\text{hits}} - N_{\text{shared}} \geq 1$, if 3.9 cm $<$ R < 38 cm $M_{\text{shared}} = 0$, if R > 38 cm
TPC	**Selection**	**Analysis**
TPC refit flag	TRUE	TRUE
Kink flag	FALSE	FALSE
Reconstructed TPC clusters N_{TPC}	> 70	> 80
Reconstructed to findable cluster ratio $\frac{N_{\text{TPC}}}{N_{\text{findable}}}$	> 0.6	> 0.8
Track quality χ^2_{red}	< 4	< 4
TPC PID dE/dx n_σ	< 4	< 3

Table 4.1: Track selection and analysis cuts

5

Cascade reconstruction

The Ω hyperon is the objective of this work. The Ω baryon decays entirely via the weak interaction and therefore traverses rather long distances ($c\tau = 2.43$ cm) in the detector volume before its subsequent decay into secondary particles. This is advantageous because the spatial resolution of the ITS of order ~ 100 μm is enough to resolve the secondary decay vertex of the Ω candidate.

With almost 70 % chance the Ω particle decays into a pair of strange particles - an electrically charged kaon and a neutral Λ hyperon. The Λ hyperon propagates straight line segments of order ca. 10 cm completely invisible to the ITS and TPC and, with a branching ratio of ca. 64%, decays weakly in a V-shaped pair of charged tracks - a proton and a pion. Particles which decay in this manner are called V0's, where 0 stands for the electric charge.

The reconstruction of the Ω candidates in the golden decay channel, i.e. $\Omega^- \rightarrow \Lambda(p\pi^-)K^-$ and for the anti-particle $\bar{\Omega}^+ \rightarrow \bar{\Lambda}(\bar{p}\pi^+)K^+$, is performed by combining the ITS and TPC tracking and PID capabilities and taking into account a pronounced decay topology.

Figure 5.1a depicts the PID capabilities of different detectors at ALICE. One can see that generally the hadron separation π/K and K/p is possible only for low momenta up to $\sim$

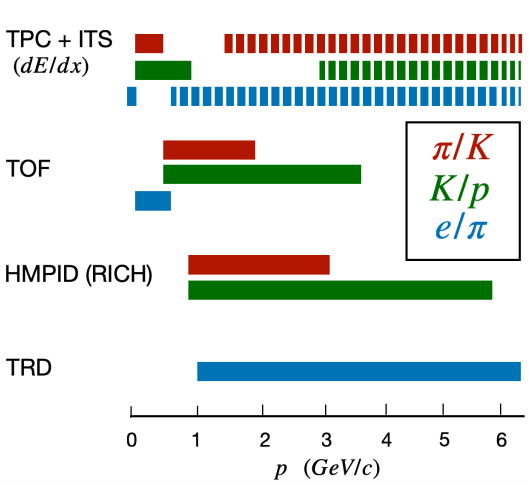

(a) Schematic view of particle identification performance at ALICE. This figure is taken and slightly adapted from Botta (2017).

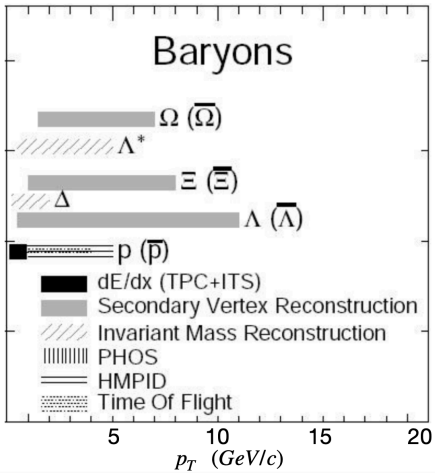

(b) Estimation of strategy for reconstruction of different baryons with ALICE. This figure is taken and slightly adapted from Kraus (2009).

Figure 5.1: Schematic overview of PID capabilities of ALICE.

0.6 GeV/c and 1 GeV/c, respectively. This is due to an overlap of the characteristic dE/dx curves of different particle species. In principle, a clean particle separation could be possible if additional information provided by the Time-Of-Flight (TOF) detector could be used. However, TOF is calibrated to detect particles coming from the primary vertex and not from secondary vertices of hyperon decays (Carnesecchi, 2019). Furthermore, the TOF detector has a lower acceptance, i.e. this lowers the signal yield. Therefore, we neglect any measurement with the TOF detector in current analysis. What makes the reconstruction of the Ω baryons possible even for high momenta, is the prominent decay topology, see Fig. 5.2. The reconstruction of hyperons strongly relies on the reconstruction of the secondary vertex, Fig. 5.1b. The efficiency of the cascade finding depends drastically on other topological variables, too.

This chapter is dedicated to the topological variables and the selection of corresponding values, and is structured as follows. Section 5.1 outlines the strategy of the cascade finding at ALICE. Section 5.2 describes special features of the hyperon reconstruction in Run 2. Section 5.3 is dedicated to the detailed description of various topological observables. A summary table 5.2 with the values of topological variables used for the pre-selection and the analysis encloses this chapter.

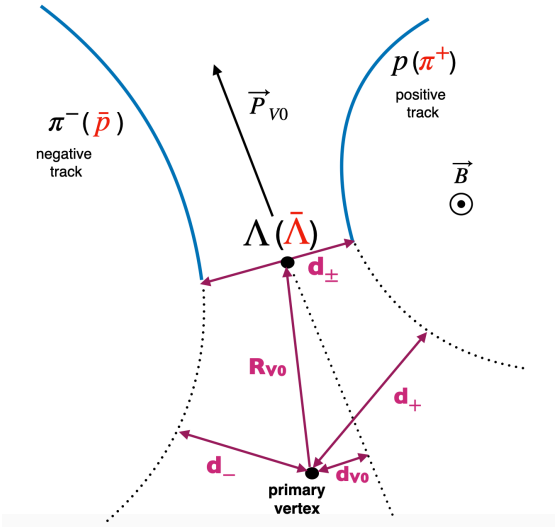

(a) Decay of the Λ hyperon into a proton and a pion in the vicinity of the magnetic field. The daughter tracks curl in the magnetic field and therefore have some (non-negligible) distance (d_-, d_+) to the primary vertex.

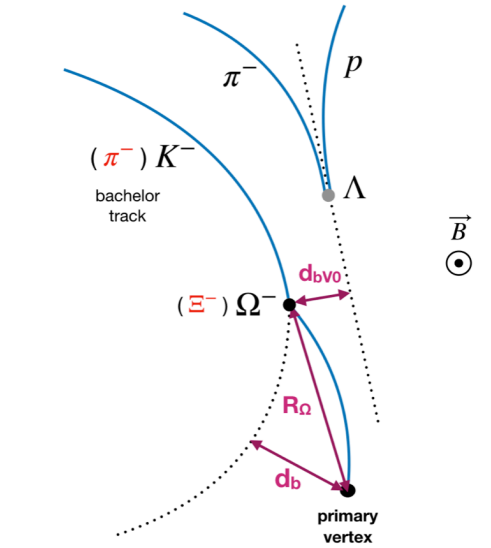

(b) Decay of the Ω hyperon into ΛK. The letters in bracket denote the related cascade decay $\Xi \rightarrow \Lambda\pi$ which has a similar topology.

Figure 5.2: Schematic visualisation of the topology in the V0 and cascade decays.

5.1 General cascade finding with ALICE

In this work we deal with the cascade reconstruction which is done off-line. The hyperon finding procedure is performed on an event-by-event basis and begins with a finding of V0 candidates. One proceeds in the following way. A general V0 particle decays in a pair of oppositely charged tracks. To find the V0 candidate, one combines positive and negative tracks in a combinatorial manner. Primary particles are rejected by selecting only those tracks that have the distance of closest approach (DCA) to the primary vertex larger than some predefined value. Then, each two V0 candidates are propagated to each other, i.e. to their DCA d_{pn}. The maximum cut-off value of d_{pn} is usually dictated by the spatial resolution of the DCA σ_{pn}, i.e. $d_{pn} < 1 - 2\,\sigma_{pn}$. The position of the V0's secondary vertex $\vec{R}_{V0}$ in the global coordinate frame is evaluated as the weighted mean of the tracks' spatial points propagated to the corresponding DCA (d_{pn}). The impact parameter d_{V0} is calculated as a DCA between the reconstructed vertex position and a prolongation of V0 track (a straight line). The information about each V0 is saved to the ESD as members of the *AliPhysics* software class *AliESDV*0.

When all V0 candidates have been reconstructed for a given event, the cascade finding takes

over. The algorithm searches for a *bachelor* track candidate, i.e. $K^{\pm}$ in case of $\Omega^{\pm}$. A bachelor track is a secondary particle and hence its DCA to the primary vertex d_b is bigger than some predefined value. The impact parameter between each pair of a bachelor track and a V0 candidate d_{bV0} is smaller than a cut value. The decay position of the resulting cascade candidate is therefore determined as a weighted mean of the bachelor and V0 tracks' position at the DCA d_{bV0}. The charge of the cascade is fixed by the charge of the corresponding bachelor daughter. The cascade candidates are saved to the ESD. Information about them can be obtained via accessing objects of the *AliPhysics* class - *AliESDcascade*.

5.2 Reconstruction in Run II

In Run 2, it was shown that the properties of the off-line reconstructed cascades did not agree with those predicted by MC simulations.

The major problem was the erroneous determination of the impact parameter between positive and negative tracks. When the distance between centers of helix curves in the x-y-plane is smaller than the corresponding sum of radii, two minima are possible, see Fig. 5.3a.

At one minimum the positive and negative tracks propagate away from each other. One calls it a *sailor* configuration. At another minimum the tracks are curved towards each other - this is a *cowboy* configuration. Since all particle tracks are saved closest to the primary vertex, the standard V0 reconstruction routine would result in an overabundance of cowboy tracks.

In order to obtain a corrected sample of candidates, we needed to recreate (= reset and revertex) the V0s and cascade lists by running the task *AliAnalysisTaskWeakDecayVertexer* before the actual analysis task. Apart from doing the sailor-cowboy fix, this script propagates the bachelor track along the helix curve (a propagation along the straight line is used per default) and therefore identifies the Ω decay vertex more precisely. The latter plays a crucial role when reconstructing the Ω baryons with large transverse momenta and/or those candidates which propagate long distances before subsequent decays.

5.3 Topological selection

5.3.1 Distance of closest approach

In order to find the DCA between a track and any other object, be it a primary vertex or another track, one needs to propagate the track to the object. Equations 5.1-5.2 show how the DCA to the primary vertex is found for a charged track inside a magnetic field and for a

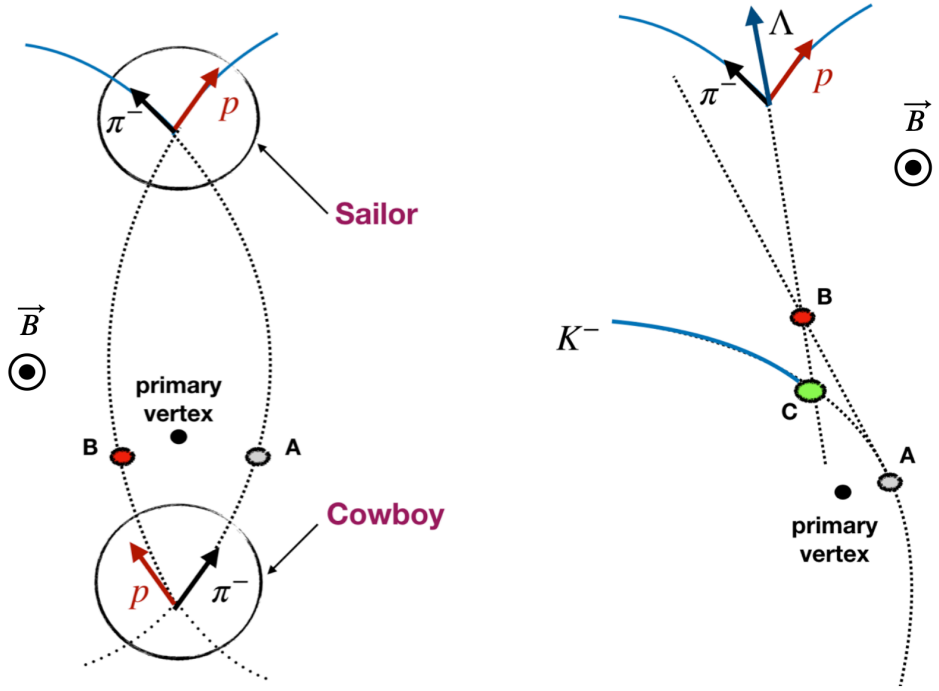

(a) Schematic representation of the cowboy-sailor topology. The points A and B depict the DCAs of the corresponding tracks of a $\pi^- i$ and p to the primary vertex. A minimization algorithm searches for the DCA between the tracks starting from the points A and B. The first (closest to the primary vertex) found minimum is assigned as the DCA.

(b) Correct propagation of the bachelor track. Point A denotes the spatial point of the DCA of the bachelor track to the primary vertex. If the bachelor track is propagated along the straight line, the cascade decay vertex is reconstructed as the point B. However, the right decay position given by the point C is usually smaller, and is obtained when the curvature of the bachelor track is taken into account.

Figure 5.3: Visualisation of topological properties which were corrected manually in the Run 2 hyperon reconstruction.

straight line track (e.g. V0 candidate). It is practical to differentiate between the transverse component of the DCA d_t and the z-component d_z because the ITS-TPC spatial and momentum resolution in the transverse plane is substantially better than along the beam axis. In this work we refer to the cut values on different DCAs as cuts on the transverse components only, it not stated explicitly otherwise.

$$d_T(r\varphi) = \begin{cases} \rho - \sqrt{(x_0 - x_v)^2 + (y_0 - y_v)^2}, & |Q| \geq 1 \\ (\vec{R} - \vec{R}_v) \times \hat{p}_T, & Q = 0 \end{cases} \tag{5.1}$$

$$d_z(z) = z_{track} - z_v, \tag{5.2}$$

where Q is the charge of the track in units of the elementary charge; (x_v, y_v, z_v) and $\vec{R}_v = (x_v, y_v, 0)$ is the position vector of the reconstructed primary vertex; (x_0, y_0) is the centre of the track in the transverse plane to the beam direction, $\vec{R}$ is the radial position of the track in the global coordinate frame, $\hat{p}_T$ is the direction vector of the transverse momentum; ρ is the curvature of the track given by the bending radius in the magnetic field; and z_{track} is the z-coordinate of the track propagated to the point of closest approach, see Fig. 5.4.

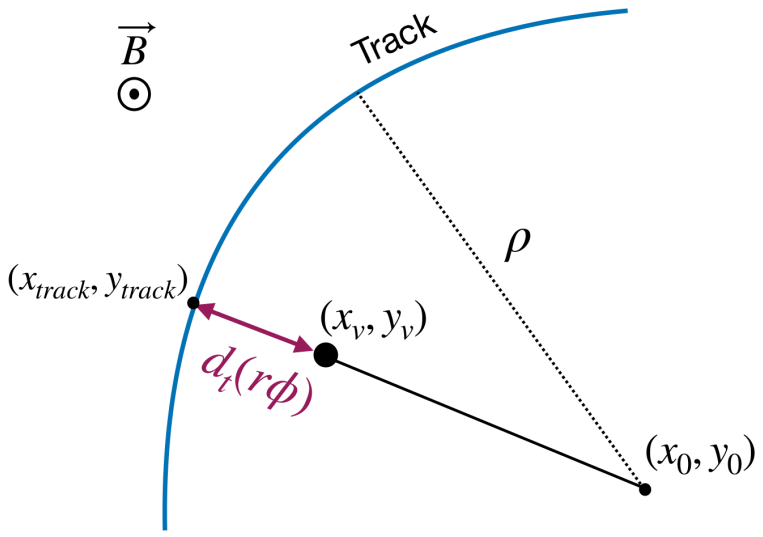

Figure 5.4: Schematic sketch of the estimation of the distance of closest approach between a charged particle's track in a magnetic field and the primary vertex.

In the pre-selection procedure we constrained the transverse component to $d_T > 0.03$ cm

for all charged tracks. For the analysis the cuts were tightened. The meson daughter of the Λ particle carries less momentum than the baryon daughter. Thus, the meson has a smaller bending radius in the magnetic field than the baryon track, and consequently a larger value of the DCA. We set $d_{meson} > 0.20$ cm, $d_{baryon} > 0.10$ cm and $d_{bachelor} > 0.05$ cm. The threshold value of DCA of the bachelor track is chosen to be the smallest as the bachelor daughter is produced closest to the primary vertex. No cuts were set on the values of the total DCA between the Λ particle and the primary vertex d_{V0} during the pre-selection routine. However, in the analysis we constrained the values of d_{V0} to be larger than 0.04 cm. Setting this cut helps to reject primary V0 candidates.

The DCA between two tracks is determined as a minimum of the weighted distance

$$d^2_{tracks} = \min \sum_{i=1}^{3} \frac{\omega_i (r_i^A - r_i^B)^2}{\omega_i} \tag{5.3}$$

where superscripts A and B stand for two tracks, the index i goes through the spatial coordinates (1="x", 2="y", 3="z"). The weights ω_i are defined as $\frac{1}{\omega_i} = \sigma^2_{A,i} + \sigma^2_{A,i}$ where $\sigma^2_{A,i}$ and $\sigma^2_{B,i}$ are the variances of spatial coordinate i of the corresponding tracks A and B. The variances are extracted from the track covariance matrix. It is assumed that $\omega_1 = \omega_2$ holds. For the estimation of the distance d_{tracks} a minimization algorithm is used which implements the Newton's optimization method.

For our pre-selection we chose the following values: $d_{pn} < 1.4\ \sigma_{pn}$ for the DCA between positive and negative tracks, with $\sigma^2_{pn} = \sigma^2_A + \sigma^2_B$. In the analysis we tightened the value up to $d_{pn} < 1.0\ \sigma_{pn}$. The value of the total DCA between the bachelor track and the V0 candidate was constrained by an upper limit $d_{bV0} < 1.0$ cm.

5.3.2 Secondary vertex and decay radius

Multi-strange particles decay weakly, hence they traverse distances which generally can be resolved by the detector system. The position of the secondary vertex $\vec{D}_{decay}$ is evaluated as a spatial point of the DCA of decay products in the global coordinate frame. In order to account for the real flight distance, one needs to shift the $\vec{D}_{decay}$ by the position of the primary vertex $\vec{D}_{PV}$ in case of a cascade candidate, and - by the position of the cascade decay - in case of the Λ candidate.

Due to the spatial resolution, one usually studies the decay radii in the transverse plane rather than decay distances. The radial distance R of the Ω and Λ particles are then calculated

as:

$$R_\Omega = |\vec{R}_{decay,\Omega} - \vec{r}_{PV}| \tag{5.4}$$

$$R_\Lambda = |\vec{R}_{decay,\Lambda} - \vec{R}_{decay,\Omega}|, \tag{5.5}$$

where $\vec{r}_{PV} = (x_{PV}, y_{PV}, 0)$.

It is important to point out that the track of the Ω particle is bent in the vicinity of the magnetic field. Rigorously, one should account for this effect when calculating the decay radius and the total flight distance. However, it can be shown that the ratio of the approximated (a straight line trajectory) R_Ω to the real bent radial flight distance R_{real} is given by

$$\frac{R_\Omega}{R_{real}} = \mathrm{sinc}\left(\frac{\alpha}{2}\right), \quad \alpha = \frac{0.3B}{M_\Omega} c\tau_{exp} \left[\frac{\mathrm{GeV}}{\mathrm{T}\cdot\mathrm{m}}\right] \tag{5.6}$$

where m, B and τ_{exp} are the central mass, the magnetic field and the determined proper life time, respectively. For example, if we demand a cut $c\tau_{exp} < 3 \cdot c\tau$ and use $M_\Omega = 1.672$ GeV/c^2 and B = 0.5 T, we obtain a mean distance difference $< |R_\Omega - R_{real}| > \approx 1\,\mu$m for all preselected Ω candidates. This difference still cannot be resolved by the ITS. Thereupon, we neglect the bending of the charged mother hyperon in our analysis.

When selecting the candidates, we demand that the secondary vertices of the Λ and Ω baryons are at least 1.1 cm and 0.6 cm away from the primary vertex, respectively. The minimal decay length is controlled by the radius of the beam pipe $\sim$ 0.6 cm. The cascade reconstruction efficiency drops drastically therein.

5.3.3 Cosine of pointing angle

In order to quantify whether a particle comes from the primary vertex or not, one usually determines a pointing angle which is defined as the angle between a particle momentum $\vec{p}$ and the flight distance from primary vertex. The flight distance vector is determined as the difference between the reconstructed decay position $\vec{D}$ and the reconstructed position of the primary vertex $\vec{D}_{PV}$. It is practical to work with the cosine of the pointing angle, expressed as

$$\cos\Theta_{\mathrm{pointing}} = \frac{\vec{p}\cdot(\vec{D} - \vec{D}_{PV})}{|\vec{p}|\cdot|\vec{D} - \vec{D}_{PV}|} \tag{5.7}$$

One expect $\cos\Theta_{pointing} \approx 1$ for particles originating from the primary vertex and for those

the bending in the magnetic field can be neglected, see Fig. 5.5. Since the cascades are produced at the primary vertex, we constrained the cosine of pointing angle $\cos\Theta_\Omega > 0.95$. For the analysis, we tightened up the value up to $\cos\Theta_\Omega > 0.99$.

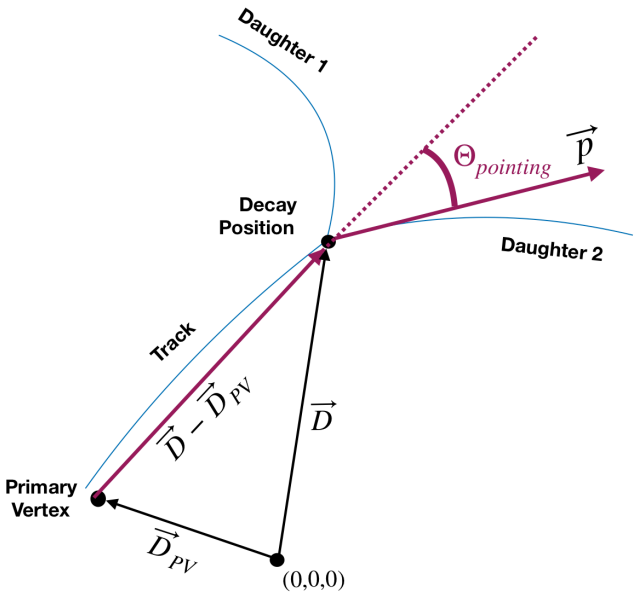

Figure 5.5: Schematic decay of a particle into two daughter tracks (blue dotted lines) is sketched. The momentum of the mother particle is $\vec{p}$ and the distance $\vec{D}$ from the coordinate origin. The reconstructed position of the primary vertex on an event-by-event basis is given by the vector $\vec{D}_{PV}$. Note: the track does not have to originate from the primary vertex.

We also accounted for the pointing angle of the Λ candidate. Since it is a secondary particle and does not need to point back to the primary vertex (especially at low momenta), the lower cut on the pointing angle was chosen to be looser than that of Ω baryon. For the candidate pre-selection we use $\cos\Theta_\Lambda > 0.90$; in the analysis, we cut at $\cos\Theta_\Lambda > 0.95$.

5.3.4 Proper life-time

The mean life-time of decaying particles τ_{exp} can be determined as

$$c\tau_{exp} = \frac{mL}{p} = \frac{mR}{p_T}, \tag{5.8}$$

where m is central mass value of the particle under consideration, L and R are the total and the radial distances (from creation vertex to the decay vertex), respectively; p and p_T are the total and transverse momenta, respectively. In this analysis, we decided to put constraint on

the mean time of the Λ and Ω candidates to be smaller than $4 \cdot c\tau_\Lambda$ and $3 \cdot c\tau_\Omega$, where the values of masses and mean life time τ are taken from Table 5.1.

The cut on the proper life time helps to reject misidentified hyperon candidates, especially those mismatches which occur at large distances from the primary vertex.

5.3.5 Cascade rejection

The Λ and Ω hyperons are not the only particles which possess the special topology discussed in chapter 5. The $\Xi^{\pm}$ baryon decays in a very similar manner to the Ω particle, i.e. $\Xi^- \rightarrow \Lambda\,\pi^-$ with the corresponding branching ratio equal to 99.9%. The decay $K^0_S \rightarrow \pi^+\pi^-$ has a similar topology to that of the Λ decay studied in this analysis. Table 5.1 summarizes the properties of weakly decaying strange baryons.

Hadron	Valence quarks	Mass [MeV/c^2]	Decay channel	BR [%]	cτ [cm]
Ω^-	sss	1672.45	ΛK^-	67.8	2.43
Ξ^-	dss	1321.71	$\Lambda\pi^-$	99.9	4.92
Λ	uds	1115.68	$p\pi^-$	63.9	7.89
K^0_S	$\frac{d\bar{s}-\bar{d}s}{\sqrt{2}}$	497.65	$\pi^+\pi^-$	69.2	2.67

Table 5.1: Some properties for cascades and V0 particles. The shown decay channel depicts daughter particles which are reconstructed in this analysis.

A clear Ξ/Ω and Λ/K^0_S separation would be only possible if p/K and π/p (or π/K) separations could be done in the whole energy range. Due to the limited PID capabilities of the ITS+TPC detector system, it is not possible, see Fig. 5.1a. Therefore, one needs to deal with a hyperon *hypothesis*. For a general V0 candidate (K^0_S or Λ), we calculate the invariant mass as:

$$M_{inv}(\mathrm{V0}) = \left[(\sqrt{m^2_{pos} + \vec{p}^{\,2}_{pos}} + \sqrt{m^2_{neg} + \vec{p}^{\,2}_{neg}})^2 - (\vec{p}_{pos} + \vec{p}_{neg})^2\right]^{\frac{1}{2}} \qquad (5.9)$$

where lower superscripts *pos* and *neg* stand for the positive and negative daughters of V0. If the hypothesis of the V0 candidate is the Λ particle, then the mass of the positive track is equal to the mass of positive kaon, the mass of the negative track - to the mass of negative pion. For the anti-particle $\bar{\Lambda}$ the mass assignments of the negative and positive tracks are interchanged. In case the V0 candidate is hypothesized to be a K^0_S candidate, both tracks are assigned the mass of the charged pion.

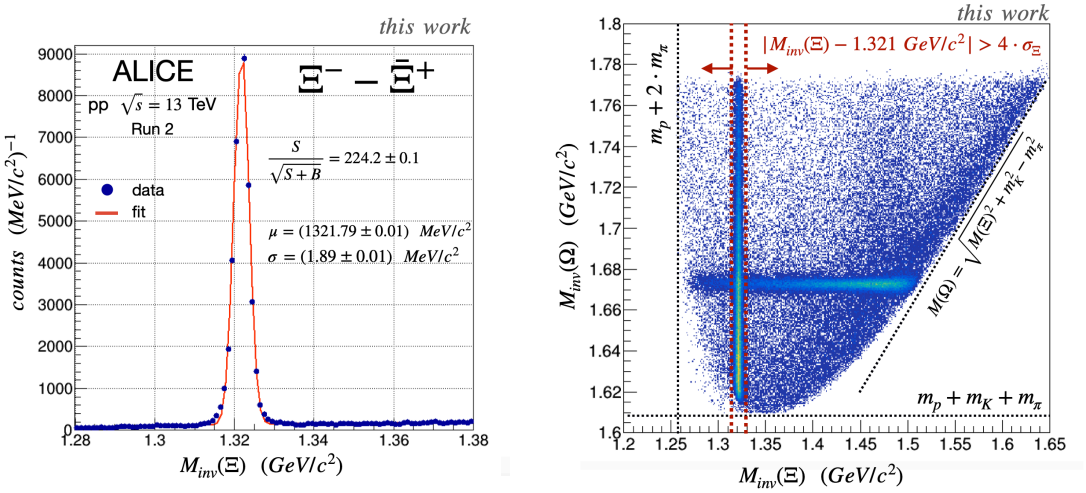

(a) Invariant mass spectrum of the Ξ particles. The signal is fit with a Gaussian and a linear background function. The estimated width of the peak, σ, is used further as a central measure for the Ξ rejection.

(b) Invariant mass of the Ω particles as a function of the reconstructed invariant mass of the Ξ candidates. The pink region depicts the area of invariant mass space which is rejected when performing analysis on the Ω hyperons.

Figure 5.6: Cascade rejection. Invariant mass spectra of the Ξ/Ω particles

The mass of a general cascade candidate ($\Xi^\pm$ or $\Omega^\pm$) is determined in a similar way:

$$M_{inv}(\text{Casc}) = \left[\left(\sqrt{m_\Lambda^2 + \vec{p}_{\text{V0}}^2} + \sqrt{m_{bach}^2 + \vec{p}_{bach}^2} \right)^2 - (\vec{p}_{\text{V0}} + \vec{p}_{bach})^2 \right]^{\frac{1}{2}}, \qquad (5.10)$$

where $\vec{p}_{V0} = \vec{p}_{pos} + \vec{p}_{neg}$, the mass m_Λ is the central (pdg) mass of the Λ hyperon. The mass of the bachelor track m_{bach} is either chosen to be that of the kaon (Ω hypothesis) or - of the pion (Ξ hypothesis). In order to select a clean signal sample, we select the Λ and Ω candidates in the mass windows $|M_{inv}(\Lambda) - 1116\,\text{MeV/c}^2| < 8\,\text{MeV/c}^2$ and $|M_{inv}(\Omega) - 1672\,\text{MeV/c}^2| < 100$ MeV/c^2, respectively.

The K/π misidentification plays a crucial role in the analysis of the cascade mass spectra. The $\Xi - \Omega$ baryon mass difference is nearly the same as the difference of the corresponding bachelor particles, i.e. $m_\Omega - m_{\Xi^\pm} \approx m_K - m_\pi = 350\,MeV/c^2$. This implies, that misidentified bachelor pions which originate from real $\Xi^\pm$ decays can "echo" in the invariant mass distribution of Ω.

Figure 6.1b shows the determined invariant mass of a cascade candidate with the Ω-hypothesis as a function of the mass evaluated with the Ξ-hypothesis. One can see that there is a region in $M(\Omega) - M(\Xi)$ space where a cascade candidate cannot be identified. The admixture of Ξ candidates in the Ω candidate sample contribute around $1 - 2\%$ to the clean Ω signal at

$p_T > 2$ GeV/c. For our precision measurement the purity of the Ω signal is essential. Therefore, we need to perform a cascade rejection. We reject all tracks which contribute both to the $\Xi^{\pm}$ and Ω mass peaks. This is done by imposing the cut $|M_{inv}(\Xi) - M_{PDG,\Xi}| < 8\,MeV/c^2$. The threshold value of $8\,MeV/c^2$ is chosen as a $4\cdot\sigma$ deviation from the Ξ invariant mass mean value, see Fig. 6.1a.

We face a similar situation when dealing with Λ/K^0_S misidentification which in turn arises in regime where p/π separation is not possible with TPC, i.e. for momenta $p > 2$ GeV/c. The K^0_S yields are low in comparison to those of Λ due to the Λ-mass window selection. Hence,the K^0_S-rejection is not performed for the analysis but is left as a subject for systematic studies.

Topological variable	Pre-selection	Analysis
DCA of the baryon track to PV, d_{baryon}	> 0.03 cm	> 0.10 cm
DCA of the meson track to PV, d_{meson}	> 0.03 cm	> 0.20 cm
DCA of the bachelor track to PV, d_b	> 0.03 cm	> 0.05 cm
DCA of V0 to PV, d_{V0}	any	> 0.04 cm
DCA positive to negative tracks, d_{pn}	$< 2.0\sigma$	$< 1.0\sigma$
DCA of the bachelor track to V0, d_{bV0}	< 2.0 cm	< 1.0 cm
Λ decay radius, R_Λ	> 0.6 cm	> 1.1 cm
Ω decay radius, R_Ω	> 0.6 cm	> 0.6 cm
Λ cosine of pointing angle, $\cos PA_\Lambda$	> 0.90	> 0.95
Ω cosine of pointing angle, $\cos PA_\Omega$	> 0.95	> 0.99
Λ proper life-time, $c\tau_{exp,\Lambda}$	any	$4\cdot c\tau_\Lambda$
Ω proper life-time $c\tau_{exp,\Omega}$	any	$3\cdot c\tau_\Omega$
Λ-mass window, $\lvert M_{inv}(\Lambda) - 1116$ MeV/c$^2\rvert$	< 8 MeV/c^2	< 6 MeV/c^2
Ω-mass window, $\lvert M_{inv}(\Omega) - 1672$ MeV/c$^2\rvert$	< 100 MeV/c^2	< 100 MeV/c^2
Competing Ξ-rejection, $\lvert M_{inv}(\Xi) - 1321$ MeV/c$^2\rvert$	any	> 8 MeV/c^2
Competing K^0_S-rejection, $\lvert M_{inv}(K^0_S) - 498$ MeV/c$^2\rvert$	any	any

Table 5.2: Topological selection used during the pre-selection routine and in the analysis. The flag *any* means that no cut was done on a topological variable.

6
Analysis

The aim of this ananlysis is to extract the invariant mass of the Ω^- and $\bar{\Omega}^+$ baryons with an unprecedented precision and, subsequently, perform the CPT test.

The invariant mass spectrum M_{inv} is assumed to be described by a Gaussian distribution with a mean value $\mu = M_\Omega$ and standard deviation σ; the latter is regulated completely by the detector response. There are no contributions from the Wigner energy distribution because $\Gamma_\Omega = \frac{\hbar}{\tau_\Omega} \approx 1\,\mu$eV which cannot be resolved by the ALICE detectors.

Performing a single Gaussian fit on the whole collected Ω sample is not suitable for our precision measurement because σ of the distribution is not a constant parameter. This would result in a distribution with non-vanishing higher order moments (skewness, kurtosis etc.) which generally might shift the position of the mean value and are not easy to be accounted for when a rigorous mathematical description of the distribution is needed. Instead, we subdivide our collected sample in smaller "portions". We perform a p_T-dependent invariant mass fit. In order to do this, we fit the invariant mass spectrum in subsequent p_T-bins of the Ω candidate. The Ω candidates are reconstructed in the range $p_T \in [0.6, 6]$ GeV/c. The first p_T-bin starts at 0.6 GeV/c and has the width of 200 MeV/c. All other p_T-bins are 100 MeV/c wide, which results in a total number of 53 bins.

The track and topological cuts applied on the candidates are those given in the right columns of tables B.1 and 5.2 and are treated as momentum and energy independent quantities. We refer to these values as *central* cuts.

For each p_T-bin, we fit the invariant mass spectrum with a function which is a sum of a Gaussian curve and a background function. The latter is defined as a polynomial of the second order. When fitting data with the Software ROOT, it is important to estimate the fitting parameters before the actual fit. In case of the Gaussian distribution, we first make a "guess" of the central (mean) mass value μ_0 and the standard deviation σ_0. In the Ω analysis we set $\mu_0 = M(\Omega)_{PDG} = 1672.5$ MeV/c^2 and $\sigma_0 = 2.0$ MeV/c^2. In order to estimate the parameters of the background function, we first set all the parameters equal to zero and fit the background in the range:

$$\text{Background range:} \quad (\mu_0 - 10\sigma_0, \mu_0 - 6\sigma_0) \div (\mu_0 + 6\sigma_0, \mu_0 + 10\sigma_0) \tag{6.1}$$

The estimated parameters from this procedure are used further to perform the combined fit of the signal and background which is done in the range:

$$\text{Signal range:} \quad (\mu_0 - 4\sigma_0, \mu_0 + 4\sigma_0) \tag{6.2}$$

In order to ensure the stability of the fitting procedure, we allow the estimate of the mean value $\hat{\mu}$ to deviate by 0.1% from the μ_0 and use integrals of fitting function in corresponding bins instead of estimating the function value at the corresponding bin center. The fit employs the least square minimization (MLS) algorithm. The uncertainties of each bin are given by the square root of the bin content. When the fitting is performed successfully, the signal is refitted by setting the fit values μ_{FIT} and σ_{FIT} into the ranges according to Eqs. 6.1 and 6.2.

The total signal T is extracted as a sum of bin contents in a range $\mu_{FIT} \pm 3\sigma_{FIT}$. The (clean) signal yield S is determined by subtracting the background function estimated at the center of the bins from the content of the corresponding bins. The background estimate is $B = T - S$. Plot 6.1 shows an example of the fit in a given p_T-bin. The statistical uncertainty of the mean is defined by $\bar{\sigma}_{FIT} = \frac{\sigma_{FIT}}{\sqrt{S}}, S \gg 1$.

As a next step, we plot the set of mean values $\{\mu_{FIT} \pm \bar{\sigma}_{FIT}\}$ as a function of p_T, setting the central p_T value to be the center of the corresponding momentum bin. The result thereof is depicted in Fig. 6.2. One can see that the invariant mass values rise with increasing p_T in the range $0.6 - 2$ GeV/c with a subsequent mass plateau $p_T \in\sim [2, 6]$ GeV/c. The "mass rising" effect originates both from an increased energy loss of low energy particles (–

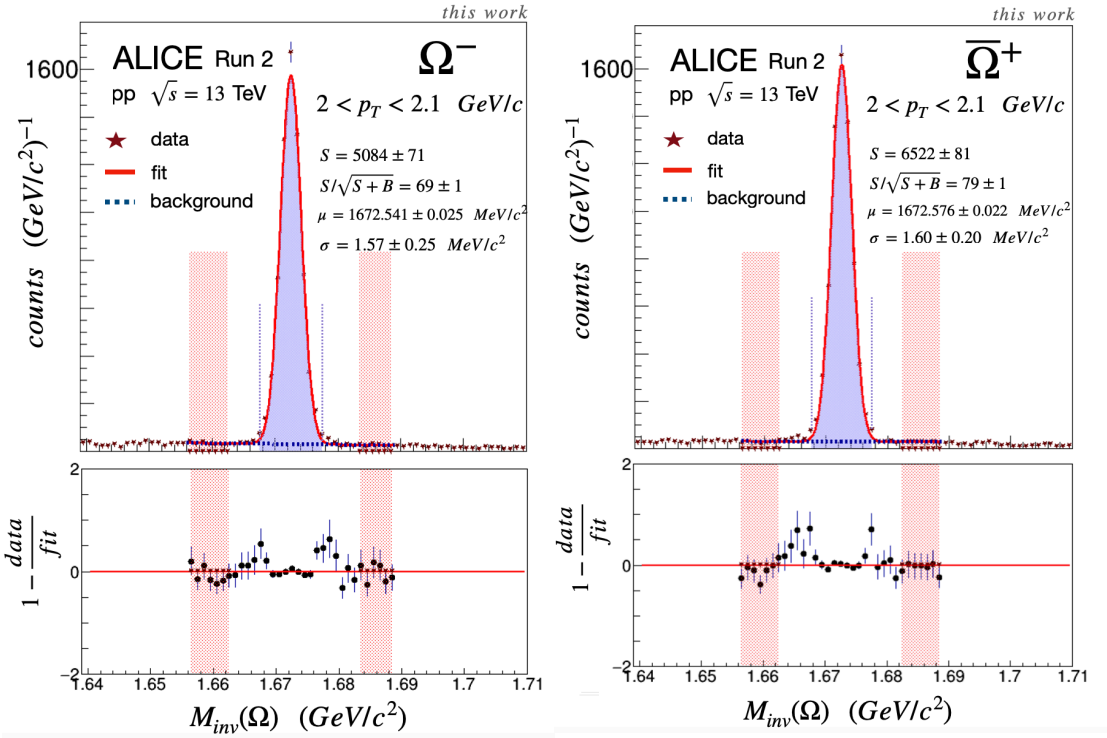

(a) Mass spectrum of the Ω^- baryons

(b) Mass spectrum of the $\bar{\Omega}^+$ baryons

Figure 6.1: Invariant mass spectrum of the Ω hyperons depicted for a selected p_T-bin.

dE/dx $\sim$ $1/\beta^2$) in a material and from the multiple scattering. In order to account for the multiple scattering, one describes the angle scattering with two Gaussian distributions with different widths. The Gaussian distribution which corresponds to the multiple scattering has a substantially wider width for low-momentum particles than for high-momentum particles. For the latter the multiple scattering becomes negligible. This introduces an asymmetry into the invariant mass distribution of the low-momentum particles and hence, - a shift of the mean mass values towards smaller values.

Currently, the effect of multiple scattering cannot be fixed. Therefore, we ignore the mass values in the range $0.6 - 2$ GeV/c. The mass plateau region $2 < p_T < 6$ GeV/c is fit with a constant parameter C, $M(p_T) = C$, by employing the MLS method. The estimate of value $\hat{C}$ and its uncertainty $\sigma_{\hat{C}}$ are hence computed as:

$$\hat{C} = \frac{\sum_i \mu_i/\bar{\sigma}_i^2}{\sum_k 1/\bar{\sigma}_k^2} \tag{6.3}$$

$$\sigma_{\hat{C}}^2 = \frac{1}{\sum_k 1/\bar{\sigma}_k^2}, \tag{6.4}$$

with $\mu_i = \mu_{i,FIT}$ and $\bar{\sigma}_i = \bar{\sigma}_{i,FIT}$ are the fit mean and the standard deviation; the indices i and k run over the p_T-bins falling into the (chosen) plateau region (Cowan, 1998). The final result is obtained by setting $M_\Omega = \hat{C}$ and $\sigma_\Omega = \sigma_{\hat{C}}$. Figures 6.2a and 6.2b depict the intermediate results obtained for the $\Omega^\pm$ candidates of the whole collected data sample. The collected clean sample of the Ω^- and Ω^+ events used for the fit in the plateau range is 101452 and 104469, respectively.

The average weighted mass of the Ω baryon obtained by the fit in the plateau region is $\bar{M}_{\Omega^-+\bar{\Omega}^+} = 1672.5934 \pm 0.0061$ MeV/c^2, where the weighting factors are chosen to be $\omega_i = 1/\sigma_i^2, i \in \{\Omega^-, \bar{\Omega}^+\}$. The deviation between the determined average mass value and the central world average value, i.e. no uncertainty of the latter considered, is $\Delta M_\Omega = 163 \pm 6$ KeV/c^2. This positive mass offset motivated us to analyse its origin in more detail.

In order to analyse the invariant mass bias, we proceeded as follows. If the mass offset is present due to an ill-defined track reconstruction procedure or any detector calibration effects, the mean mass of other particles determined by the fit in a plateau range should also be shifted in a similar manner. The best candidate to analyse is the Λ hyperon because its mass is measured with a much higher precision than those of the Ω and Ξ baryons. Therefore, we performed the similar fitting procedure on the sample of the daughter $\Lambda + \bar{\Lambda}$ baryons, see Fig. 6.3. For the Λ analysis, we chose the p_T-bin width to be 200 MeV/c. It is straightfor-

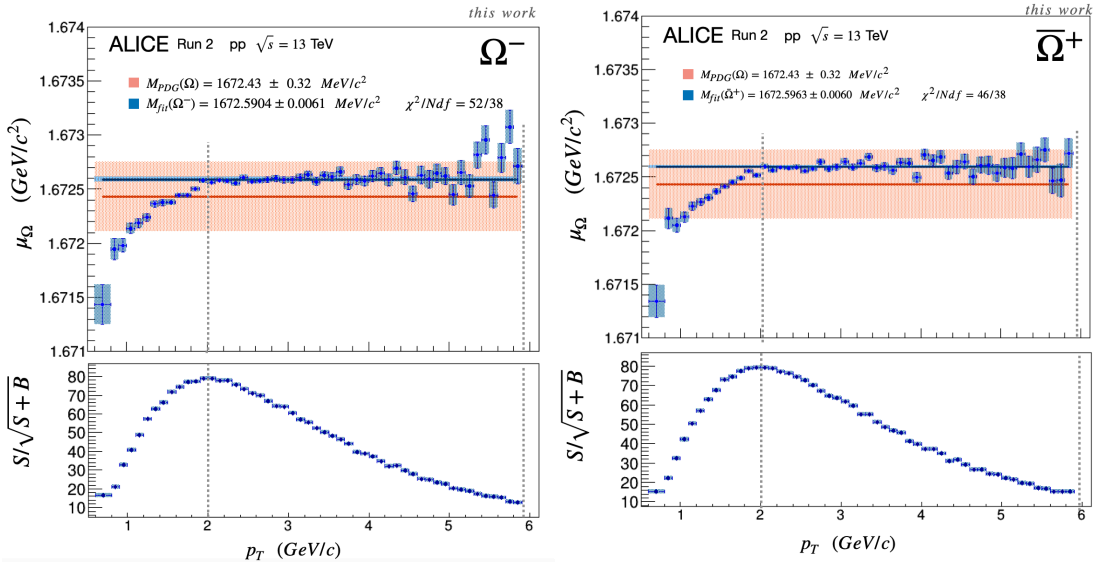

(a) Invariant mass spectrum of the Ω^- baryons

(b) Invariant mass spectrum of the $\overline{\Omega}^+$ baryons

Figure 6.2: Mean mass distribution of the Ω hyperons as a function of the transverse momentum p_T. The results are obtained for the initial Ω sample.

ward to see that the positive shift in the invariant mass spactrum is present in the Λ sample, too. Consequently, one deals with a systematic bias. Moreover, the determined average mass $\bar{M}_{\Lambda+\bar{\Lambda}} = 1115.9751 \pm 0.0040$ MeV/c^2 deviates from the so far best measured average Λ mass by $\Delta M_\Lambda = 292 \pm 7$ keV/c^2, where the uncertainty $\sigma_{\Delta M}$ is evaluated as a square root of a quadratic sum of individual uncertainties. The deviation ΔM_Λ is significant. This encouraged us to try to fix this bias.

Figure 6.4 shows the mean mass spectrum of the Λ and $\bar{\Lambda}$ samples combined as a function of the Λ momentum p_T, plotted for different radial positions of the Λ decay vertex in the global coordinate frame. The left panel 6.4a depicts the case when the mass bias is present. The right panel 6.4b shows the mass spectrum after the correction of the bias has been applied. One can clearly infer from Fig.6.4a that the mass offset depends on the radial position of the secondary vertex of Λ candidates. Only if the Λ candidate decays before the first SPD layer, the mass plateau reaches the world average Λ mass value. Moreover, the dramatic mass dependence on the radial distance of the low-energy Λ candidates ($p_T \leq 1$ GeV/c) indicates that we deal with an effect due to a possible energy loss correction.

Indeed, the observed behaviour might be explained as the correction of energy loss dE/dx in the ITS and the beam pipe. A general track reconstruction routine uses the Kalman algorithm and starts at the outer wall of the TPC where tracking *seeds* are searched for (Belikov

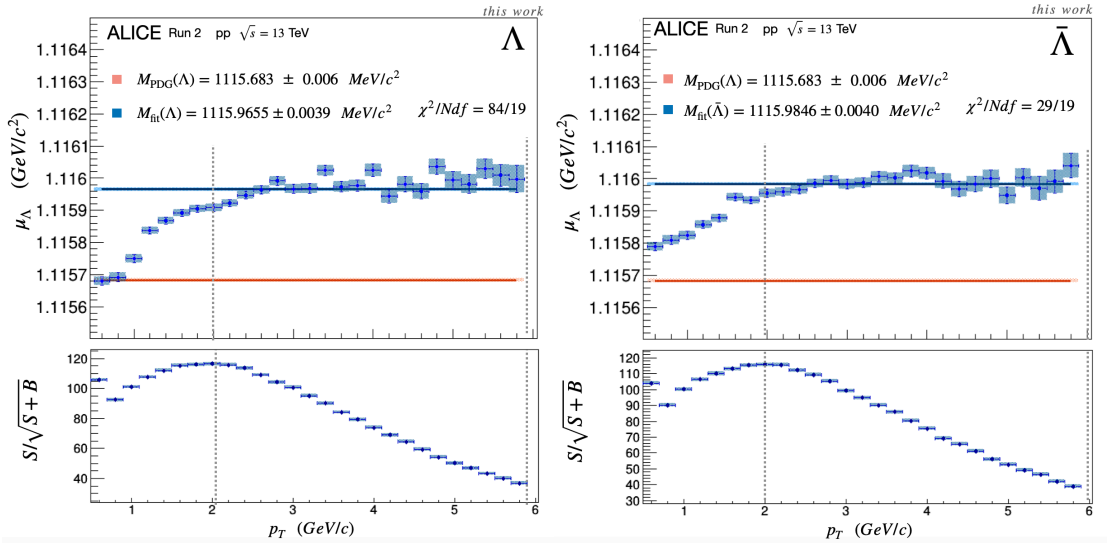

(a) Invariant mass spectrum of the Λ hyperons

(b) Invariant mass spectrum of the $\bar{\Lambda}$ hyperons

Figure 6.3: Mean mass distribution of the daughter Λ hyperons as a function of the transverse momentum p_T. The daughter particles are handled as primaries by the Kalman tracker.

et al., 1997). The track is then propagated inwards to the primary vertex. The first estimate of the particle momentum is done during the first stage of the track reconstruction inside the TPC. The default tracking algorithm considers each particle to be a primary particle and thus corrects for the energy loss dE/dx in the ITS material and the beam pipe material.

If the energy of a particle inside TPC is given by E_0, then the energy E_1 at the primary vertex is estimated as $E_1 = E_0 + dE$, where dE is the value of the energy lost along the whole track length inside the ITS. Accordingly, the momentum of the track is scaled by a factor f:

$$f = \frac{|\vec{p}_1|}{|\vec{p}_0|} = \sqrt{1 + \frac{dE(2E_0 + dE)}{p_0^2}} \geq 1, \tag{6.5}$$

where $|\vec{p}_0|$ and $|\vec{p}_1|$ are the total particle momenta as reconstructed by the TPC and rescaled when propagating to the primary vertex, respectively. Since the total energy loss of a track inside the ITS cannot be measured by all 6 layers, the value of dE is estimated as:

$$dE = \frac{dE}{dx} \cdot \langle \rho \rangle \cdot L, \tag{6.6}$$

where $\frac{dE}{dx}$ is the average energy loss per distance in silicon, $\langle \rho \rangle$ is the mean length-density of material "seen" by a track and L is the length segment of the track inside the ITS. The value

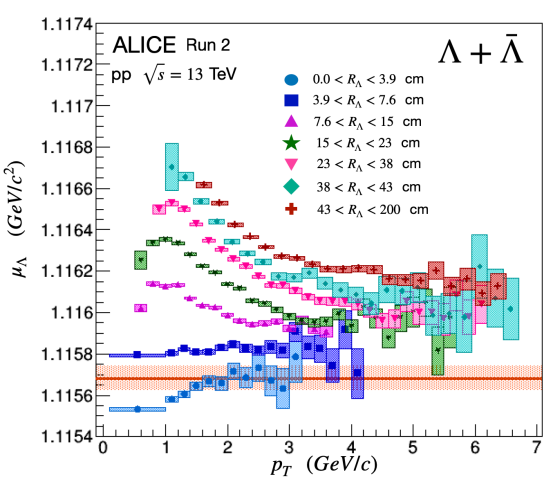

(a) Daughter particles are handled as primaries by the Kalman tracker

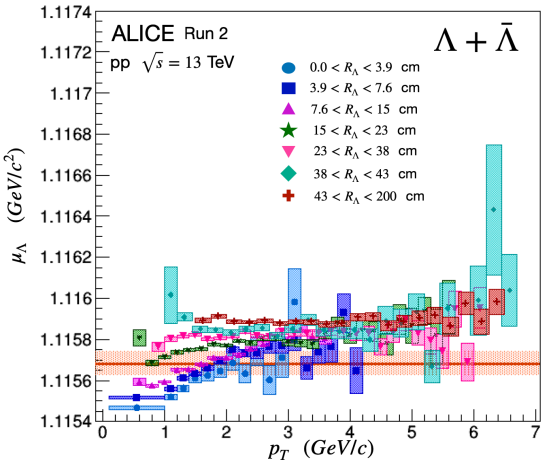

(b) Momenta of the daughter particles are rescaled as to account for overestimated energy loss correction inside the ITS material

Figure 6.4: Mean mass of the combined Λ and $\bar{\Lambda}$ spectrum as function of transverse momentum shown for different radial distances of the secondary Λ position.

of L is calculated as the length of a straight line. The track mass hypothesis, needed for the calculation of E_0, is based on the PID information measured by the TPC. Furthermore, it is assumed that the energy loss affects every component of a particle's momentum in the same way, i.e. one scales every component of $\vec{p}_0$ with the factor f and direction is not changed.

Although this procedure is reasonable for primaries, it is not applicable for secondary tracks originating at measurable distances away from the primary vertex. Therefore, we try to correct the energy loss scaling. We proceeded as follows. We assumed that all three daughter tracks were correctly assigned to a cascade candidate and there was no need to perform a cascade finding from scratch because the expected energy rescaling is a minor effect on a decay topology and the secondary vertex position should not change significantly. We start with a positive-negative track pair and perform the following steps:

- We propagate each track to the primary vertex and store the total momentum p and the spatial X_{primary} coordinate of the track at the DCA to the primary vertex. No momentum rescaling is performed at this point.

- Both tracks are propagated to each other to the point of DCA with momenta p_1. Improved propagation as described in section. 5.2 is implemented. At this step we store information about the coordinate $X_{\text{secondary}}$.

- Each track is propagated from X_{primary} to $X_{\text{secondary}}$ using the method of the AliPhysics

class AliTrackerBase: *AliTrackerBase::PropagateTo*. When tracks are propagated outwards, i.e. $X_{\text{secondary}} > X_{\text{primary}}$ which is our case, the sign of the total energy loss is reversed $dE \rightarrow -dE$, see Fig.6.5a. This is reasonable because we subtract the amount of energy once added manually to the track. Hence the right decay momentum (referred to as *real* in Fig. 6.5)) is determined as:

$$\vec{p}_{real} = \vec{p}_1 \cdot f_{corr} = \vec{p}_1 \cdot \sqrt{1 - \frac{dE(2E_1 - dE)}{p_1^2}} \leq 1 \tag{6.7}$$

- the energy-rescaled tracks are propagated their DCA with *real* momenta starting at the DCA to the primary vertex, see Fig.6.5b. No further energy corrections are done at this step. The newly obtained V0 (member of *AliESDv0*) is saved and used further for the energy loss corrections of the Ω particles.

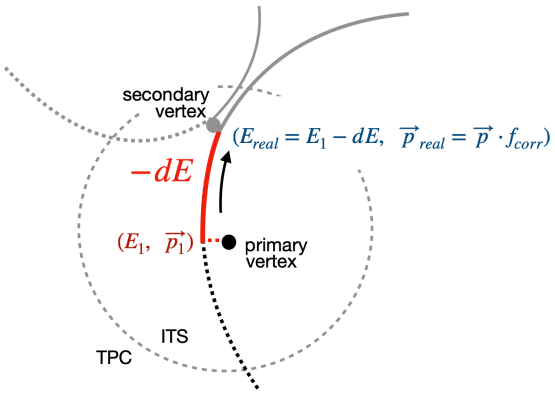

(a) In the first step we determine the DCA of a track to the primary vertex d_{primary} and DCA of this track to the secondary decay vertex $d_{\text{secondary}}$. When propagating the track to the DCA of the secondary vertex, we subtract the energy dE which was initially added to the track by the default tracking algorithm.

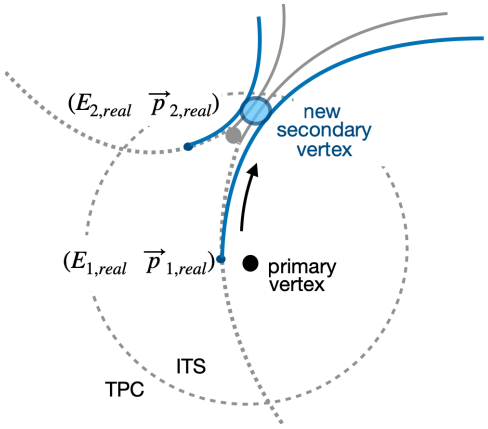

(b) After the energy dE is estimated and subtracted, we start again at the DCA of the primary vertex, however, with rescaled momentum p_{real} for each track. Generally, p_{real} is smaller or equal to the initial momentum. A new value of the DCA of two tracks is determined.

Figure 6.5: Sketch of the energy correction procedure performed for the daughter tracks.

Consequently, we need to apply energy corrections also on the bachelor track. The steps are analogous to those described above:

- First of all, the bachelor track is propagated to the primary vertex and the X_{primary} coordinate is stored.

- From the primary vertex, the bachelor is propagated to the newly built V0 candidate and $X_{\text{secondary}}$ is obtained. Again, the improved procedure (as outlined in section 5.2) is used.
- The method *AliTrackerBase::PropagateTo* corrects the overestimated energy of the bachelor track when propagating it from X_{primary} to $X_{\text{secondary}}$.
- An energy-corrected cascade candidate is built and stored as the *AliESDcascade* object.

The energy correction procedure is done for all periods, for all saved candidates with kinematic and topological cuts of the pre-selection stage, i.e. left columns of tables B.1 and 5.2. Consequently, the values of kinematic and topological variables are recalculated and set to central cut values.

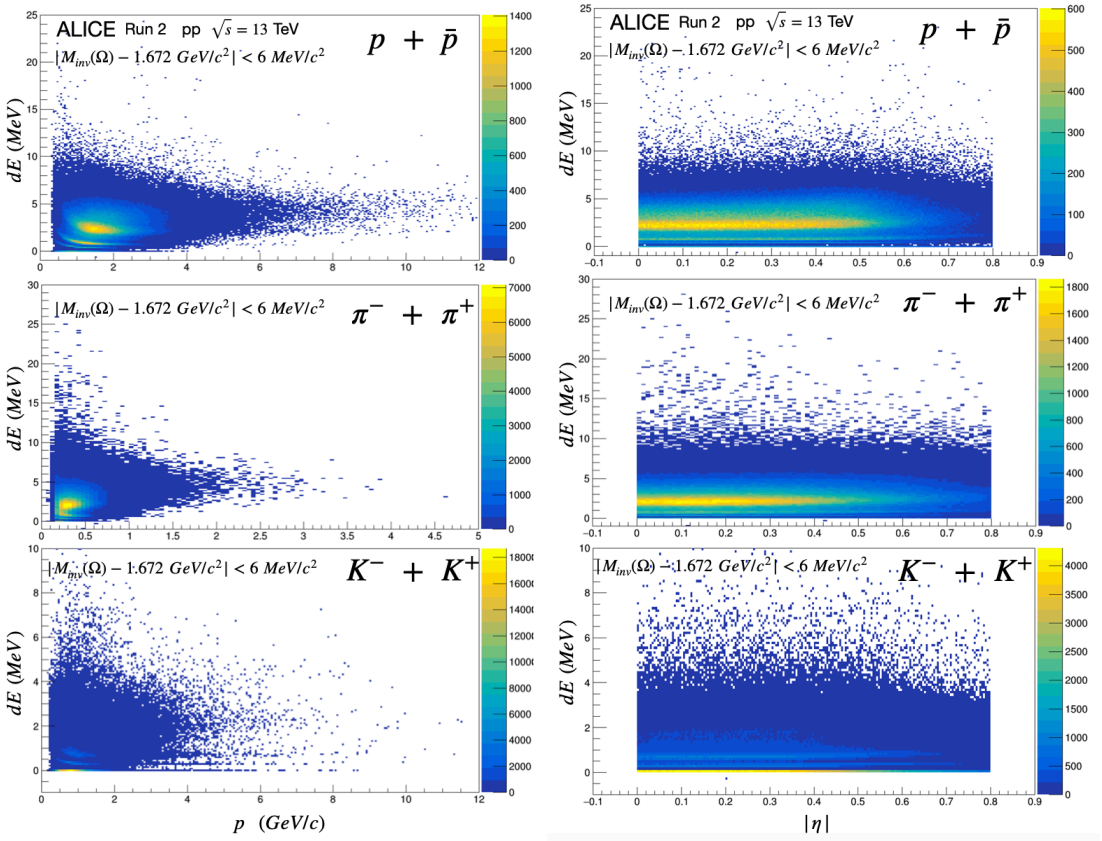

(a) Energy loss as a function of particle momentum.

(b) Energy loss as a function of pseudo-rapidity.

Figure 6.6: Studies of the energy loss correction dE in dependence on the particle momentum and pseudo-rapidity

In order to check, whether the energy correction procedure is coherent, we studied some

properties of the total energy loss $dE = E_1 - E_{\text{real}}$. The left panel of Fig. 6.6 shows the total energy loss as a function of particle momentum.

The energy loss takes the highest values for low-momentum particles, as one would expect from the dependence $-dE/dx \sim 1/\beta^2$. The values of dE saturate at around 2 MeV for protons and pions of $p = 1 - 2$ GeV/c and $p = 0.4 - 0.5$ GeV/c, respectively. For kaons, the saturation happens at values very close to 0 MeV; this could happen due to the position of the Ω secondary vertex being close to the primary vertex. The energy loss becomes higher with increasing particle momentum. This effect might come both from the form of the characteristic Bethe-Bloch curve and from the fact that high-energy daughters come from the high-energy mother particles which, on average, traverse longer distances, i.e. cross more material, before the subsequent decay.

It is appealing to study the corrected energy loss dE as a function of the track inclination angle Θ, too. The motivation here is that tracks with bigger values of Θ cross more material and hence one needs to correct for a larger amount of energy loss. One would expect the dependence $dE \sim 1/\cos\Theta = 1/\sinh\eta$, where η is the pseudo-rapidity of the track. However, the dE values do not decrease with higher values η and stay constant over the whole region, which is illustrated in Fig. 6.6b.

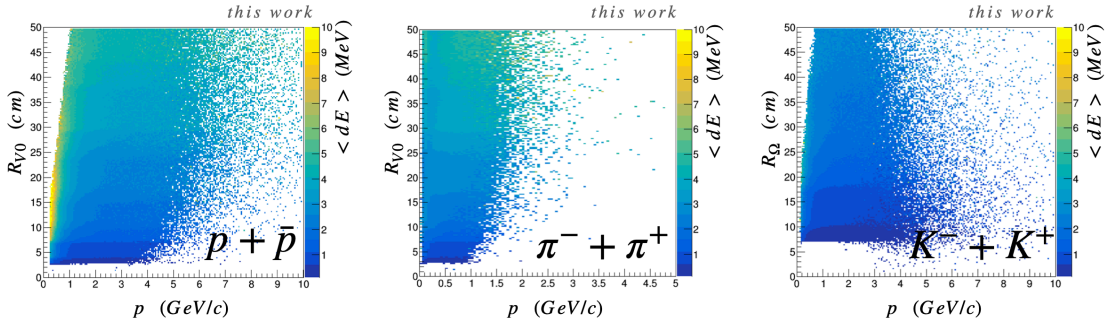

Figure 6.7: The average energy loss $\langle dE \rangle$ as a two-dimensional function of the particle momentum and the position of the secondary vertex.

In order to investigate the combined dependence of the energy loss on the radial distance of the secondary vertex R and particles momentum p, we created the dE maps, see Fig. 6.7. For the map creation we used the data sample with pre-selection cuts as to ensure a higher quality (statistics) of the maps. The minimum value of the depicted average $\langle dE \rangle$ is set to 0.1 MeV. One can easily notice that the bigger dE-correction indeed is applied for the tracks with higher values of radial positions R and higher momenta p.

The mean mass of the energy loss corrected Λ candidates as a function of the momen-

tum p_T is shown in Fig. 6.4b. The mass values decrease dramatically, $400 - 700$ keV/c^2, for $p_T < 2$ GeV/c and take on values very close to the world average M_Λ. For the high-energy Λ candidates, the invariant mass values decrease slightly by $100 - 200$ keV/c^2. The begin of the plateau region starts at $p_T = 5$ GeV/c for the corrected spectrum instead of the previously chosen $p_T = 2$ GeV/c. The overall mean mass of the Λ hyperon in the plateau region turns out to be $M_{\text{corrected},\Lambda} = 1115.8297 \pm 0.0081$ MeV/c^2, which is around 150 keV/c^2 lower than the mean mass value evaluated for the Λ spectrum without dE/dx correction. The difference between $M_{\text{corrected},\Lambda}$ and the world average mass value is still significant. We discuss this result in chapter 7 where we treat it as a mass offset.

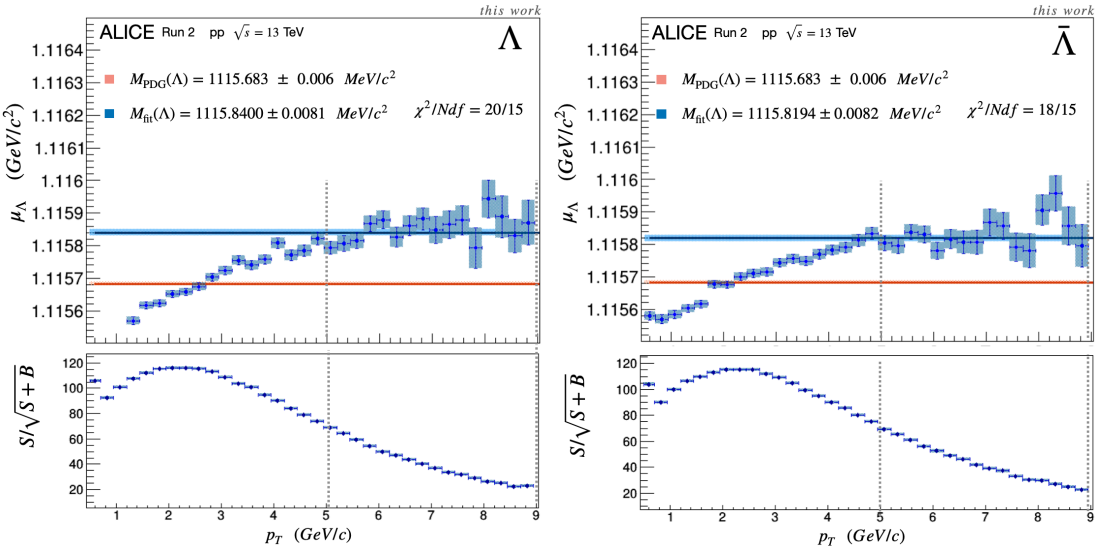

(a) Invariant mass of the daughter Λ particles

(b) Invariant mass of the daughter $\bar{\Lambda}$ particles

Figure 6.8: Energy corrected mean mass distribution of the daughter Λ hyperons.

Although our momentum rescaling procedure is not enough to correct the Λ mass sufficiently, there is still an advantage present in performing the dE/dx rescaling; namely, the resolution of the invariant mass peak. Figure 6.9 illustrates how the width σ of the invariant mass distribution of the Λ and Ω particles changes when the dE/dx-correction is done. It is interesting to note that the overall dependence of the mass resolution on momentum follows the track momentum resolution, see Fig. 3.5. In case of the Λ hyperons, the width decreases in the range $p_T \in [0.5 - 3]$ GeV/c. For higher momenta no clear statement can be made due to the lack of statistics. In case of the Ω baryons, the resolution does not change significantly. A possible explanation could be that the momentum of daughter kaons is not rescaled sufficiently to cause a significant improvement.

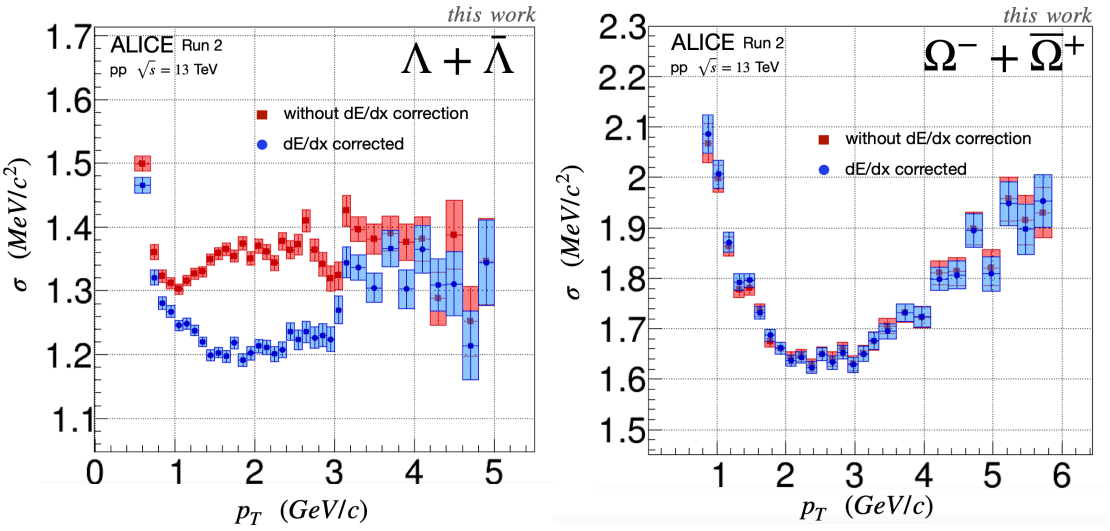

(a) Width distribution of the combined daughter $\Lambda + \bar{\Lambda}$ sample.

(b) Width distribution of the combined $\Omega^- + \bar{\Omega}^+$ spectrum.

Figure 6.9: Width of the mass peak σ, described by the Gaussian distribution, as a function of the particle momentum. The case when no energy loss correction is done on the secondaries is compared to the case when the energy correction is applied on the secondary particles. The analysed Λ hyperons are daughters of the Ω baryons. Hence, they (Λ) decay at larger radii than the mother particle. This leads to a larger correction of the width of the mass distribution.

We proceeded with the analysis of the Ω mass spectrum. The corrected mean mass of the $\Omega^{\pm}$ candidates become $\bar{M}_{\text{corrected},\Omega^-+\Omega^+} = 1672.5402 \pm 0.0061\ \text{MeV/c}^2$, where the given uncertainty is statistical. This is still 18 standard deviations ($\sigma_{M_{corrected}}$) away from the central mean world average value. Nevertheless, we consider this value as the result of this work.

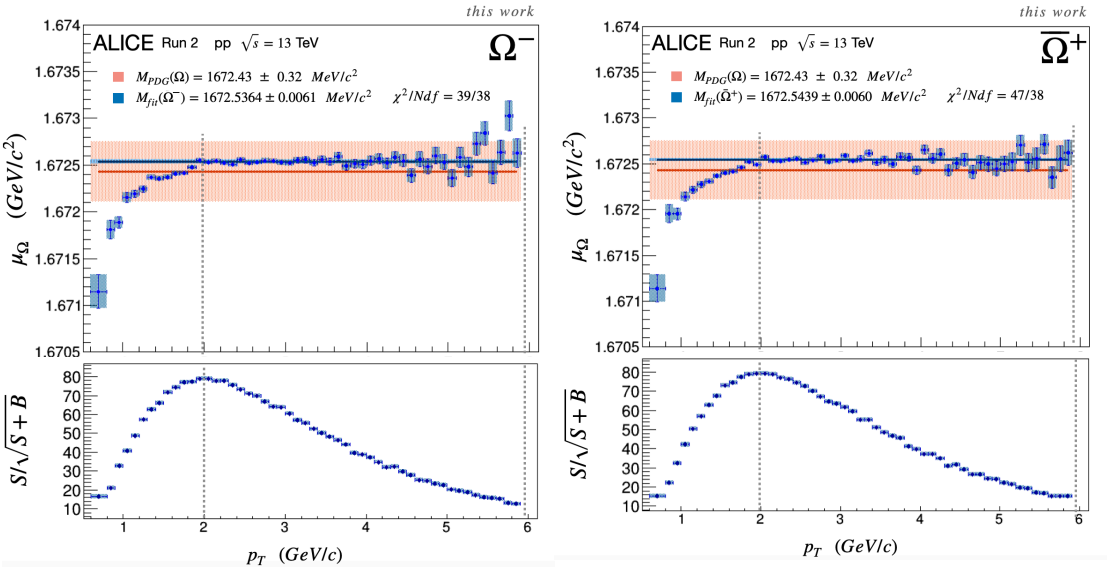

(a) Invariant mass spectrum of the Ω^- particles

(b) Invariant mass spectrum of the $\overline{\Omega}^+$ particles

Figure 6.10: Energy loss corrected mean mass distribution of the $\Omega^\pm$ baryons as a function of the transverse momentum.

7

Systematics studies

This chapter is dedicated to the evaluation of the systematic uncertainties and conduction of the systematic checks of the Ω mass measurement.

Generally, a systematic uncertainty is determined via quantitative comparison of (at least) two measured values obtained from any (at least) two data samples, say S and T. In this analysis for each sample, the set of the mean Ω mass values in different p_T bins $\{\mu_i \pm \bar{\sigma}_i\}_{\mathrm{p_T\ bins}}$ and the mean mass in the plateau region $\bar{M}_{\mathrm{fit}}(\Omega) \pm \bar{\sigma}_{\mathrm{fit}}$ for both Ω^- and $\bar{\Omega}^+$ events are measured, where the latter is computed with the values of the p_T-set:

$$\bar{M}_{\mathrm{fit}}(\Omega) = \frac{\sum_i \mu_i/\bar{\sigma}_i^2}{\sum_k 1/\bar{\sigma}_k^2} \tag{7.1}$$

$$\sigma_{\mathrm{fit}}^2 = \frac{1}{\sum_k 1/\bar{\sigma}_k^2}, \tag{7.2}$$

which is equivalent to the fit with a polynomial of zeroth order.

In terms of the properties of the data samples, we can differentiate two general cases: the samples can be either independent or dependent on each other.

For the case of **independent** samples the evaluation of systematic uncertainty is the follow-

ing. We compare the values $\bar{M}_{\text{fit}}(\Omega)$ directly with each other, i.e. we compute the difference $\Delta M_{\text{fit}} = \bar{M}_{\text{fit}}(\Omega)|_S - \bar{M}_{\text{fit}}(\Omega)|_T$ with the combined uncertainty $\sigma^2_\Delta|_{S\cap T=\emptyset} = \sigma^2_{\text{fit}}|_S + \sigma^2_{\text{fit}}|_T$.

If the relation $\Delta M_{\text{fit}} < 3\cdot\sigma^2_\Delta$ holds, we consider both measured values to be consistent. No systematic uncertainty is needed to be computed. If, on the contrary, $\Delta M_{\text{fit}} > 3\cdot\sigma^2_\Delta$, then we assume that the values $\bar{M}_{\text{fit}}(\Omega) \pm \bar{\sigma}_{\text{fit}}$ are described by a Gaussian distribution alone and investigate whether these individual distributions overlap within 3 standard deviations. If the distributions do overlap, we do not calculate any systematic uncertainty, i.e. $\sigma_{\text{syst}}|_{S\cap T=0}$. For the case when both Gaussian distributions do not overlap we compute the systematic uncertainty as the minimal distance needed to ensure the overlapping. Mathematically, this can be summarized as:

$$\sigma_{\text{syst}}(S\cap T=\emptyset) = (M_S - 3\cdot\sigma_S) - (M_T + 3\cdot\sigma_T), \tag{7.3}$$

where we assume without loss of generality that the mean mass value measured on the subset S is larger than that measured with the sample T.

Any two samples S and T are **dependent** when $S\cap T\neq\emptyset$. This is usually the case when one studies the systematic effects via variation of kinematic and/or topological cuts. In the scenario of the dependent samples we need to proceed differently. It is worth noting that the systematic uncertainty evaluation according to Eq.7.3 will generally result in an underestimate of the underlying systematic effect. This comes from the fact that the estimated values will usually be consistent within their statistical uncertainties because a common shared subsample was used for their determination. In order to account for the common statistics, we proceed in steps described below.

1. For two samples S and T we perform the mass analysis in p_T bins in the central plateau region $p_T \in [2,6]$ GeV/c using the same fitting properties for both samples, i.e. the bin number and widths, signal extraction regions, background function etc.

2. The two obtained sets of values in p_T bins $\{\mu_S \pm \bar{\sigma}_S\}_{\text{p}_\text{T bins}}$ and $\{\mu_T \pm \bar{\sigma}_T\}_{\text{p}_\text{T bins}}$ are compared. This means that for each bin i we determine the deviation $\Delta\mu_i = \mu_{S,i} - \mu_{T,i}$ and the combined uncertainty $\sigma_{\Delta i}$ given by the derived formula:

$$\sigma^2_{\Delta i} = \bar{\sigma}^2_{S,i} + \left(1 - 2\cdot\frac{\sigma^2_{S,i}}{\sigma^2_{T,i}}\right)\bar{\sigma}^2_{T,i}, \tag{7.4}$$

where $\sigma_{S(T),i}$ denote the width of the corresponding Gaussian distribution. For the

full derivation, see Appendix C. We note that Eq.7.4 is consistent with the method described by Barlow (2002). However, we include the dependence on the width of the Gaussian distribution.

3. We fit the set $\{\Delta\mu_i \pm \sigma_{\Delta i}\}$ with a constant parameter in the p_T-range used for the mass plateau analysis. As a result we get the mean mass deviation $\langle\Delta\mu\rangle > \pm\sigma_{<\Delta\mu>}$. The same values of the latter can also be evaluated by Eq.7.1 and 7.2. This calculation is coherent since the values in any two different p_T bins are independent from each other.

4. We check whether the value $\langle\Delta\mu\rangle$ is consistent with zero within the 3 intervals in units of the statistical uncertainty 7.2. If the deviation is significant, the systematic uncertainty σ_{syst} is evaluated as

$$\sigma_{\text{syst}}(S \cap T \neq \emptyset) = |\langle\Delta\mu\rangle| - 3 \cdot \sigma_{\langle\Delta\rangle} > 0. \tag{7.5}$$

Otherwise, the systematic uncertainty is set to 0.

7.1 Systematics in different periods

The first systematic check which we decided to do was to investigate each data sample in individual data taking periods. This is motivated by the fact that the properties of the detector system (calibration, mechanical alignment, magnetic field and others) may be different between each two periods. We fit the invariant mass of the $\Omega^{\pm}$ baryons in the p_T-range from 2 GeV/c up to 6 GeV/c. We could not perform the plateau analysis for each period the way we did for the total collected data sample because the samples are different in size. In order to minimize possible contributions from the statistical fluctuations to the measured mean mass values we decided to ignore the samples with the clean signal yields S at $p_T > 2$ GeV/c with $S < 200$.

We were left with 25 period samples (out of 34) which surpass the signal criterion above. For periods with $1 \cdot 10^3 < S < 5 \cdot 10^3$, we did not perform the plateau fit but instead fit the whole signal in the given p_T range. Thus we accounted for possible statistical fluctuations which could affect the fit result, although the width of the invariant mass peak is not constant over the p_T range. The plateau analysis was done for each period with $S > 5 \cdot 10^3$. Here we differentiated two cases: if $S < 1. \cdot 10^4$, we set the p_T-bin width to 500 MeV/c^2; in case $S > 1. \cdot 10^4$, the bin width was chosen to be 250 MeV/c^2.

The fit mean mass values are depicted in Fig. 7.1. No outlier was found when comparing the evaluated mass values with the world average mass of the Ω hyperon $M_{\mathrm{PDG}}(\Omega)$: all obtained values lie within the total uncertainty (red band in Fig. 7.1) of the $M_{\mathrm{PDG}}(\Omega)$ value.

As a next step, we needed to compare the analysis in individual periods with the results of the plateau fit on the whole sample. To do this, we determined the weighted mean value $M_{\mathrm{periods}}(\Omega)$ of the mass sample shown in Fig. 7.1. The weights ω_i are chosen to be $\omega_i = 1/\overline{\sigma}_i^2$, where $bar\sigma_i^2$ are the statistical uncertainty of the mean values and the index i runs over the whole analysed sample. The standard deviation of the $M_{\mathrm{periods}}(\Omega)$ was evaluated according to Eq. 7.2.

The estimated mean value $M_{\mathrm{periods}}(\Omega)$ lies within the statistical uncertainties of the value $M_{\mathrm{fit}}(\Omega)$ which we obtained in our analysis. The insignificant deviation between both mean mass values indicates that the contribution of the other 9 periods (which were included in the analysis sample) is negligible.

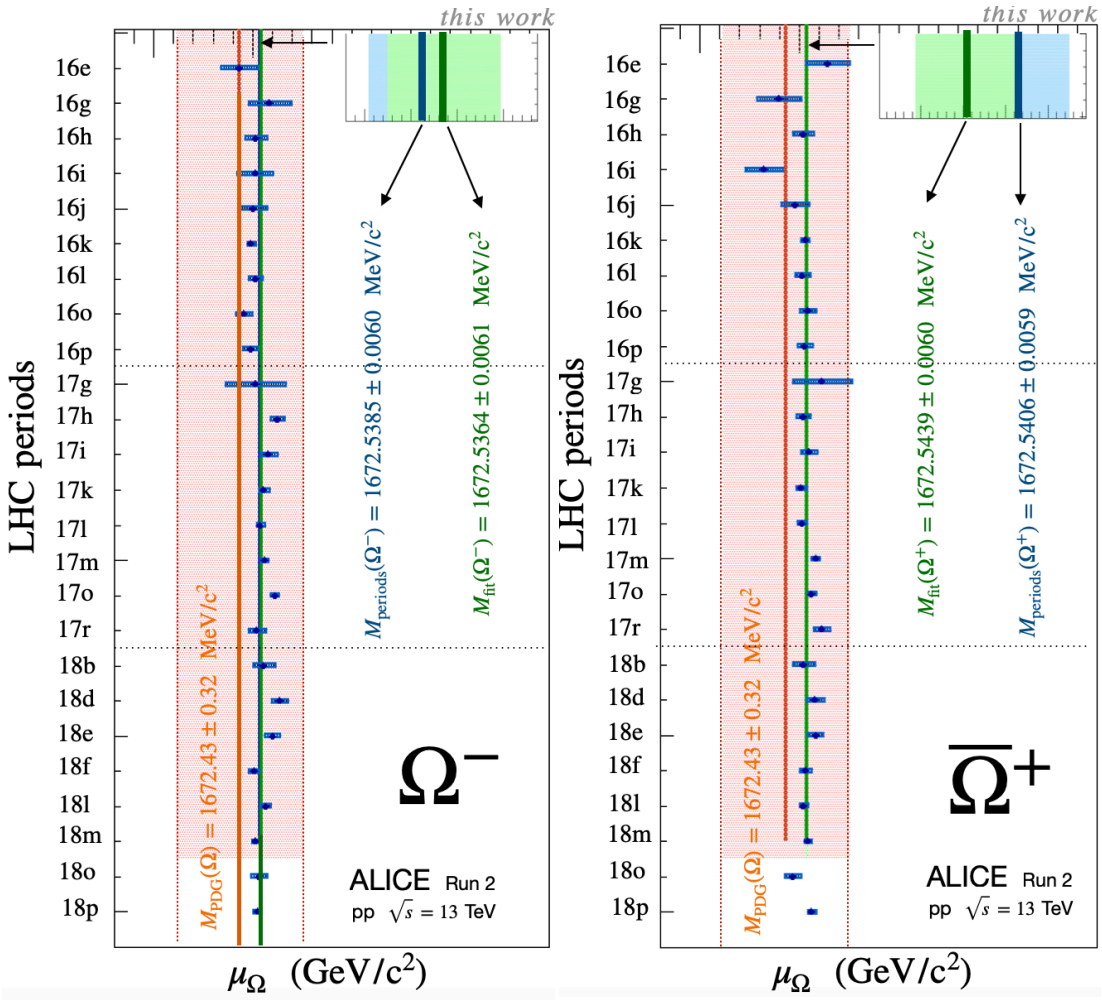

(a) Analysis with the Ω^--sample.

(b) Analysis with the $\overline{\Omega}^+$-sample.

Figure 7.1: Plateau analysis for each data sample collected for each data taking period.

7.2 Variation of track and topology selection

In our analysis we set the values of the topological variables to the central values. However, there is no unique recipe how to make the best choice of these cantral values. Variations of the cut values on topological variables is therefore possible. In this section we estimate the systematic uncertainty related to the topological variations. We proceed as follows. A cut variation means that we change the threshold values of a given topological variable within a specified value range using equidistant steps in a random manner (flat distribution), see Table 7.1. The tightest cut values were chosen in a way that when applied together there is a 25% drop in clean $\Omega^{\pm}$ signal in the plateau region $p_T > 2$ GeV/c.

Variable	Central	Interval	Step
DCA meson to PV (cm) >	0.20	$[\,0.05 - 0.20\,]$	0.05
DCA baryon to PV (cm) >	0.10	$[\,0.05 - 0.15\,]$	0.05
DCA bachelor to PV (cm) >	0.05	$[\,0.04 - 0.12\,]$	0.04
DCA V0 to PV (cm) >	0.04	$[\,0.02 - 0.06\,]$	0.02
DCA bachelor to V0 (cm) <	1.0	$[\,0.4 - 1\,]$	0.2
DCA negative to positive (cm) <	1.0σ	$[\,0.6 - 1.4\,]\,\sigma$	0.4σ
$\mathrm{Cos(PA}_{\Lambda})$ >	0.95	$[\,0.98 - 0.99\,]$	0.01
$\mathrm{Cos(PA}_{\Omega})$ >	0.99	$[\,0.98 - 0.995\,]$	0.005
R_{Λ} (cm) >	0.6	$[\,0.6 - 1.4\,]$	0.4
R_{Ω} (cm) >	1.1	$[\,0.6 - 1.2\,]$	0.6
$c\tau^{\mathrm{exp}}/c\tau\vert_{\Lambda}$ <	4	$[\,1 - 3\,]$	1
$c\tau^{\mathrm{exp}}/c\tau\vert_{\Omega}$ <	3	$[\,1.5 - 3.5\,]$	0.5

Table 7.1: Values of topological cuts used for the analysis (central) and for the topological variations. The latter are shown in the right two columns. Variables are varied within a given value range in equidistant steps. Each value is chosen randomly (flat distribution). The units of variables in each row are shown in the left column.

For each set of varied cut values we determine the mean mass values of $\Omega^{\pm}$ particles using the same properties of bins and fitting procedure. It is clear that any two data sub-samples on which we reconstruct the Ω mass are dependent. Rigorously, the proper superset T is that sample with the loosest cuts. However, since the value ranges are generally tight we can assume for each sub-sample S that $S \cap T \approx T$. Therefore, we decided to compare results obtained in each measurement on a varied sample with the measured mass values determined with the Ω sample on which the central cut values were applied.

A complete set of variations with all values given in Table 7.1 would result in performing the plateau analysis $\sim 10^6$ times. For the reasons of CPU limits, we decided to make an estimate of the systematic uncertainty on a much smaller sample of 3000 variations. We

computed the mean mass deviation $\langle \Delta\mu \rangle \pm \sigma_{\langle \Delta\mu \rangle}$ according to the prescription given in the introductory part of this chapter. The average systematic uncertainty σ_Ω is determined as the mean of the $\sigma_{\langle \Delta\mu \rangle}$ distribution. If any obtained result was consistent with that evaluated with the central cuts, $\sigma_{\langle \Delta\mu \rangle} = 0$, then this result was not used for the estimation of the systematic uncertainty. First of all, we performed the analysis on the Ω^- sample and recorded the values of topological variables in each variation. Then the Ω^+ analysis was done using the recorded set of the cut values. The results are depicted in Fig. 7.2.

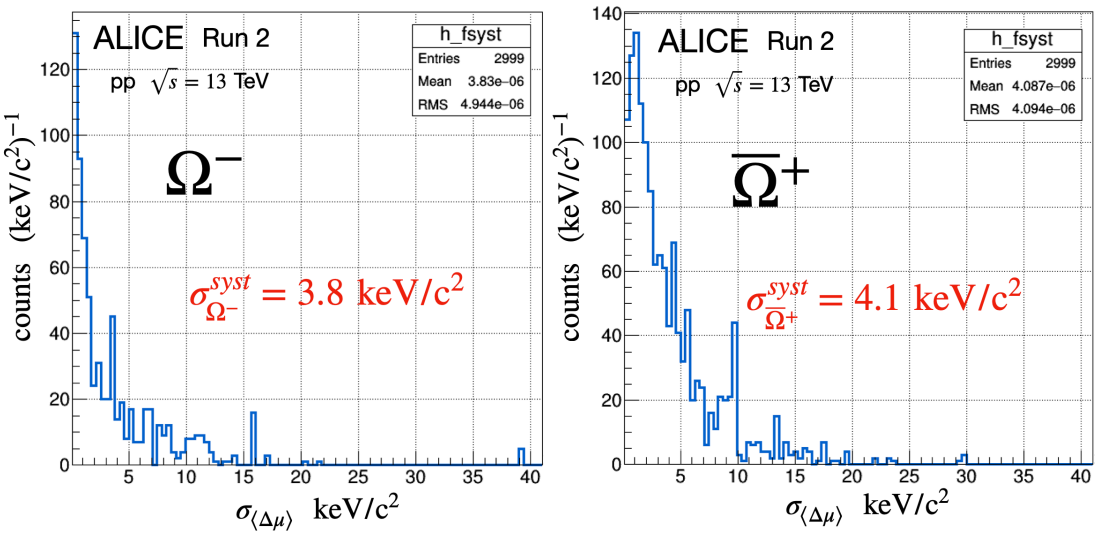

(a) Analysis with the Ω^--sample.

(b) Analysis with the $\overline{\Omega}^+$-sample.

Figure 7.2: Distribution of systematic uncertainty $\sigma_{\langle \Delta\mu \rangle}$ obtained in the mass analysis of the Ω hyperons obtained on different data sub-samples using the variation of topological cuts.

For the final result, we conclude that the mean systematic uncertainty due to topological cut variations is $\sigma^{syst}_{\Omega^-} = 3.8 keV/c^2$ and $\sigma^{syst}_{\overline{\Omega}^+} = 4.1 keV/c^2$

7.3 Λ MASS DEPENDENCE

For the calculation of the invariant mass of the $\Omega^{\pm}$ candidates, we use the central mass of the Λ baryon in Eq. 5.10. However, one could also determine the mass of the baryons using the kinematic information about each charged daughter track. For the Ω baryons the formula is:

$$M_{\text{inv}}(p\pi K) = \left((E_p + E_\pi + E_K)^2 - p_\Omega^2\right)^{\frac{1}{2}} \tag{7.6}$$

The method to determine the invariant mass with the equation above is connected to the values of the invariant mass of the Λ baryon and thus is more sensitive to the track reconstruction effects, i.e. energy scaling etc., than the method employing Eq. 5.10.

Figure 7.3 depicts the mean mass distribution the Ω particles as a function of transverse momentum comparing the invariant mass $M_{\text{inv}}(\Omega)$ and $M_{\text{inv}}(p\pi K)$. For visibility, we analysed the combined $\Omega^- + \overline{\Omega}^+$ sample. The invariant mass fit in the plateau region $p_T \in [2, 6]$ GeV/c yields the value $\overline{M}_{\text{inv}}(p\pi K)$ which deviates from the central result of this analysis by around 56 ± 7 keV/c^2, see chapter 6. Although this deviation is significant, we cannot compute the systematic uncertainty according to Eq. 7.3 and 7.5.

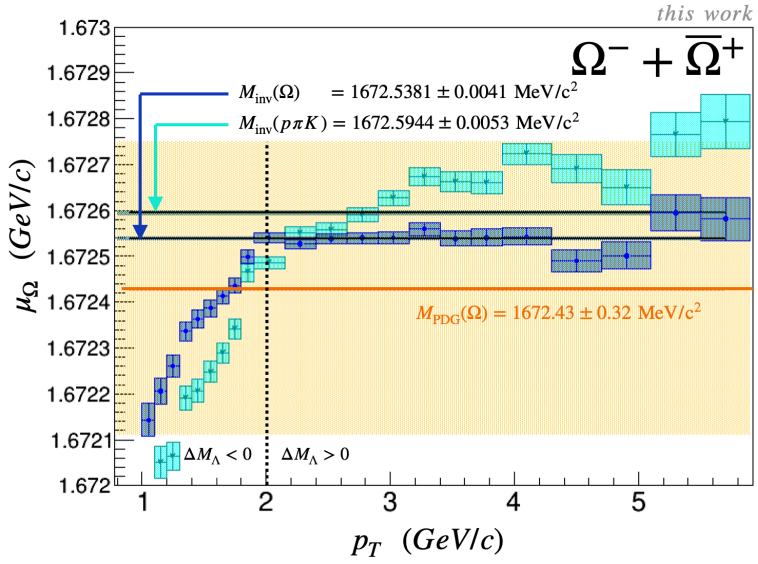

Figure 7.3: Invariant mean mass spectra of the Ω baryons as a function of p_T. Two different methods were used for the mass computation. The dark blue squares represent the Ω mass values which were calculated using the world average mass value of the Λ baryon. The light blue squares denote the reconstructed Ω mass.

We note that two methods for the mass determination differ in their sensibility on the value of the Λ mass. This can be seen as follows. Let the deviation (in this work: the positive

mass offset) of the measured Λ mass $M_{\text{inv}}(\Lambda)$ and the world average mass M_Λ be $\Delta M_\Lambda = M_{\text{inv}}(\Lambda) - M_\Lambda$; let the world average mass of the Ω baryons be M_Ω; let the Ω mass determined by Eq. 5.10 and Eq. 7.6 be $M_{\text{inv}}(\Omega)$ and $M_{\text{inv}}(p\pi K)$, respectively. Then there is a connection between the values expressed by:

$$M_{\text{inv}}(p\pi K) = M_{\text{inv}}(\Omega) + \Delta M_\Lambda \cdot \frac{M_\Lambda}{M_\Omega} + \zeta, \tag{7.7}$$

where the term ζ depends on the momenta of the daughter particles. For the exact derivation, see appendix D. In particular, the formula above implies that $M_{\text{inv}}(p\pi K) < M_{\text{inv}}(\Omega)$ for $p_T < 2$ GeV/c as the mass shift ΔM_Λ is negative in that momentum range, see Fig. 6.8 and 7.3; and analogously, one expects that $M_{\text{inv}}(p\pi K) > M_{\text{inv}}(\Omega)$ for $p_T > 2$ GeV/c.

In order to compare both mass evaluation methods quantitatively, we correct the $M_{\text{inv}}(p\pi K)$ distribution for the shift ΔM_Λ. To do this, we fit the invariant Λ mass spectrum in p_T bins. For each bin i we determine the shift term $\Delta M_\Lambda(i\text{ bin})$. For the Ω analysis we choose the same properties of the bins as for the Λ analysis.

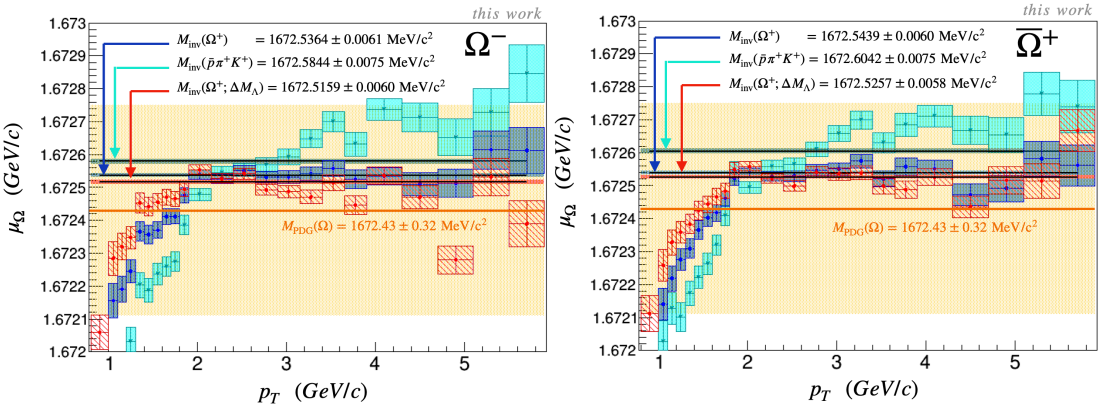

(a) Invariant mass of the Ω^- hyperons.

(b) Invariant mass of the $\overline{\Omega}^+$ hyperons.

Figure 7.4: Systematic studies of the Ω mass spectrum.

We calculate the invariant mass values according to Eq. 7.6, consequently fit the invariant mass spectrum of the Ω baryons and finally subtract the terms $\Delta M_\Lambda \cdot M_\Lambda / M_\Omega$ binwise. The values $\Delta M_\Lambda = \mu_{i,\Lambda} - M_{\text{PDG}}(\Lambda)$ are calculated for each p_T bin i where $\mu_{i,\Lambda}$ is the mean value of the fit Λ mass distribution. For the invariant mass spectra of the Ω^- and $\overline{\Omega}^+$ candidates we differentiate between the mass distributions of the Λ and $\bar{\Lambda}$ particles, respectively. The corrected spectrum is compared to the $M_{inv}(\Omega)$ distribution: the plateau analysis in $p_T \in [2, 6]$ GeV/c is performed and the obtained fit values are quantitatively compared.

Figure 7.4 illustrates our results. The difference in the mean mass values between $M_{\text{inv}}(\Omega)$ distribution and the corrected mass spectrum $M_{\text{inv}}^{\text{corr}}(\Omega)$ are $\Delta M(\Omega^-) = 20.5 \pm 8.6\ \text{keV/c}^2$ and $\Delta M(\overline{\Omega}^+) = 18.2 \pm 8.3\ \text{keV/c}^2$. The variance of the mass difference is computed as the quadratic sums of the individual uncertainties. Both values $\Delta M(\Omega^-)$ and $\Delta M(\overline{\Omega}^+)$ are consistent within 3σ intervals and are considered to be non-significant. Hence we conclude that two methods for the Ω mass estimation are consistent with each other up to the systematic bias which manifests itself in the offset of the Λ mass.

It has been shown in this analysis that both the Λ and the Ω baryon have a systematic mass offset. The determined $\Omega^{\pm}$ mass values lie within the total uncertainty of the world average Ω mass, and hence it is not sufficient to extrapolate the value of the shift $\Delta M^{\text{offset}}(\Omega)$ just from the Ω mass values. We rely more on the measurement with the Λ particle, whose reconstructed mean mass value deviates significantly from the world average Λ mass. Since the mass offsets of the Λ and Ω particles are connected through Eq.7.7, we evaluate the value $\Delta M^{\text{offset}}(\Omega)$ as:

$$\Delta M^{\text{offset}}(\Omega) = \Delta M^{\text{offset}}(\Lambda) \cdot \frac{M_\Lambda}{M_\Omega} \tag{7.8}$$

With $\Delta M^{\text{offset}}(\Lambda) = 157 \pm (6 \oplus 8)\ \text{keV/c}^2$ and $\Delta M^{\text{offset}}(\bar{\Lambda}) = 136 \pm (6 \oplus 8)\ \text{keV/c}^2$, we obtain using the equation above:

$$\Delta M^{\text{offset}}(\Omega^-) = 105 \pm 7\ \text{keV/c}^2 \tag{7.9}$$

$$\Delta M^{\text{offset}}(\overline{\Omega}^+) = 91 \pm 7\ \text{keV/c}^2 \tag{7.10}$$

Both values above are consistent within the total uncertainty. We estimate the mean mass offset for the $\Omega^{\pm}$ particles to be $\Delta M^{\text{offset}}(\Omega) = 98 \pm 7\ \text{keV/c}^2$.

7.4 Magnetic field

For each period we recorded the magnitude and the polaraity of applied magnetic field. This allows us to perform a systematic check based on magnetic field effects. Our complete data sample can be split in three subgroups of periods, see table 7.2.

For the period LHC17*g* where the magnetic field $B = -0.2$ T was applied we do not have enough statistics to perform a consistent systematic check with the precision of $\sim 1 - 10$ keV/c^2 when analysing the Ω sample. Consequently, we cannot make any statement about the impact of the magnetic field on the reconstructed Ω mass. Therefore, we decided to perform a systematic check of the properties of the $\Omega^{\pm}$ signal in dependence on the B-field polarity.

B [T]	Periods	S(Ω^-)($p_T > 2$ GeV/c)	S($\bar{\Omega}^+$)($p_T > 2$ GeV/c)
+ 0.5	LHC16(h,j,k,l,o,p) LHC17(f,j) LHC18(g,i,m,n,o,p)	45120(220)	46720(220)
– 0.5	LHC16(d,e,g) LHC17(c,e,h,i,k,l,m,o,r) LHC18(b,d,e,f,h,j,k,l)	51840(230)	53290(230)
– 0.2	LHC17g	436(21)	466(22)

Table 7.2: Data sub-samples split to account for the magnetic field.

B [T]	$M_{\text{fit}}(\Omega^-)$ [MeV/c^2] [MeV/c^2]	$M_{\text{fit}}(\bar{\Omega}^+)$ [MeV/c^2]
+ 0.5	1672.316(90)	1672.5104(90)
– 0.5	1672.441(80)	1672.5696(79)
– 0.2	1672.61(15)	1672.51(15)

Table 7.3: Results obtained in the analysis of the energy rescaled Ω sample invariant mass dependence on the polarity of the magnetic field.

For each of the sub-samples we extrapolate the mean invariant mass and its statistical uncertainty in the plateau analysis. Since each data sub-sample ($B = +0.5$ T and $B = -0.5$ T) is around a half of the total sample ($B = \pm 0.5$ T and $B = -0.2$ T combined), we double the size of p_T-bin width, i.e. each bin is 200 MeV/c wide. Thus we try to keep the same order of the statistical fluctuations in each p_T bin. The results obtained for the energy rescaled sample are shown in table 7.5. In case of the Ω^- baryons the deviation between mass values is $\Delta M(\Omega^-) = \overline{M}(\text{B} = -0.5\text{ T}) - \overline{M}(\text{B} = +0.5\text{ T}) = 13 \pm 12$ keV/c^2, where the uncertainty

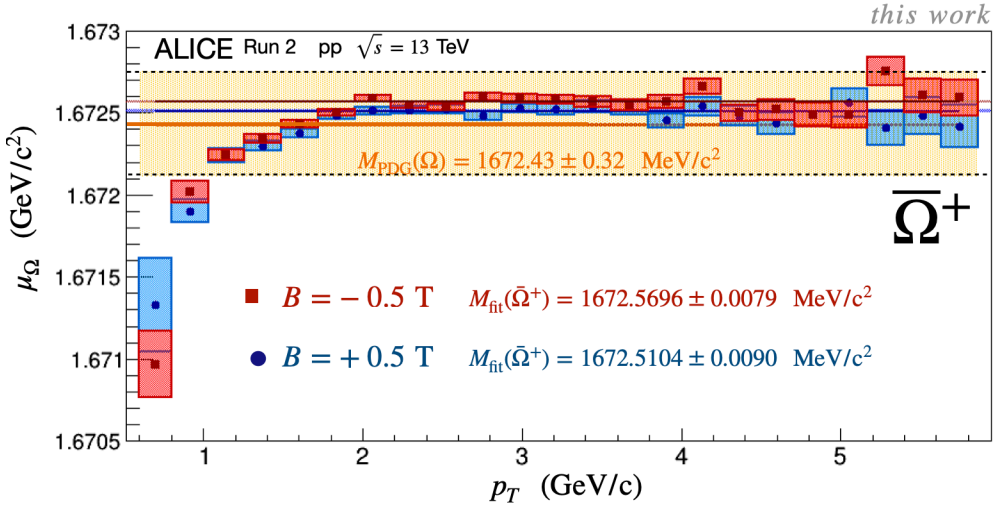

Figure 7.5: Mean mass spectrum of the $\overline{\Omega}^+$ particle as a function of the momentum p_T, plotted for two different magnetic field polarities.

$\sigma^2_{\Delta M} = \sigma^2_{\mathrm{B=-0.5T}} + \sigma^2_{\mathrm{B=+0.5T}}$ because the samples are independent from each other. In case of the $\overline{\Omega}^+$ hyperons, the analogous calculation of the deviation results in $\Delta M(\bar{\Omega}^+) = 60 \pm 12$ keV/c^2 which is significant. Furthermore, the Ω^+ measured mean mass values do not overlap within the 3σ uncertainty range, i.e. the values are discrepant. Figure 7.5 illustrates the mean mass spectrum of the Ω^+ baryon for two polarities of the magnetic field.

A possible dependence of the energy loss correction on the secondary tracks, which we performed in the analysis, on the magnetic field polarity is excluded since also for initial (not corrected) sample the deviations for the Ω^- and $\bar{\Omega}^+$ baryons are $\Delta M_{\mathrm{initial}}(\Omega^-) = 9 \pm 12$ keV/c^2 and $\Delta M_{\mathrm{initial}}(\bar{\Omega}^+) = 58 \pm 12$ keV/c^2, respectively. This result was tested to be independent on the choice of the bin width, signal extraction region or the choice of the plateau region. We calculate the systematic uncertainty due to the polarity of the magnetic field σ_B only for the $\bar{\Omega}^+$ candidates. We calculate the value σ_B according to Eq.7.3:

$$\sigma_B(\overline{\Omega}^+) = (M_{B=-0.5\mathrm{T}} - 3 \cdot \sigma_{B=-0.5\mathrm{T}})|_{\overline{\Omega}^+} - (M_{B=+0.5\mathrm{T}} + 3 \cdot \sigma_{B=+0.5\mathrm{T}})|_{\overline{\Omega}^+} = 8.8\ \mathrm{keV/c^2} \tag{7.11}$$

7.5 TPC related systematic studies

7.5.1 TPC counting gas

The choice of the counting gas inside the TPC active volume may have an impact on the tracking reconstruction efficiency. During Run 2 two gas compositions were used, see table 7.4. In this section we perform the systematic check based on the choice of the gas composition. We subdivided the total collected sample into two sub-samples, performed the mean mass analysis for each of the samples using the bin width of 200 MeV/c^2 in the whole $p_T \in [2, 6]$ GeV/c and finally compared the results.

TPC gas composition	Periods	S(Ω^-)($p_T > 2$ GeV/c)	S($\bar{\Omega}^+$)($p_T > 2$ GeV/c)
Ar-CO_2 ($88\% - 12\%$)	LHC 16, 18	71990(270)	74100(270)
Ne-CO_2-N_2 (90 : 10 : 5)	LHC 17	36020(190)	36990(190)

Table 7.4: Data sub-samples split to account for the TPC counting gas composition.

TPC gas composition	$M_{\text{fit}}(\Omega^-)$ [MeV/c^2] [MeV/c^2]	$M_{\text{fit}}(\bar{\Omega}^+)$ [MeV/c^2]
Ar-CO_2 ($88\% - 12\%$)	1672.5283(83)	1672.5250(83)
Ne-CO_2-N_2 (90 : 10 : 5)	1672.5520(110)	1672.5717(107)

Table 7.5: Results obtained in the analysis of the energy corrected Ω sample invariant mass dependence on the TPC gas composition.

The deviation of the Ω^- mean mass values for the two gas compositions is found to be $\Delta M(\Omega^-)_{\text{TPC gas}} = \bar{M}(Ar) - \bar{M}(Ne) = 23 \pm 14$ keV/c^2. This deviation is insignificant. For the Ω^+ particles the similar calculation yields a significant deviation $\Delta M(\Omega^+)_{\text{TPC gas}} = 47 \pm 14$ keV/c^2. However, since the measured values overlap within the ranges of the 3σ uncertainties, they are considered to be consistent. Hence, no systematic uncertainty should be determined in this case.

7.5.2 Particle identification

We investigated how the PID quality of the TPC influence the measurement of the Ω mass. To do this, we varied the number of the standard deviations $\sigma_{dE/dx}$ from the expected dE/dx value for individual daughters while keeping other kinematic and topological cuts at the central values. In this case we deal with dependent data samples. The proper superset T is given by all daughters with $n_{\sigma(dE/dx)} < 4$.. This implies that each measurement obtained in each

variation (i.e. on the subset S) is compared to the proper superset T according to Eq.7.4. We vary the values of $n_{\sigma(dE/dx)}$ in the range $[2, 4]$ in equidistant steps $\Delta n_{\sigma(dE/dx)} = 0.2$. For each variation the mean mass deviation $\langle \Delta\mu \rangle$ is determined, see Fig. 7.6. One can infer from Fig. 7.6 that for cases with varied $n_{\sigma(dE/dx)}$ close to 4 the sets S and T do not differ substantially from each other, hence $\langle \Delta\mu \rangle$ is close to 0 as expected. For the cases when we select daughter sample with $n_{\sigma(dE/dx)} < 1-2$ the statistical uncertainty of the mean mass deviation becomes large. This can be explained by decreased statistics of the $\Omega^{\pm}$ mass-spectrum and hence - by larger statistical fluctuations in individual p_T-bins. The systematic uncertainty due to TPC PID is determined as the mean of the $\sigma_{\langle \Delta\mu \rangle}$ distribution, see Eq. 7.5. The total uncertainty $\sigma_{\Omega}(\text{TPC PID}) = \langle \sigma_{\text{meson}} \rangle \oplus \langle \sigma_{\text{baryon}} \rangle \oplus \langle \sigma_{\text{bachelor}} \rangle$. We evaluate $\sigma_{\Omega^-}(\text{TPC PID}) = 0.1 \oplus 0.1 \oplus 0.4\ \text{keV/c}^2 = 0.4\ \text{keV/c}^2$ and $\sigma_{\overline{\Omega}^+}(\text{TPC PID}) = 0.2 \oplus 0.2 \oplus 0.4\ \text{keV/c}^2 = 0.5\ \text{keV/c}^2$. We keep the values for the record.

7.5.3 Number of clusters

A track of a charged particle may have up to 159 reconstructed clusters inside the TPC. Tracks with higher number of the TPC clusters have higher overall position and momentum resolution, i.e. they are of high quality. It is tempting to investigate how the kinematic quality of the tracks influence the mass measurement. Here, similar to section 7.5.2, we vary the number of cluster and compare each mass measurement with that done on the proper superset T, where T consists out of tracks with $N_{cls} > 70$. The variation range lies between 70 and 120 clusters with an equidistant step of $\Delta N_{cls} = 1$. Figure 7.7 shows the result. The mean systematic uncertainty is calculated in the same manner as in section 7.5.2. We evaluate $\sigma_{\Omega^-}(N_{\text{cls}}) = 0.2\ \text{keV/c}^2$ and $\sigma_{\overline{\Omega}^+}(N_{\text{cls}}) = 1.0\ \text{keV/c}^2$.

We also investigated another variable which controls the reconstruction quality of the tracks, i.e. the ratio of the number of reconstructed clusters to the number of findable clusters. When this ratio is close to unity then the quality of track is the best. However, it was shown that at ratios higher than 90% the data no longer agree with MC. For this reason, we vary the values of the ratio $N_{\text{cls}}/\ N_{\text{findable}}$ in the range $[0.7, 0.9]$ with a step of 1%. The nominal set is that with $N_{\text{cls}}/\ N_{\text{findable}} > 0.7$ and every measurement is compared to it, see Fig. 7.8. The systematic uncertainties are determined estimated to be $\sigma_{\Omega^-}(N_{\text{cls}}/N_{\text{findable}}) < 0.1\ \text{keV/c}^2$ and $\sigma_{\overline{\Omega}^+}(N_{\text{cls}}/N_{\text{findable}}) = 0.4\ \text{keV/c}^2$.

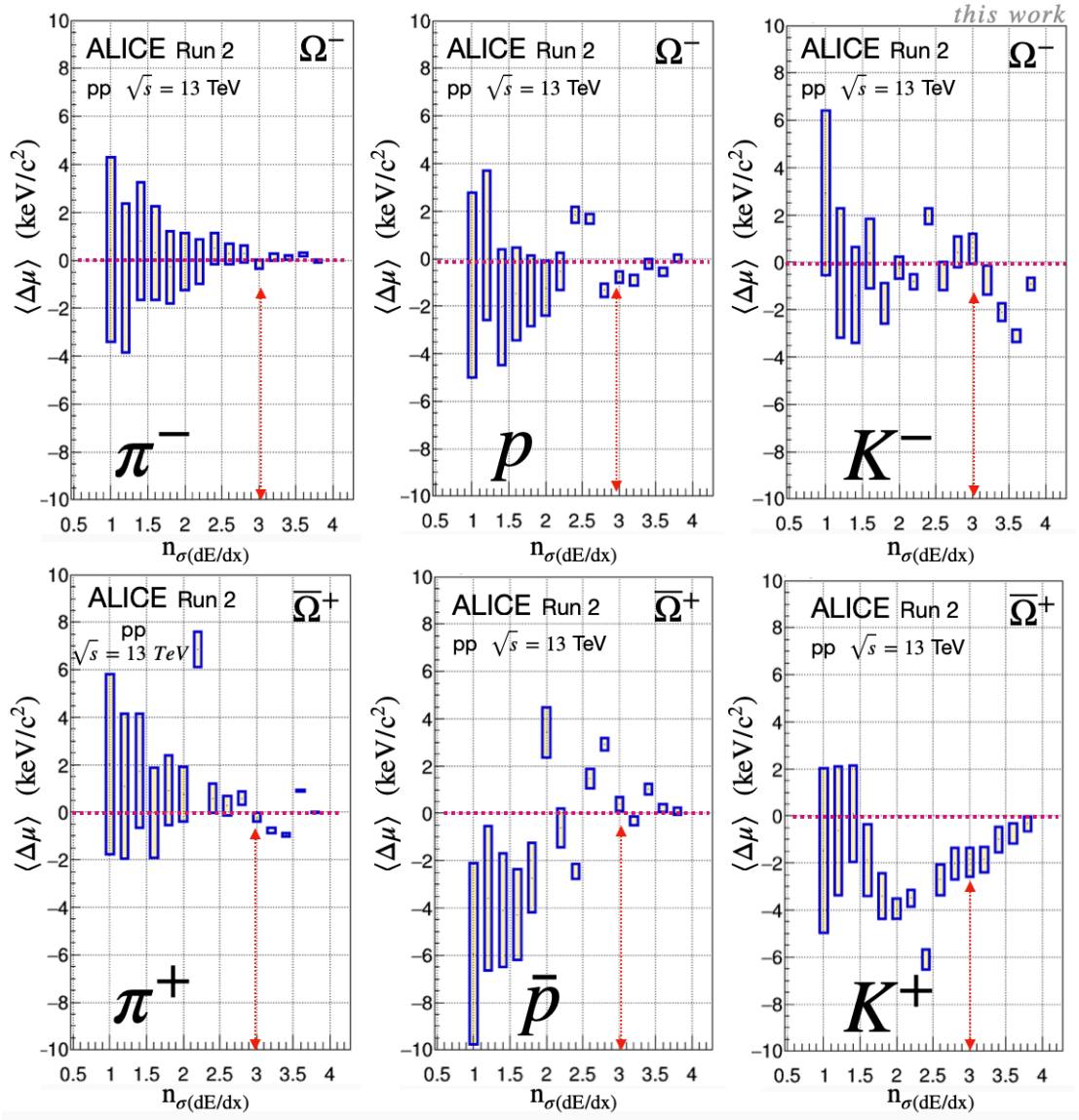

Figure 7.6: Systematic studies of the Ω invariant mass dependence on the quality of the PID with the TPC. The red arrow indicate the central cut value used for the analysis. Every measurement is compared to the proper superset with $n_{\sigma(dE/dx} < 4$.

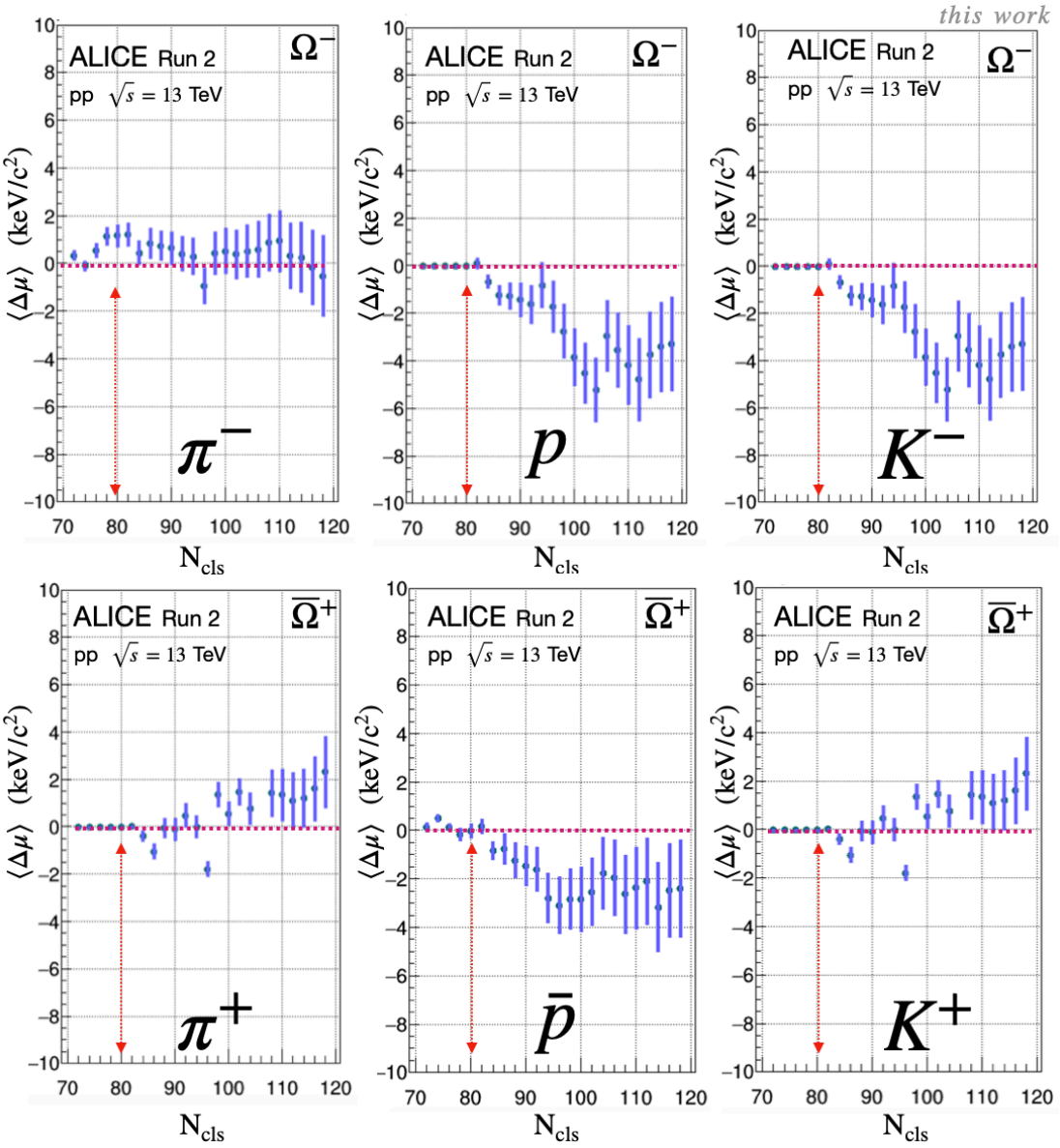

Figure 7.7: Systematic studies of the Ω invariant mass dependence on the threshold number of reconstructed track clusters inside the TPC $N_{\rm cls}$. The red arrow indicate the cut value put on the allowed number of TPC clusters used in the analysis. Each measurement is compared to that with $N_{\rm cls} > 70$.

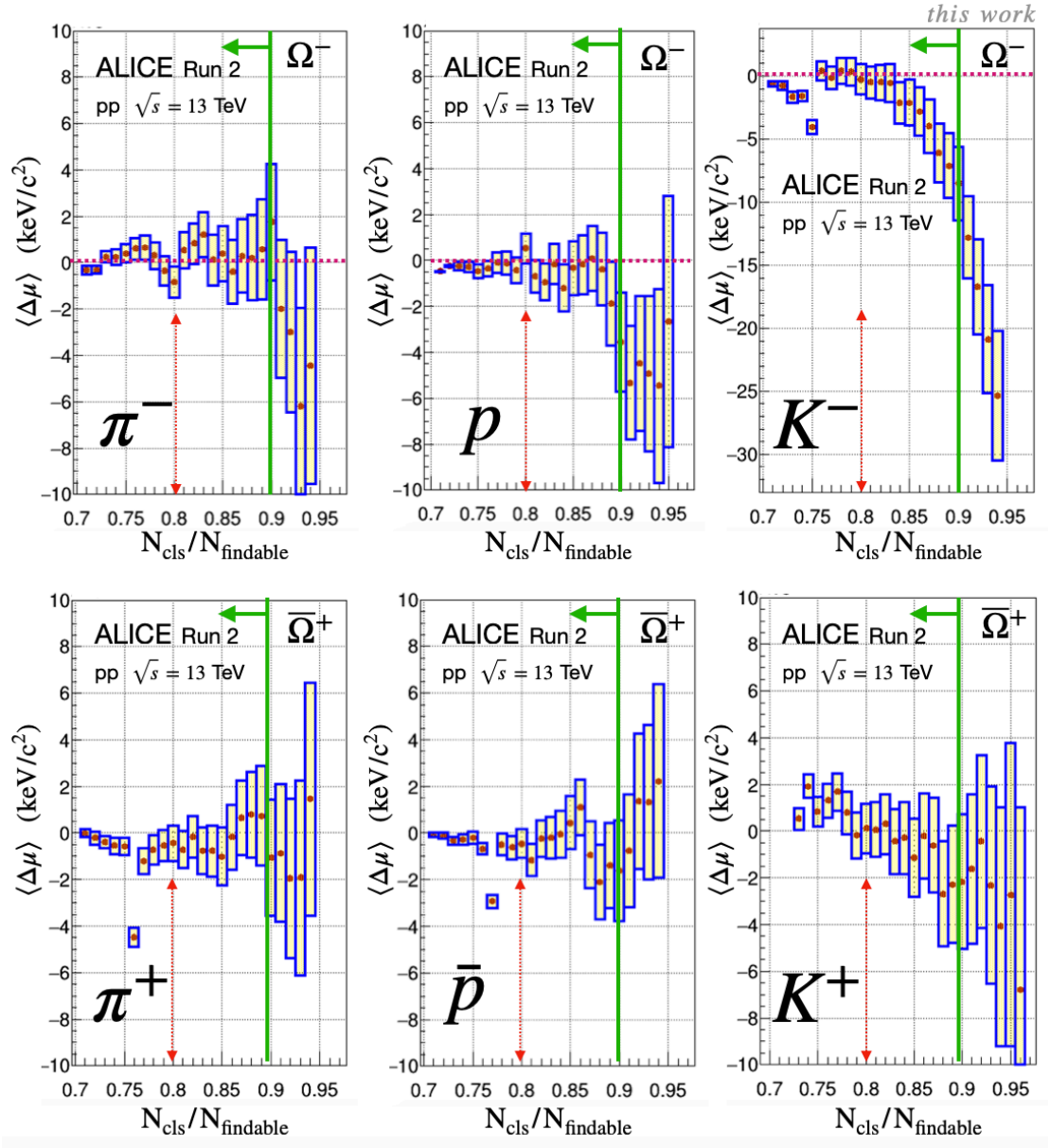

Figure 7.8: Systematic studies of the Ω invariant mass dependence on the threshold ratio of the number of reconstructed track clusters to the number of findable clusters $N_{\text{cls}}/N_{\text{findable}}$. Red arrow indicate the minimum allowed value of $N_{\text{cls}}/N_{\text{findable}}$ which was used in the analysis. Each measurement is compared to that with $N_{\text{cls}}/N_{\text{findable}} > 70$. The green vertical line at $N_{\text{cls}}/N_{\text{findable}} = 90$ shows where the discrepance between real data and MC becomes significant. See text for more detail.

7.5.4 Cascade rejection

We reject the $\Xi^{\pm} \rightarrow \Lambda + \pi^{\pm}$ events from our $\Omega^{\pm} \rightarrow \Lambda + K^{\pm}$ sample to keep it clean from misidentified π/K particles. The presence of the $\Xi^{\pm}$ candidates in the Ω contributes a large part to the background distribution in the Ω invariant mass spectrum, see Fig. 6.1b. Therefore, we dedicate this section entirely to the cascade rejection.

The cascades $\Xi^{\pm}$ are rejected in this work by accepting only those Ξ-hypothesis mass values $M_{\text{inv}}(\Xi)$ which lie outside of a given mass window $\text{M}^{\Xi}_{\text{window}}$ away from the world average mass value $M_{\Xi} = 1.321$ GeV/c^2, i.e. accept an event if $|M_{\text{inv}}(\Xi) - M_{\Xi}| > \text{M}^{\Xi}_{\text{window}}$. Table 7.6 summarizes how the width of the mass window $\text{M}^{\Xi}_{\text{window}}$ affects the $\Omega^{\pm}$ baryon yields, including the central cut used in the analysis $\text{M}^{\Xi}_{\text{window}} = 8$ MeV/c^2.

$\text{M}^{\Xi}_{\text{window}}$ [MeV/c^2]	$\text{S}(\Omega^-)(p_T > 2$ GeV/c)	$\text{S}(\bar{\Omega}^+)(p_T > 2$ GeV/c)
0	104432	107829
2	104432	107829
4	104386	107771
6	103553	106705
8	102751	105909

Table 7.6: Signal yields of the $\Omega^{\pm}$ baryons for different mass window with of the Ξ mass used for the cascade rejection.

Table 7.6 shows the clean signal yields for the $\Omega^{\pm}$ events in dependence of the Ξ-mass window width. Even for the widest window (i.e. tightest cut) the clean signal loss is just $1 - 2\%$.

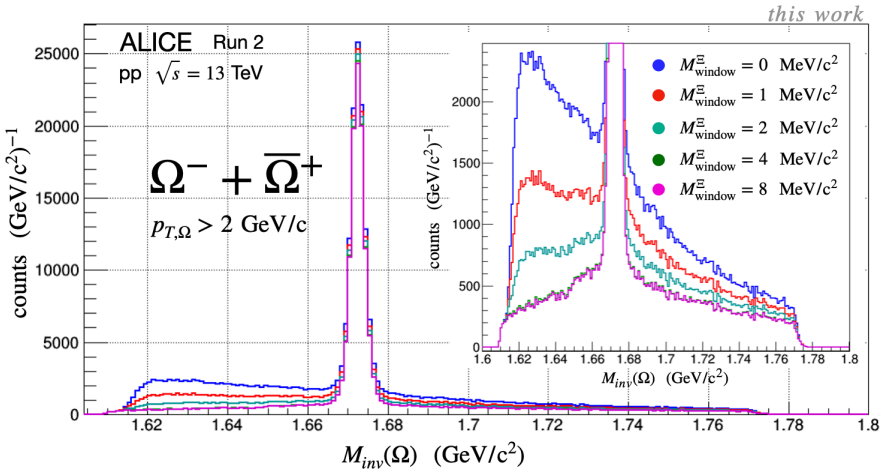

Figure 7.9: Invariant mass spectrum of the $\Omega^{\pm}$ hyperons for different cuts of the Ξ mass.

Although only a tiny fraction of the signal is lost after the cascade rejection, the admixture of the cascades in the sample changes the shape of the background under the Ω mass peak as is illustrated in Fig. 7.9. The change of the form of the background may shift the estimated fit mean mass value.

We evaluate the systematic uncertainty using the prescription for the dependent samples. The total set T is the sample which includes all cascades $M^{\Xi}_{\text{window}} = 0$. Every sample S after the application of the cut $M^{\Xi}_{\text{window}} > 0$ becomes an inclusion of T. The upper panels of Fig. 7.11 show the mean mass deviation $\langle \Delta\mu \rangle$ as a function of the Ξ mass window. For values of the mass window lying within the resolution ($1\sigma_{\Xi}$) of the Ξ mass spectrum, the background shape under the Ω peak does not change much and this yields consistent $M_{inv}(\Omega)$ values. As more cascades are being rejected, the more does the background shape influence the fit values $M_{inv}(\Omega)$. For $M^{\Xi}_{\text{window}} \geq 4$ MeV/c^2, the mean mass deviation becomes significant.

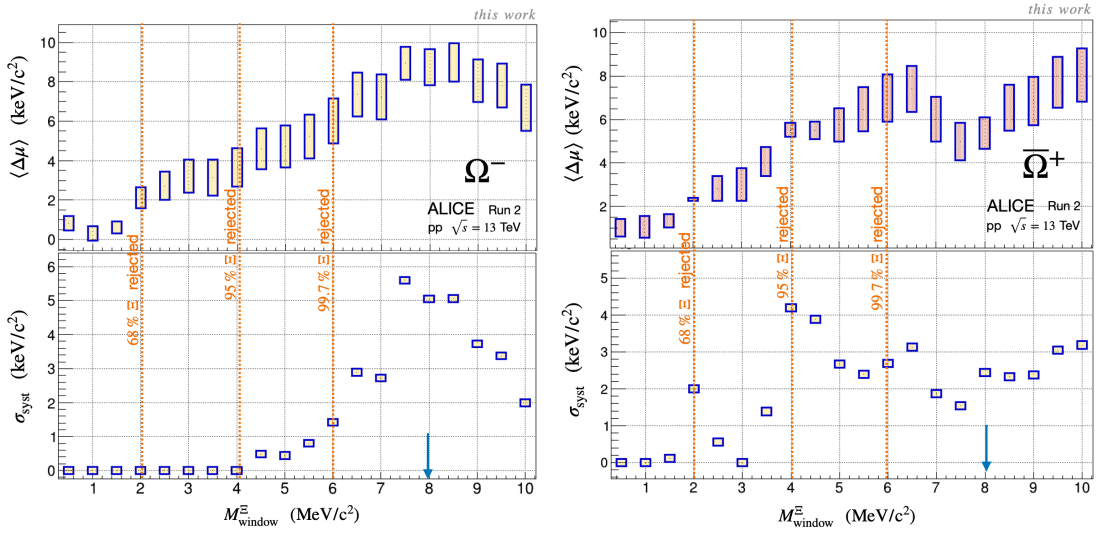

(a) Analysis with the Ω^--sample

(b) Analysis with the Ω^+-sample

Figure 7.10: Distribution of the mean mass deviations (upper panels) and the computed systematic uncertainty as a function of the width of the Ξ-mass rejection window.

The lower panels of Fig. 7.11 show the evaluated systematic uncertainties σ_{syst} according to Eq.7.5 for the $\Omega^{\pm}$ events as a function of the cascade mass window. Each determined value of σ_{syst} is coupled to the uncertainty of the fit. In order to decouple the fitting uncertainty from the uncertainty due to the cascade rejection, we determine the mean value $\langle \sigma_{\text{syst}} \rangle$ as evaluated from the set of 60 measurements in the range $M^{\Xi}_{\text{window}} \in [6, 12]$ MeV/c^2 with an equidistant mass window step $\Delta M^{\Xi}_{\text{window}} = 0.1$ MeV/c^2. In the given range we do not have any cascade candidates, and only insignificant amount of background is rejected. This implies that the

statistical spread of the values $\langle\sigma_{\text{syst}}\rangle$ is only due to uncertainty of the fit. The distributions of the systematic uncertainties $\langle\sigma_{\text{syst}}\rangle$ is illustrated in Fig.7.11.

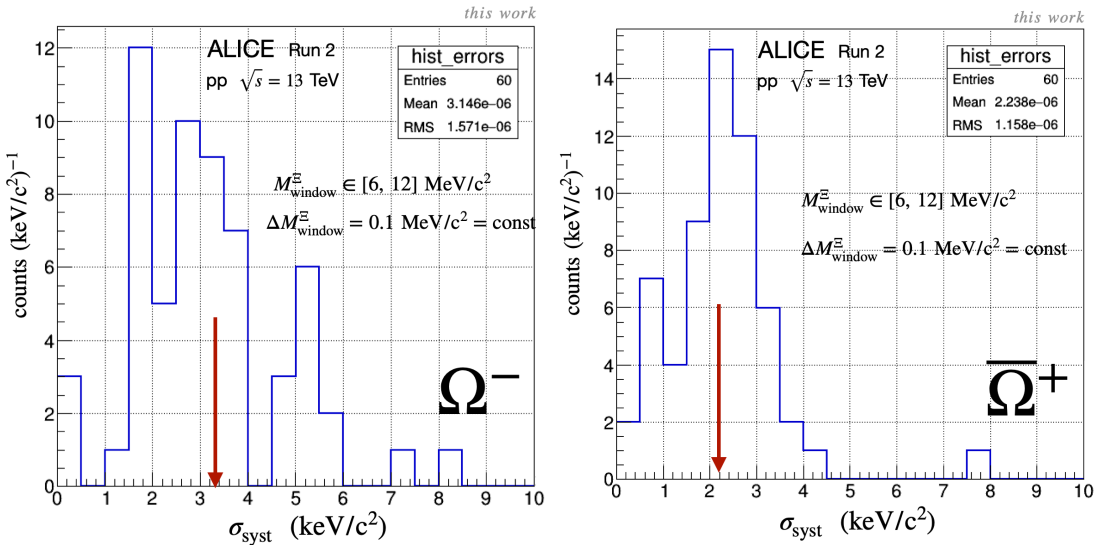

(a) Analysis with the Ω^--sample.

(b) Analysis with the Ω^+-sample.

Figure 7.11: Distribution of the systematic uncertainty due to cascade rejection.

Hence, we conclude that the systematic uncertainty due to the cascade rejection is 3.1 keV/c^2 and 2.2 keV/c^2 for the Ω^- and $\overline{\Omega}^+$ candidates, respectively.

7.5.5 Quality of energy scaling

In this section we test how good the dE/dx scaling of the momenta of the daughter particles, which we performed in the analysis, actually is. We found out that the largest correction was done on the protons (due to its large mass) and pion (due to low momentum) of the decay daughter decay $\Lambda \to p\pi$. Furthermore, we found out that the correction depends not only on the momentum itself but also on the radial distance of the secondary vertex from the primary vertex. That is why we analysed the Ω invariant mass spectrum in dependence of the radial decay position of the daughter Λ baryon R_Λ. We split our Ω candidate sample in two independent sub-samples: one contained only those Λ candidates that decay before the second SPD layer, i.e. $R_\Lambda \leq 7.9$ cm; for another sub-sample we demanded $R_\Lambda > 7.9$ cm. For a possible cross-check, we performed the analogous analysis on the sample for which no dE/dx rescaling on the secondaries was applied. The results of such analysis are shown in Table 7.7.

Sample	$M_{\text{inv}}(R_\Lambda \leq 7.9\text{ cm})$ [MeV/c^2]	$M_{\text{inv}}(R_\Lambda > 7.9\text{ cm})$ [MeV/c^2]
Ω^-, dE/dx rescaled	1672.5590(82)	1672.5011(93)
$\overline{\Omega}^+$, dE/dx rescaled	1672.5709(82)	1672.5053(90)
Ω^-, dE/dx NOT rescaled	1672.5775(82)	1672.5998(93)
$\overline{\Omega}^+$, dE/dx NOT rescaled	1672.5859(81)	1672.6069(91)

Table 7.7: Mean mass of the $\Omega^\pm$ candidates in dependence on the radial decay position of the daughter Λ baryon.

One can infer from the table above that the values $M_{\text{inv}}(R_\Lambda \leq 7.9$ cm) and $M_{\text{inv}}(R_\Lambda > 7.9$ cm) are consistent within the fit uncertainty in case of the not rescaled dE/dx sample for both the Ω^- and Ω^+ candidates. For the dE/dx scaled samples we see that the values are discrepant. This discrepancy could come from the daughter kaons, $\Omega \to \Lambda K$, whose energy was most of the times not rescaled especially if they originate from the Ω decay vertex close to the primary vertex. This significant Ω mass difference is not expected to come from the energy rescaling done on the daughter protons or pions alone since the invariant Λ mass is shown to be independent on the radial distance, see Fig. 6.4b.

In order to check if the dominant contribution comes from the daughter kaons, we split our total sample again in two independent sub-samples. However, this time the boundary is set by the radial distance of the Ω decay vertex $R_\Omega \leq 4$ cm and $R_\Omega > 4$ cm. The value $R_\Omega = 4$ cm is chosen in such a way that two sub-samples are in proportion $1:1$. Since the properties of the Ω^- and $\overline{\Omega}^+$ spectra are substantially the same, i.e. distribution of the decay

radius, and the dE/dx rescaling on the kaon directly depends on the value of R_Ω, we would expect the same mass differences for the Ω^- baryon and its anti-particle.

Sample	$M_{\text{inv}}(R_\Omega \leq 4\,\text{cm})$ [MeV/c^2]	$M_{\text{inv}}(R_\Omega > 4\,\text{cm})$ [MeV/c^2]
Ω^-, dE/dx rescaled	1672.5620(92)	1672.5116(83)
$\overline{\Omega}^+$, dE/dx rescaled	1672.5686(91)	1672.5189(81)

Table 7.8: Mean mass of the $\Omega^\pm$ candidates in dependence of the radial decay position of the mother Ω baryon.

The mass deviations are calculated to be $\Delta M(\Omega^-) = \Delta M(\overline{\Omega}^+) = M(R_\Omega < 4\text{cm}) - M(R_\Omega > 4\text{cm}) = 50 \pm 12$ keV/c^2. Consequently, the effect is indeed due to the energy rescaling of kaon tracks. We need to admit that there is a radius dependent mean mass shift in the Ω reconstructed mass spectrum. However, since the both Gaussian distributions with the mean and standard deviation given by the values in Table 7.8 overlap, we cannot estimate the systematic uncertainty in this case.

Consequently, we introduce an upper limit of 50 keV/c^2 on the estimated mean mass of the Ω baryon. We understand it as the non-vanishing mass shift due to energy scaling and handle the value as an asymmetric uncertainty.

8

Results and outlook

The goal of this thesis was to reconstruct the $\Omega^{\pm}$ hyperons in the golden decay channel $\Omega^- \rightarrow \Lambda(p\pi^-)K^-$ and $\overline{\Omega}^+ \rightarrow \Lambda(\bar{p}\pi^+)K^+$ and determine the invariant mass with unprecedented precision. We analysed the whole data sample of pp collisions at $\sqrt{s} = 13$ TeV which was collected during Run 2 in the years $2016 - 2018$. The invariant mass was measured in the momentum range of the Ω hyperons 2 GeV/c $< p_T <$ 6 GeV/c where the mean mass distribution is described by a plateau which we fit with a constant parameter. Our fit result for the sample of 101452 Ω^- and 104469 $\overline{\Omega}^+$ particles is $M_{\text{fit}}(\Omega^-) = 1672.5364 \pm (0.0061)_{\text{stat}}$ MeV/c^2 ($\chi^2_{\text{red}} = 1.03$) and $M_{\text{fit}}(\overline{\Omega}^+) = 1672.5439 \pm (0.0060)_{\text{stat}}$ MeV/c^2 ($\chi^2_{\text{red}} = 1.24$), respectively. The weighted average Ω mass is hence $M_{\text{fit}}(\Omega) = 1672.5402 \pm (0.0043)_{\text{stat}}$ MeV/c^2. The weights are given by the reciprokes of the statistical variances of individual values.

In this analysis we have shown that the hyperons artificially receive a positive offset to the mean invariant mass when the corresponding charged daughter particles are reconstructed with a primary track hypothesis. The latter means that the momentum of the particles was corrected for the specific energy loss dE/dx inside the ITS and beam pipe material. For the $\Lambda - \bar{\Lambda}$ and $\Omega^{\pm}$ baryons the mean mass shifts were estimated to be $+292 \pm 7$ keV/c^2 and

$+195 \pm 5$ keV/c^2 when compared to the world average Ω mass, respectively,.

We tried to correct for this effect by re-tracking the daughter particles with the correct assumption of their origin being the corresponding position of the secondary vertex. The re-tracking algorithm subtracted an amount of "fake" energy on a straight line segment connecting the spatial positions primary vertex and the secondary vertex, and rescaled the momenta of particles accordingly. Our correction did not make the mass offset vanish completely. Nevertheless, we managed to decrease its value by nearly a factor of two. For the $\Lambda - \bar{\Lambda}$ and $\Omega^{\pm}$ particles the values of the mass offset dropped to 147 ± 10 and 98 ± 7 keV/c^2, respectively.

Another goal of this thesis was to perform the CPT test in the Ω system. To do this, we needed to evaluate the total uncertainty of the corresponding mass measurement. Table 8.1 summarizes the values of both the statistical fit and systematic uncertainties of various kind.

Type	σ_{Ω^-} [keV/c^2]	$\sigma_{\overline{\Omega}^+}$ [keV/c^2]
Fit (statistical)	6.1	6.0
Magnetic field	0	8.8
Topological variations	3.8	4.1
Cascade rejection	3.1	2.2
TPC PID $n_{\sigma(dE/dx)}$	0.4	0.5
TPC N_{cls}	0.2	1.0
TPC $N_{cls}/N_{findable}$	0	0.4
dE/dx in the ITS and beam pipe	0	0
Total systematic	4.9	10.0
Total	7.8	11.7

Table 8.1: Summary of the statistical and systematic uncertainties of the $\Omega^{\pm}$ mass values.

In order to obtain the total variance we add individual values of uncertainty in quadrature. The mass shift due to the energy scaling of the charged daughter tracks builds the upper limit on the determined Ω mass and is included in the result as the asymmetric uncertainty $\delta M^{-}_{\text{offset}} = -50$ keV/c^2. Our result is

$$M_{\Omega^-} = 1672.5364^{+0}_{-0.0500} \pm (0.0061)_{\text{stat}} \pm (0.0049)_{\text{syst}} \text{ MeV/c}^2$$
$$M_{\overline{\Omega}^+} = 1672.5439^{+0}_{-0.0500} \pm (0.0060)_{\text{stat}} \pm (0.0100)_{\text{syst}} \text{ MeV/c}^2$$

The mass difference ΔM is therefore

$$\Delta M = M_{\Omega^-} - M_{\overline{\Omega}^+} = -7.5 \pm (8.6)_{\text{stat}} \pm (11.14)_{\text{syst}} \text{ keV/c}^2,$$

where individual uncertainties of the Ω^- and $\overline{\Omega}^+$ are added in quadrature and the common mass shift due to energy scaling cancels out. The CPT test is then performed

$$\frac{\Delta M}{M_{\text{fit}}(\Omega)} = (-4.48^{+1.13}_{-0} \pm (5.14)_{\text{stat}} \pm (6.66)_{\text{syst}}) \cdot 10^{-6}$$

where the positive part of the asymmetric uncertainty accounts for the mass offset of the mean value $M_{\text{fit}}(\Omega)$ which is given by $\delta M^{-}_{\text{offset}}$. Adding the statistical and systematic uncertainties in quadrature leads to the result

$$\left.\frac{\Delta M}{M(\Omega)}\right|_{\text{result}} = (-4.48^{+1.13}_{-0} \pm 8.41) \cdot 10^{-6}$$
$$\left.\frac{\Delta M}{M(\Omega)}\right|_{\text{PDG}} = (1.44 \pm 7.98) \cdot 10^{-5},$$

where $\frac{\Delta M}{M(\Omega)}|_{\text{PDG}}$ is the current world average of the CPT test and is given here for comparison. Our result is around one order of magnitude more precise than the recent world average. The improved value is still consistent with the CPT symmetry.

The momentum rescaling of the secondary particles which we have done in this work is the first measurement of this kind ever performed with ALICE. Further investigations and improvements are still needed to make the values of the mass offset in the hyperon sector become consistent with zero. Moreover, it is needed to be studied whether our energy re-scaling procedure is compatible with MC data. We note that importance of the energy rescaling may become apparent for the future precision measurements in upcoming Run 3 and Run 4. In Run 3, the upgrade of the TPC detector will enable a factor 100 more statistics to be collected since a new readout capability of around 3.5 kHz instead of 300 Hz in Pb-Pb collisions is expected (Lippmann, 2014). Furthermore, the upgrade of the ITS2 detector will increase the resolution of the secondary vertex reconstruction as the first detecting layer of the ITS2 is closer to the beam pipe than the current SPD1. For the particle tracking and energy scaling, a decrease of the material budget by a factor of seven will play a crucial role as this improves both the impact parameter and the momentum resolutions. (Abelev et al., 2014). Due to the lower material budget of the future ITS2 (and ITS3 in Run4, (Adamová et al., 2019)) it will be possible and of high interest not only to test CPT invariance in the Ω system in the currently unacceptable momentum range $p_T < 2$ GeV/c but also reconstruct the invariant mass with unprecedented precision and free of any systematic biases (such as mass offsets).

A

Discrete Symmetries

Operation of the discrete symmetries on different operators, also known as *inversions*, is summarised in the table below. The operators in bold denote the 3-vectors, s and Q have one component and x stands for 4-vector.

The matrices $S_{P,C,T}$ which act on spinor fields satisfy the following conditions:

$$S_P^{-1}\gamma^\mu S_P = \gamma_\mu \;\Rightarrow\; S_P = \gamma^0 \tag{A.1}$$

$$S_C^{-1}\gamma^\mu S_C = -(\gamma^\mu)^T \;\Rightarrow\; S_C = \gamma^2 \tag{A.2}$$

$$S_T^{-1}\gamma^\mu S_T = \gamma_\mu \;\Rightarrow\; S_T = i\gamma^1\gamma^3 \tag{A.3}$$

$$\tag{A.4}$$

Observable	Operator	P	C	T	CPT
spatial coordinate	$\mathbf{x}$	$-\mathbf{x}$	$\mathbf{x}$	$\mathbf{x}$	$-\mathbf{x}$
3-Momentum	$\mathbf{p}$	$-\mathbf{p}$	$\mathbf{p}$	$-\mathbf{p}$	$\mathbf{p}$
orbital angular momentum	$\mathbf{L} = \mathbf{x} \times \mathbf{p}$	$\mathbf{L}$	$\mathbf{L}$	$-\mathbf{L}$	$-\mathbf{L}$
projected component of spin	s	s	s	$-$s	$-$s
charge	Q	Q	$-$Q	Q	$-$Q
scalar field	$\varphi(t, \mathbf{x})$	$\eta_P \varphi(t, -\mathbf{x})$	$\eta_C \varphi^\dagger(t, \mathbf{x})$	$\eta_T \varphi(-t, \mathbf{x})$	$\eta_{CPT} \varphi^\dagger(-x)$
EM field	$A^\mu(t, \mathbf{x})$	$+A_\mu(t, -\mathbf{x})$	$-A^\mu(t, \mathbf{x})$	$+A_\mu(-t, \mathbf{x})$	$-A^\mu(-x)$
fermionic field, s = $\frac{1}{2}$	$\psi(t, \mathbf{x})$	$\eta_P S_P \psi(t, -\mathbf{x})$	$\eta_C S_C \bar{\psi}^T(t, \mathbf{x})$	$\eta_T S_T \psi(-t, \mathbf{x})$	$\eta_{CPT} \gamma_5 \gamma_0 \bar{\psi}^T(-x)$
general tensor	$T^{\mu\nu\rho\dots}(t, \mathbf{x})$	$\eta_P T_{\mu\nu\rho\dots}(t, -\mathbf{x})$	$\eta_C T^{\dagger(\mu\nu\rho\dots)}(t, \mathbf{x})$	$\eta_T T_{\mu\nu\rho\dots}(-t, \mathbf{x})$	$\eta_{CPT} T^{\dagger\mu\nu\rho\dots}(-x)$

Table A.1: Summary of action of discrete (inversion) symmetry operators: parity (P), charge conjugation (C), time-reversal (T) and its combination, CPT, on different observables.

B

Event properties

Period	N_{runs}	B [T]	Interaction rate [kHz]	TPC gas	Events selected [10^6]	Events analysis [10^6]
16d	10	-0.5	1.5 – 5.5		14.4	0.01
16e	11	-0.5	5 – 600		47.0	0.05
16g	17	-0.5	75 – 120		25.0	0.19
16h	67	+0.5	120 – 200 (∼130)		65.0	1.23
16j	34	+0.5	∼ 240	Ar - CO_2	41.8	0.90
16k	194	+0.5	∼ 120	88%-12%	139	4.51
16l	58	+0.5	∼ 120		27.7	1.38
16o	71	+0.5	∼ 120		30.8	1.11
16p	42	+0.5	120		19.2	1.19
17c	5	-0.5	1–45		8.63	0.007
17e	5	-0.5	5 – 200		9.45	0.01
17f	5	+0.5	4 – 22		9.05	0.01
17g	31	-0.2	4 – 70		88.4	0.14
17h	88	-0.5	100 – 200		112.2	2.21
17i	52	-0.5	190	Ne-CO_2-N_2	41.7	1.29
17j	10	+0.5	10 – 50	90%-10%-5%	36.9	0.03
17k	105	-0.5	190		87.7	3.70
17l	127	-0.5	190		65.6	4.82
17m	108	-0.5	190		92.3	4.87
17o	148	-0.5	190		94.0	6.26
17r	28	-0.5	50		23.5	1.48
18b	25	-0.5	2 – 80		168.6	0.22
18d	44	-0.5	195		37.1	1.63
18e	41	-0.5	195		37.3	1.51
18f	59	-0.5	195		50.0	4.06
18g	11	+0.5	20 – 160		7.55	0.04
18h	2	-0.5	195		3.42	0.30
18i	9	+0.5	20		49.7	0.05
18j	1	-0.5	190	Ar - CO_2	0.080	0.006
18k	12	-0.5	20 – 160	88%-12%	9.0	0.52
18l	76	-0.5	190		58.2	4.81
18m	242	+0.5	190 – 250		170.8	14.4
18n	2	+0.5	12		3.18	0.004
18o	39	+0.5	10 – 50,160 – 250		29.2	4.04
18p	79	+0.5	250		59.25	10.8

Table B.1: Periods' and event information

C

On covariance and correlation factors

Consider two samples S and T with a general condition $S \cap T = U$, where one can think of S, T and U as collections of cascade candidates in context of this work. [1]

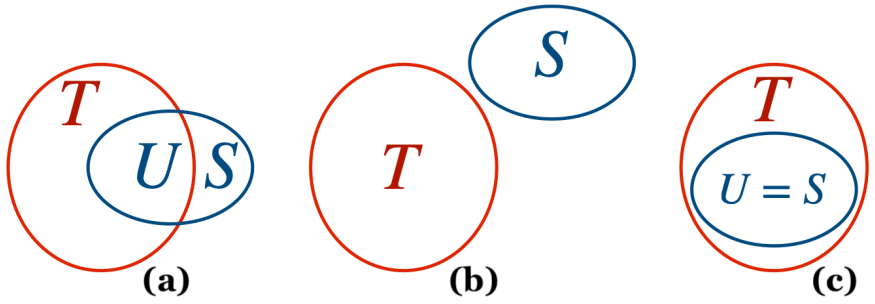

Figure C.1: (a) General subsets with a non vanishing intersection U. **(b)** Independent subsets. This can the case when studying sets dependent on different B field polarities, different TPC counting gas etc.**(c)** Case of inclusion. This case is studied by Barlow (2002).

Say, we measure some quantity $\mathbb{X}$ (mass, life-time etc.) on the sub-samples with averages

[1] Generally, if any daughter track is assigned to multiple cascade candidates, then one needs to consider the cascades are no longer independent. However, in this analysis we have on average one cascade pro event and hence, Ω candidates are viewed as independent events.

a:

$$a_S = \frac{1}{N_S}\sum_S x_S, \qquad a_T = \frac{1}{N_T}\sum_T x_T, \qquad a_U N_U = \sum_U x_U \tag{C.1}$$

and uncertainties of the mean $\bar{\sigma}$:

$$\bar{\sigma}_S^2 = \frac{\sigma_S^2}{N_S}, \qquad \bar{\sigma}_T^2 = \frac{\sigma_T^2}{N_T}, \qquad \bar{\sigma}_U^2 N_U = \sigma_U^2, \tag{C.2}$$

where σ^2 stands for the standard deviation. In the case of intersection sample U, we avoid using N_U in denominator, as N_U can be 0 in general. One can think of N_i as signal yields in a corresponding subsample i.

If one wants to compare the two measurements a_S and a_T with each other, a straightforward procedure is to calculate the difference $\Delta a = |a_S - a_T|$. According to propagation of errors, the uncertainty of Δa is given by:

$$\sigma_\Delta^2 = \bar{\sigma}_S^2 + \bar{\sigma}_T^2 - 2 \cdot cov(a_S, a_T), \tag{C.3}$$

where the covariance between *means* a_S and a_T defined as:

$$cov(a_S, a_T) = \frac{1}{n}\sum_{i=1}^{n} a_{i,T} \cdot a_{i,T} - \mu_S \mu_T, \tag{C.4}$$

where $\mu = \frac{1}{n}\sum a_i$. Here we consider that $N_S, N_T \gg 1$ and, therefore, assume that $a_{i,(S,T)} = a_{(S,T)} = \mu_{(S,T)}$ for $\forall i$. Generally, we cannot put the same assumption on U. Consequently, estimate of the mean a_U may have some deviation from μ_U, we may express it as $\delta\mu_U = a_U - \mu_U$. Here, a_U is the value obtained from a (any) single measurement.

One can decompose the sums as

$$N_S \cdot a_{i,S} = N_U \cdot a_{i,U} + (N_S \cdot a_{i,S} - N_U \cdot a_{i,U}) = \tag{C.5}$$

$$= N_U \cdot a_{i,U} + (N_S \cdot \mu_S - N_U \cdot a_U) \Rightarrow \tag{C.6}$$

$$a_{i,S} = \frac{N_U}{N_S} \cdot a_{i,U} + a_U - \frac{N_U}{N_S}\mu_S \tag{C.7}$$

and similarly, one obtains the same expression for the sample T:

$$a_{i,T} = \frac{N_U}{N_T} \cdot a_{i,U} + a_U - \frac{N_U}{N_T}\mu_T \tag{C.8}$$

Inserting results from C.7 and C.8 in C.4 leads to:

$$cov(a_S, a_T) = \frac{N_U}{N_S \cdot N_T}\sigma_U^2 + N_U \cdot \delta\mu_U \cdot \left[\frac{\mu_S}{N_S} + \frac{\mu_T}{N_T}\right] + \frac{N_U^2}{N_S \cdot N_T} \cdot (\delta\mu_U)^2 \tag{C.9}$$

In the equation above we used $\frac{1}{n}\sum a_{i,U}^2 = \bar{\sigma}_U^2 + \mu_U^2$. In case, when $N_U/N_{S,T} \ll 1$ (almost independent S and T, $S \cap T \approx \emptyset$), the covariance vanishes. If on contrary, $N_{U,S,T} \gg 1$, then $\delta\mu_U \to 0$ and the covariance reduces to $cov(a_S, a_T) = \frac{N_U}{N_S \cdot N_T}\sigma_U^2$. Moreover, if say, S is an inclusion of T, i.e. $S \subset T \Longleftrightarrow S \cap T = S$, then the covariance is given by a result obtained by Barlow (2002), i.e. $cov(a_S, a_T) = \frac{N_S}{N_S \cdot N_T}\sigma_S^2 = \frac{N_S}{N_T}\bar{\sigma}_S^2$. In summary, we may approximate σ_Δ as follows

$$\sigma_\Delta^2 = \begin{cases} \bar{\sigma}_S^2 + \bar{\sigma}_T^2 & , if \quad S \cap T = \emptyset \\ \bar{\sigma}_S^2 + (1 - 2 \cdot \frac{\sigma_S^2}{\sigma_T^2})\bar{\sigma}_T^2 & , if \quad S \cap T = S \end{cases} \tag{C.10}$$

In the latter case, one can approximate even further with $\sigma_\Delta^2 = \sigma_S^2 - \sigma_T^2$, when $\sigma_S \approx \sigma_T$, which for instance would be the case when width of the peak is given solely by detector resolution.

D

Λ mass dependence of the Ω mass spectrum

Here the derivation of equation 7.7 is presented.

For each cascade candidate we can consider the following. The invariant mass the Ω baryon $M_{\text{inv}}(p\pi K)$ calculated by Eq. 7.6 will have a shift from the world average central mass value $\Delta M_{p\pi K} = M_{\text{inv}}(p\pi K) - M_{\Omega}$. Analogously, the shift for the mass value $M_{\text{inv}}(\Omega)$ computed with Eq.5.10 will have a shift $\Delta M_{\Omega} = M_{\text{inv}}(\Omega) - M_{\Omega}$; and the Λ mass computed with Eq. 5.9 has a general shift $\Delta M_{\Lambda} = M_{\text{inv}}(\Lambda) - M_{\Lambda}$. When all mass shifts ΔM are small (which is the case in this analysis, $\Delta M/M \sim 10^{-5}$ we can approximate:

$$M_{\text{inv}}(p\pi K)^2 = (E_p + E_\pi + E_K)^2 - p_\Omega^2 \approx M_\Omega^2 + 2M_\Omega \cdot \Delta M_{p\pi K} \tag{D.1}$$

$$M_{\text{inv}}(\Omega)^2 = (E_\Lambda + E_K)^2 - p_\Omega^2 \approx M_\Omega^2 + 2M_\Omega \cdot \Delta M_\Omega \tag{D.2}$$

$$M_{\text{inv}}(\Lambda)^2 = (E_p + E_\pi)^2 - p_\Lambda^2 \approx M_\Lambda^2 + 2M_\Lambda \cdot \Delta M_\Lambda, \tag{D.3}$$

where $E_\Lambda = sqrt M_\Lambda^2 + p_\Lambda^2$. Subtracting Eq. D.3 from Eq. D.1 we get

$$\begin{aligned} M_{\text{inv}}(p\pi K)^2 - M_{\text{inv}}(\Omega)^2 &= 2M_\Omega(\Delta M_{p\pi K} - \Delta M_\Omega) \\ &= (E_\pi + E_p)^2 - E_\Lambda^2 + 2E_K(E_\pi + E_p - E_\Lambda) \\ &= M_{\text{inv}}(\Lambda)^2 - M_\Lambda^2 + 2E_K(E_\pi + E_p - E_\Lambda) \\ &= 2M_\Lambda \cdot \Delta M_\Lambda + 2E_K(E_\pi + E_p - E_\Lambda) \end{aligned}$$

or equivalently

$$\Delta M_{p\pi K} = \Delta M_\Omega + \Delta M_\Lambda \frac{M_\Lambda}{M_\Omega} + \zeta \tag{D.4}$$

The last term $\zeta = \frac{E_K(E_\pi + E_p - E_\Lambda)}{M_\Omega}$ vanishes for the Ω candidates in the limit of very high energy E_Ω. Hence, for the calculated masses we get (adding M_Ω to both sides of Eq.D.5)

$$M_{\text{inv}}(p\pi K) \approx \Delta M_{\text{inv}}(\Omega) + \Delta M_\Lambda \frac{M_\Lambda}{M_\Omega} \tag{D.5}$$

References

Aamodt, K. et al. (2010). Alignment of the ALICE inner tracking system with cosmic-ray tracks. *Journal of Instrumentation*, 5(3).

Abel, C. et al. (2020). Measurement of the Permanent Electric Dipole Moment of the Neutron. *Phys. Rev. Lett.*

Abelev, B. et al. (2014). Technical Design Report for the Upgrade of the ALICE Inner Tracking System. *J. Phys. G*, 41, 087002.

Ablikim, M. et al. (2019). Polarization and entanglement in baryon–antibaryon pair production in electron–positron annihilation. *Nat. Phys*.

Acharya, S., Adamova, D., Adler, A., Adolfsson, J., Aggarwal, M. M., Aglieri Rinella, G., & Agnello, M. (2020). *Production of light-flavor hadrons in pp collisions at* $\sqrt{s}$ *= 7 and* $\sqrt{s}$ *= 13 TeV*. Technical Report arXiv:2005.11120, CERN, Geneva.

Adam, J. et al. (2015). Precision measurement of the mass difference between light nuclei and anti-nuclei. *Nature Physics*, 11(10), 811–814.

Adamová, D. et al. (2019). A next-generation LHC heavy-ion experiment.

Aggarwal, M. M. et al. (2011). Strange and multistrange particle production in Au + Au collisions at $\sqrt{s_{NN}} = 62.4$ *GeV*. *Phys. Rev. C*, 83, 024901.

ALICE (2015). First results of the ALICE detector performance at 13 TeV.

ALICE (2020). λK femtoscopy in pb-pb collisions at $\sqrt{s_{\mathrm{NN}}}$ = 2.76 tev.

Alme (2010). The ALICE TPC, a large 3-dimensional tracking device with fast readout for ultra-high multiplicity events.

Arash, F., Moravcsik, M. J., & Goldstein, G. R. (1985). Dynamics-independent null experiment for testing time-reversal invariance. *Phys. Rev. Lett.*, 54, 2649–2652.

Aubert, B. et al. (2006). Measurement of the spin of the Ω^- hyperon. *Phys. Rev. Lett.*, 97, 112001.

Barlow, R. (2002). Systematic errors: Facts and fictions. In *Conference on Advanced Statistical Techniques in Particle Physics* (pp. 134–144).

Barnes, V. E. et al. (1964). Observation of a hyperon with strangeness minus three. *Phys. Rev. Lett.*, 12, 204–206.

Belikov, Y., Safarík, K., & Batyunya, B. (1997). *Kalman Filtering Application for Track Recognition and Reconstruction in ALICE Tracking System*. Technical Report ALICE-INT-1997-24. CERN-ALICE-INT-1997-24, CERN, Geneva.

Berger, C. et al. (1979). Jet analysis of the $\Upsilon(9.46)$ decay into charged hadrons. *Physics Letters B*, 82(3), 449 – 455.

Bethe, H. & Ashkin, J. (1953). *Experimental Nuclear Physics*.

Bhasin, A. et al. (2010). Minimum bias trigger for pp physics with ALICE. *Indian Journal of Physics*, 84, 1733–1738.

Blum, W., Riegler, W., & Rolandi, R. (2008). *Particle Detection with Drift Chambers, 2nd ed.*

Bolotov, V. et al. (2005). Study of $K^- \to \pi^0 e^- \nu_e \gamma$ decay with ISTRA+setup. *Technical Report INR-1150/2005*.

Botta, E. (2017). Particle identification performance at ALICE. In *5th Large Hadron Collider Physics Conference*.

Burkard, H. et al. (1985). Muon decay: measurement of the positron polarization and implications for the spectrum shape parameter eta, V-A and T invariance. *Phys.Lett.*

Burnstein, R. et al. (2005). Hypercp: A high-rate spectrometer for the study of charged hyperon and kaon decays. *Nuclear Instruments & Methods in Physics Research Section A-accelerators Spectrometers Detectors and Associated Equipment*, 541, 516–565.

Carnesecchi, F. (2019). Performance of the ALICE time-of-flight detector at the LHC. *Journal of Instrumentation*, 14(06), C06023–C06023.

Chan, A. et al. (1998). Measurement of the Properties of the $\bar{omega}^+$ and $omega^-$ hyperons. *Phys. Rev. D*, 58, 072002.

Chen, Y. et al. (2005). Measurement of the Alpha Asymmetry Parameter for the $\Omega^- \to \Lambda K^-$. *Phys. Rev. Lett.*

Conrad, J., Contreras, J., & Jorgensen, C. (2005). Minimum bias triggers in proton-proton collisions with VZERO and pixel detectors.

Contin, G. (2012). Performance of the present ALICE Inner Tracking System and studies for the upgrade. *Journal of Instrumentation*, 7(6).

Cowan, G. (1998). *Statistical Data Analysis*. Oxford science publications. Clarendon Press.

Crivellin, A. et al. (2018). Combined explanations of $(g-2)_{\mu,e}$ and implications for a large muon EDM. *Phys. Rev.*

Dainese, A. (2008). Physics program of the ALICE experiment at the LHC. *Italian Phys. Soc. Proc.*, 96, 253–261.

D'Ambrosio, G. & Isidori, G. (2006). Determination ofCPandCPTviolation parameters in the neutral kaon system using the bell-steinberger relation and data from the KLOE experiment. *Journal of High Energy Physics*, 2006(12), 011–011.

Dellacasa, G. et al. (1999). ALICE technical design report of the inner tracking system (ITS).

Dobrzynski, L., Xuong, N.-H., Montanet, L., Tomas, M., Duboc, J., & Donald, R. (1966). Test of cp and c invariances in pp annihilations at 1.2 gev/c involving strange particles. *Physics Letters*, 22(1), 105 – 108.

Fee, M. S. et al. (1993). Measurement of the positronium $1\,^3s_1$–$2\,^3s_1$ interval by continuous-wave two-photon excitation. *Phys. Rev. A*, 48, 192–219.

Furry, W. H. (1937). A symmetry theorem in the positron theory. *Phys. Rev.*, 51, 125–129.

Gao, Y.-Q., Lao, H.-L., & Liu, F.-H. (2018). Chemical potentials of light flavor quarks from yield ratios of negative to positive particles in Au+Au collisions at RHIC. *Adv. High Energy Phys.*, 2018, 6047960.

Garabatos, C. (2004). The ALICE TPC. *Nuclear Instruments and Methods in Physics Research, Section A: Accelerators, Spectrometers, Detectors and Associated Equipment*, 535(1-2), 197–200.

Garwin, R. L., Lederman, L. M., & Weinrich, M. (1957). Observations of the failure of conservation of parity and charge conjugation in meson decays: the magnetic moment of the free muon. *Phys. Rev.*, 105, 1415–1417.

Gell-Mann, M. (1961). The eighfold way: a theory of strong interaction symmetry.

Gell-Mann, M., Oakes, R. J., & Renner, B. (1968). Behavior of current divergences under $su_3 \times su_3$. *Phys. Rev.*, 175, 2195–2199.

Glashow, S. (1961). Partial Symmetries of Weak Interactions. *Nucl. Phys.*, 22, 579–588.

Gluckstern, R. (1963). Uncertainties in track momentum and direction, due to multiple scattering and measurement errors. *Nucl. Instrum. Meth.*, 24, 381–389.

Greenberg, O. W. (2002). Violation Implies Violation of Lorentz Invariance. *Physical Review Letters*, 89(23).

Hamieh, S., Redlich, K., & Tounsi, A. (2000). Canonical description of strangeness enhancement from p–a to pb–pb collisions. *Physics Letters B*, 486(1), 61 – 66.

Hasinoff, M. et al. (2006). A Test of Time Reversal Invariance in Stopped Kaon Decay $K^+ \to \pi^0 \mu^+ \nu_\mu$. *AIP Conference Proceedings*.

Hawking, S. W. (1976). Breakdown of predictability in gravitational collapse. *Phys. Rev. D*, 14, 2460–2473.

Higgs, P. W. (1964). Broken symmetries and the masses of gauge bosons. *Phys. Rev. Lett.*, 13, 508–509.

Hori, M. (2018). Single-photon laser spectroscopy of cold antiprotonic helium. *Hyperfine Interactions*, 239, 1–8.

Khriplovich, I. & Lamoreaux, S. (1997). *CP Violation Without Strangeness*.

Kostelecky, V. A. (1998). Theory and tests of CPT and Lorentz violation. (November), 1–12.

Kraus, I. (2009). Alice pp physics programme.

Kuijer, P. (2003). The alice experiment at the CERN LHC. *Nuclear Physics B - Proceedings Supplements*, 117(SUPPL. 1), 62–64.

Lehnert, R. (2016). CPT Symmetry and Its Violation. *Symmetry*, 8(11), 114.

Lippmann, C. (2012). Performance of the ALICE Time Projection Chamber. In *Physics Procedia*.

Lippmann, C. (2014). Upgrade of the ALICE Time Projection Chamber.

Lu, L. et al. (2005). Observation of parity violation in the $\Omega^- \to \Lambda k^-$ decay. *Physics Letters B*, 617(1), 11 – 17.

Lu, L. et al. (2006). Measurement of the Asymmetry in the Decay $\overline{\Omega}^+ \to \overline{\Lambda} K^+ \to \bar{p}\pi^+ K^+$. *Phys. Rev. Lett.*

Lueders, G. (1954). On the Equivalence of Invariance under Time Reversal and under Particle-Antiparticle Conjugation for Relativistic Field Theories. *Matematisk-Fysiske Meddelelser Kongelige Danske Videnskabernes Selskab*, 28(5), 1–17.

Lueders, G. & Zumino, B. (1957). Some consequences of TCP-Invariance. 47, 385–386.

Massimo, A. (2007). *Technical Design Report*, volume 11.

Mills, A. P. & Berko, S. (1967). Search for *c* nonconservation in electron-positron annihilation. *Phys. Rev. Lett.*, 18, 420–425.

Monteno, M. (2005). Particle multiplicity in proton–proton collisions with ALICE. *Journal of Physics: Conference Series*, 5, 209–218.

Ne'eman, Y. (1961). Derivation of strong interactions from a gauge invariance. *Nuclear Physics*, 26(2), 222 – 229.

Pais, A. (1959). Notes on antibaryon interactions. *Phys. Rev. Lett.*, 3, 242–244.

Pais, A. & Jost, R. (1952). Selection rules imposed by charge conjugation and charge symmetry. *Phys. Rev.*, 87, 871–875.

Report, P. P. (2005). *Physics Performance Report Volume II Part 2*, volume II.

Salam, A. & Ward, J. (1964). Electromagnetic and weak interactions. *Physics Letters*, 13(2), 168 – 171.

Sirunyan, A. M. et al. (2020). Strange hadron production in pp and pPb collisions at $\sqrt{s_{NN}} = 5.02$ tev. *Phys. Rev. C*, 101, 064906.

Sozzi, M. S. (2018). *Discrete Symmetries and CP Violation*.

Tanabashi, M. et al. (2018). Particle Data Group. *Phys. Rev. D 98*.

Vasileiou, M. (2020). Strangeness production with ALICE at the LHC. *Physica Scripta*, 95(6), 064007.

White, C. (2001). Rare hyperon and kaon decays from HyperCP. *Int. J. Mod. Phys. A*, 16S1B, 687–689.

Wigner, E. P. (1959). *Group theory and its application to the quantum mechanics of atomic spectra*. Pure Appl. Phys. New York, NY: Academic Press. Trans. from the German.

Wu, C. S. et al. (1957). Experimental test of parity conservation in beta decay. *Phys. Rev.*, 105, 1413–1415.

Zweig, G. (1964). *An SU_3 model for strong interaction symmetry and its breaking; Version 1*. Technical Report CERN-TH-401, CERN, Geneva.

Acknowledgments

I WISH TO EXPRESS my deepest gratitude to my supervisor, Dr. Kai Schweda, for allowing me to take part in this highly interesting project. During the conduction of this work there were a lot of difficulties and burdens. Your endless support, encouragement, advice and patience enabled the successful completion of this thesis. I learned from you not to give up and continue to pursue goals independent on the circumstances.

I would like to thank Dr. Alexander Schmah for deepening my understanding of C++ and improvement of the analysis related codes and scripts. Without your help this work would not be possible.

Moreover, many thanks go to Prof. Dr. David Dobrigkeit Chinellato and Dr. Antonin Maire. Your precious discussions on V0 and cascade reconstruction with ALICE showed me how broad and deeply non-trivial the area of light flavour physics actually is.

I want to kindly thank Dr. Marten Ole Schmidt for helping me out with AliPhysics/AliRoot software and GitHub.

Erklärung

Hiermit versichere ich, dass ich die vorliegende Arbeit selbstständig verfasst und keine anderen als die angegebenen Quellen und Hilfsmittel benutzt habe, dass alle Stellen der Arbeit, die wörtlich oder sinngemäß aus anderen Quellen übernommen wurden, als solche kenntlich gemacht und dass die Arbeit in gleicher oder ähnlicher Form noch keiner Prüfungsbehörde vorgelegt wurde.

Heidelberg, den October 14, 2020 .....